HELIUM BURNING OF ^{22}NE: TARGETS, DETECTORS, AND INITIAL MEASUREMENTS

Sean Hunt

A dissertation submitted to the faculty of the University of North Carolina at Chapel Hill in partial fulfillment of the requirements for the degree of Doctor of Philosophy in the Department of Physics and Astronomy.

Chapel Hill
2019

Approved by:

Christian Iliadis

Art Champagne

Tom Clegg

Richard Longland

Fabian Heitsch

ABSTRACT

SEAN HUNT: Helium Burning of ^{22}Ne: Targets, Detectors, and Initial Measurements.
(Under the direction of Christian Iliadis)

The goal of the work in this dissertation is to advance the understanding of nuclear astrophysics by remeasuring a reaction vital to the stellar synthesis of heavy elements. The ^{22}Ne(α,γ)^{26}Mg and ^{22}Ne(α,n)^{25}Mg reactions are of great importance to the s-process which takes place in asymptotic giant branch and massive stars, and produces half of all elements heavier than iron. The low energy resonances in these reactions have the greatest impact on the s-process, but have poorly understood resonance strengths.

The α-particle beam necessary to measure the ^{22}Ne(α,n)^{25}Mg and ^{22}Ne(α,γ)^{26}Mg reactions are very damaging to solid targets. In this study, three types of targets made of glass, sintered metal, and evaporated metal were designed and fabricated. All three targets are capable of withstanding the effects of α-particle bombardment.

Previous measurements of the ^{22}Ne(α,n)^{25}Mg reaction saw significant contamination from the ^{13}C(α,n)^{16}O reaction. A significant effort was made in this dissertation to develop new capture-gated detector technologies to differentiate between low energy neutrons of interest and high energy contaminant neutrons. Structures in the signal pulses were identified, correcting a misunderstanding in the literature, and never-before-made measurements of detector resolution and efficiency were performed.

Finally, a measurement of the resonance strength of the 828 keV resonance in the ^{22}Ne(α,γ)^{26}Mg reaction was made using one of the new target designs. This measurement represents the first of this reaction using a coincidence detector system, the first time this reaction has been measured using a fraction fitting analysis technique, and the first time a nuclear reaction has been measured using blister-resistant solid targets. The value of the resonance strength for the 828 keV resonance determined in this work is 0.047(12) meV.

TABLE OF CONTENTS

LIST OF TABLES

LIST OF FIGURES

LIST OF ABBREVIATIONS

AFM	Atomic Force Microscopy
AGB	Asymptotic Giant Branch
BCI	Beam Current Integrated
BR	Branching Ratio
ECR	Electron Cyclotron Resonance
FF	Fraction Fitter
FWHM	Full Width at Half Maximum
HB	Horizontal Branch
HPGe	High-Purity Germanium
HR	Hertzsprung-Russell
LENA	Laboratory for Experimental Nuclear Astrophysics
$M_{\odot}$	Solar Mass
MCMC	Markov Chain Monte Carlo
MS	Main Sequence
PSD	Pulse Shape Discrimination
RGB	Red Giant Branch
TP − AGB	Thermally-Pulsing Asymptotic Giant Branch
TUNL	Triangle Universities Nuclear Laboratory

Chapter 1

Introduction

1.1 Astrophysical Motivation

Stellar nucleosynthesis is responsible for the production of most elements heavier than helium and virtually all elements heavier than beryllium. Iron, nickel and lower mass elements are produced in energy favorable reactions (i.e. reactions where the resultant nuclei have less rest mass than the reacting nuclei), whereas elements heavier than iron and nickel are produced in energy unfavorable reactions (i.e. reactions where the resultant nuclei have more rest mass than the reacting nuclei). Figure 1.1 illustrates this effect with a graph of the binding energy per nucleon versus atomic mass. It can be seen from this chart that energy must be released while fusing elements with a lower mass than iron, and energy is required to fuse elements heavier than iron.

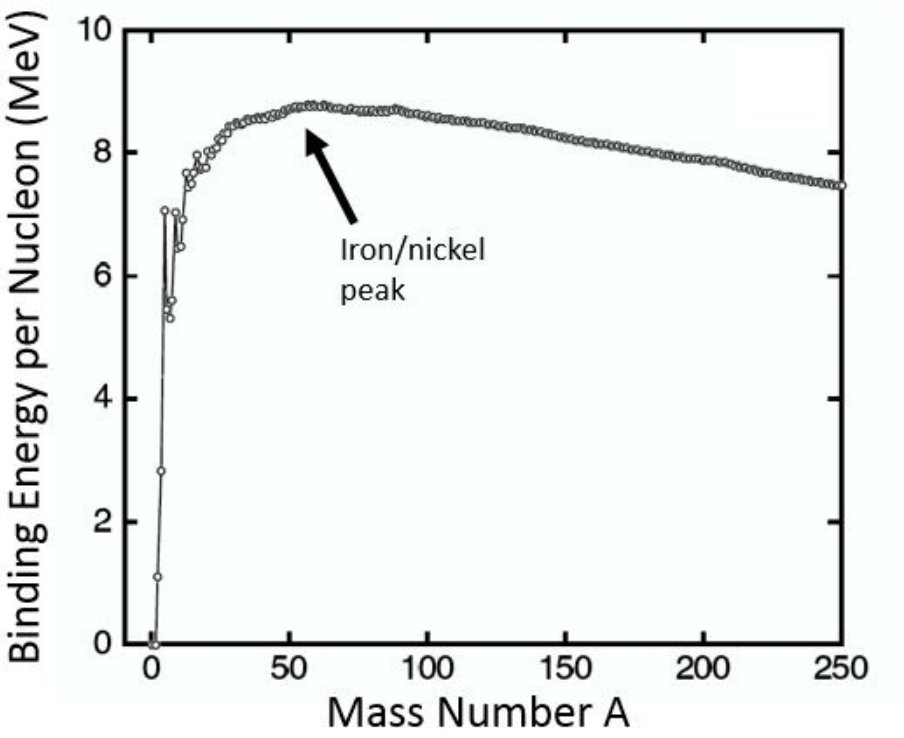

Figure 1.1: Binding energy per nucleon versus atomic mass. There is an increase in binding energy (and therefore an increase in energy released during fusion) for elements leading up to the iron/nickel peak, followed be decreasing binding energy per nucleon at higher atomic mass numbers. Figure is adapted from [Iliadis, 2015]. Data are taken from [Audi et al., 2003].

It has been known since 1957 [Burbidge et al., 1957] that stellar fusion of the elements heavier than iron primarily occurs through neutron capture. Significant neutron capture requires sufficiently high free neutron densities, which only occurs at the highest stellar temperatures. There are two astrophysical processes capable of producing these neutron density conditions: The r-process, or rapid neutron capture process, which occurs during the core-collapse of supernovae or merger of neutron stars, and the s-process, or slow neutron capture process, which occurs during the late burning stages of asymptotic giant branch stars (AGB) and in massive ($M > 10M_{\odot}$) stars. Figure 1.1a shows the elemental abundances of the solar system, and identifies the stellar processes primarily responsible for the production of those elements. Figure 1.1b shows the heavy elements produced

by the s-process and r-process, and illustrates the comparable quantities of elemental production each process is responsible for. The s-process is the focus of this study.

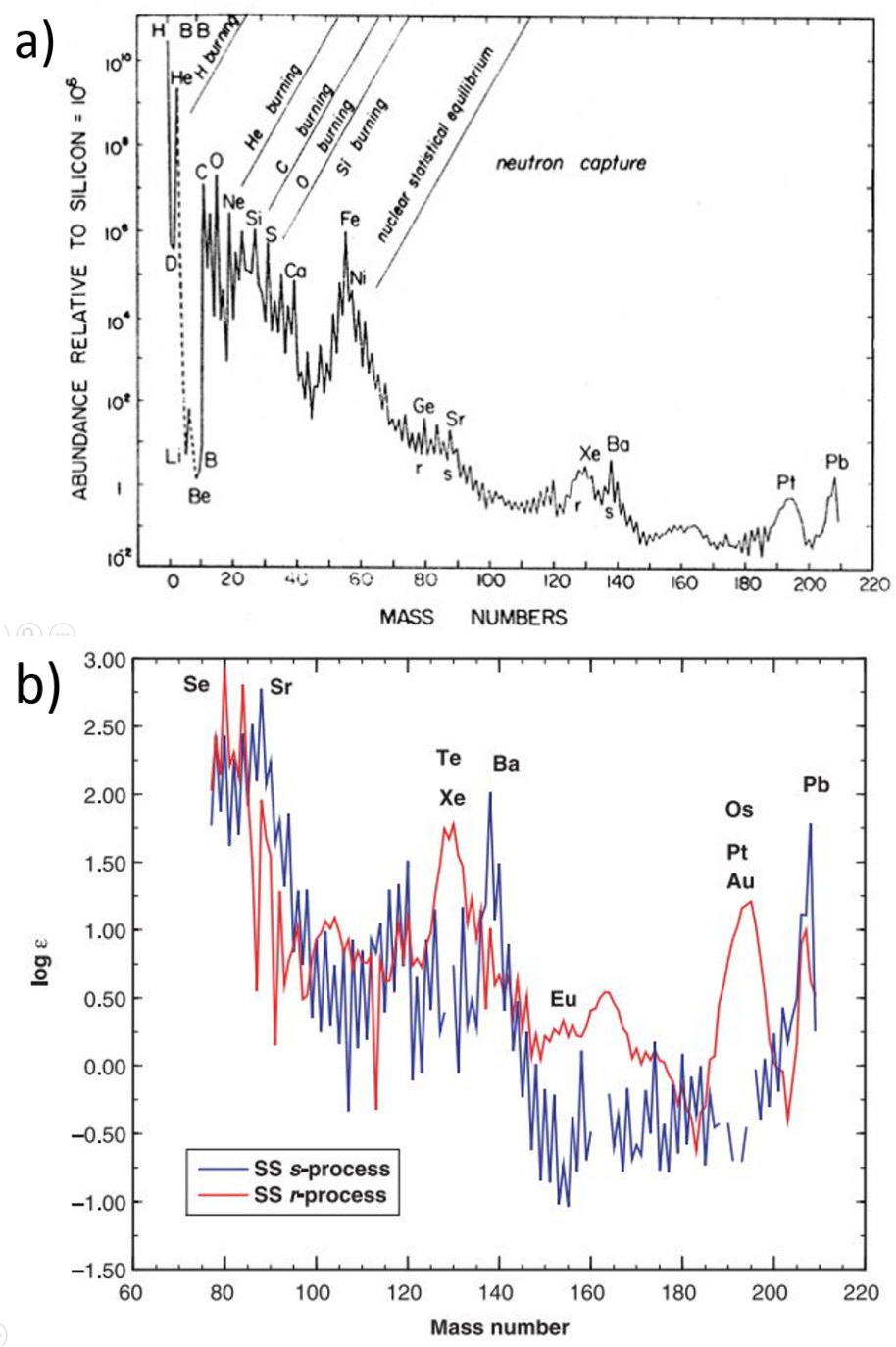

Figure 1.2: (a) Solar system elemental abundances. Values are relative to silicon which is arbitrarily normalized to 10^6. Diagonal lines indicate the processes responsible for the production of elements within an elemental mass region. Figure is taken from [Cameron, 1982]. (b) A comparison of heavy solar system (SS) elemental abundances normalized to silicon 10^6 (given as log ϵ). Nuclei formed from the r-process are given in red, and nuclear from the s-process are given in blue. Figure is taken from [Sneden and Cowan, 2003].

1.2 The s-Process

The s-process is a neutron induced nucleosynthesis process that takes place at moderately low (compared to the r-process) neutron density and moderately high temperature conditions in stars. The phenomenological picture of the s-process was first developed by the seminal papers [Burbidge et al., 1957, Cameron, 1957]. Additional details were discovered in the following decades in a number of influential papers [Clayton and Rassbach, 1967, Clayton and Ward, 1974, Clayton et al., 1961, Seeger et al., 1965].

In low neutron density environments, the time scale for neutron capture is typically slower than the β-decay time scale for elements near the β-decay stable isobars in the chart of isotopes. In these environments, stable isotopes capture neutrons over long periods of time, and eventually decay to form new elements. This process is in contrast to the r-process, wherein neutrons are captured faster than the average β-decay time, resulting in a number of neutron-rich elements far from the β-decay stable isobars rapidly beta decaying to stability (for more information on the r-process, see [Burbidge et al., 1957, Seeger et al., 1965, Thielemann et al., 2011]). Figure 1.3 illustrate the paths that the s- and r-processes take through the chart of isotopes to develop the heavier stable nuclei. It should be noted that there is an additional minor contribution to the nucleosynthesis of the heavy elements known as the p-process which involves proton capture and photofission that is not shown in the figure (for more information on the p-process, see [Arnould and Goriely, 2003, Burbidge et al., 1957, Cameron, 1957, Rayet et al., 1995]).

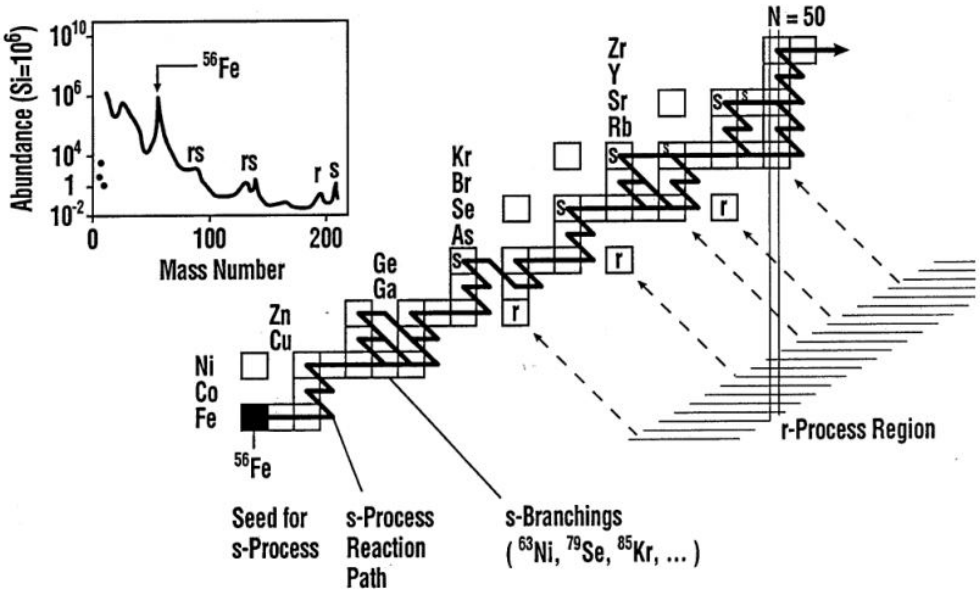

Figure 1.3: Illustration of the neutron-capture processes responsible for synthesis of the heavy elements. The s- and r-reaction paths are shown, though the p-process reaction paths are not. Image taken from [Käppeler et al., 2011].

There are two distinct components of the s-process that occur in different stellar environments. The *weak* s-process, and the *main* s-process.

1.2.1 The Weak s-Process in High Mass Stars

The weak s-process occurs in massive ($M > 8M_{\odot}$) stars [Arnett and Thielemann, 1985], such as the historically important star Betelgeuse (Shown in Fig. 1.4), and is responsible for the majority of the production of the s-process isotopes within the atomic mass range of $70 < \mathrm{A} < 90$ [Kappeler et al., 1989, Raiteri et al., 1991] (though [Travaglio et al., 2004] has shown that there must be an additional process responsible for some fraction of the $70 < \mathrm{A} < 90$ nuclei). A massive star burns through its hydrogen core in a matter of millions of years, and once the star begins to burn helium in the core, the temperature is hot enough to fuse ^{14}N (usually remnants from previous deceased stars) into ^{22}Ne through the following sequence of α captures and $\beta+$ decays:

$$^{14}\mathrm{N}(\alpha,\gamma)^{18}\mathrm{F}(e^{+},\nu)^{18}\mathrm{O}(\alpha,\gamma)^{22}\mathrm{Ne} \tag{1.1}$$

Toward the end of helium core burning, temperatures rise above 2.5×10^{8}K, which is high enough for ^{22}Ne to undergo ^{22}Ne(α,n)^{25}Mg burning, producing neutrons that fuel the weak s-process [Couch et al., 1974, Lamb et al., 1977, Peters, 1968, Prantzos et al., 1990, Raiteri et al., 1991]. Some ^{22}Ne survives the helium burning in the core, and when the massive star forms a carbon burning shell, the ^{22}Ne reacts with α particles produced by the ^{12}C(^{12}C, α)^{20}Ne reaction to reactivate the ^{22}Ne(α,n)^{25}Mg reaction and continue s-process nucleosynthesis [Arnett and Truran, 1969, Prantzos et al., 1990]. Carbon core burning does not contribute significantly to the s-process, primarily because material processed during carbon core burning rarely escapes the death of the star.

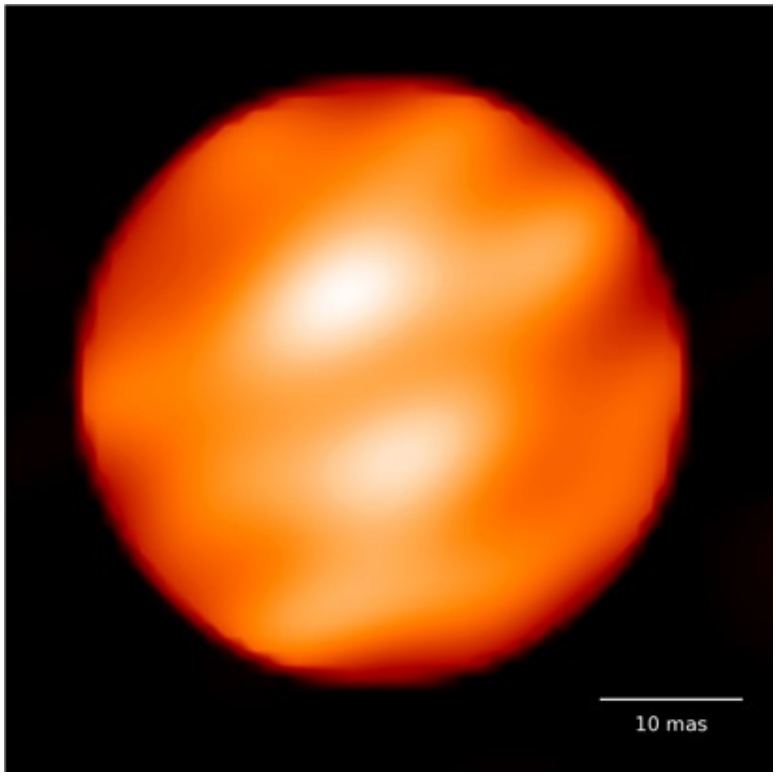

Figure 1.4: Betelgeuse is a massive star, estimated as much as 30 times more massive than our sun, residing ≈ 640 light years away [Harper et al., 2008]. Betelgeuse was the first star other than our sun to be directly imaged [Buscher et al., 1990]. The s-process is currently synthesizing heavy elements in the core of Betelgeuse. Image taken from [Haubois et al., 2009].

1.3 The Main s-Process in AGB Stars

The main s-process occurs in main sequence asymptotic giant branch (AGB) stars [Seeger et al., 1965] with a mass of $0.6M_{\odot} < M < 8M_{\odot}$, such as the historically important star Mira (shown in Fig. 1.5), and is responsible for the majority of the production of the s-process isotopes with atomic mass range of A > 90. The main s-process is more complicated than the weak s-process, and requires an understanding of late stage stars to fully describe it.

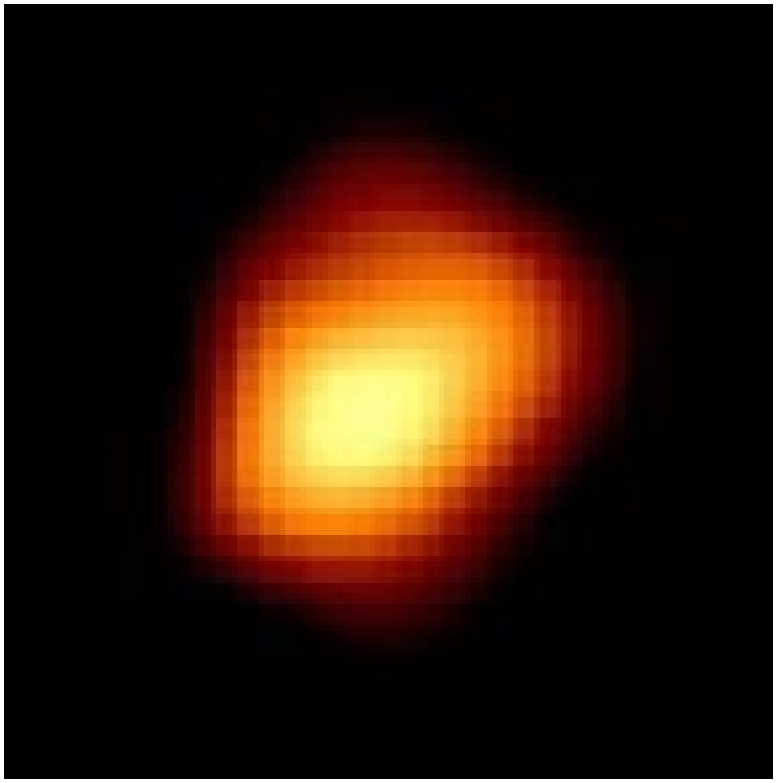

Figure 1.5: Mira (also known as Omicron Ceti) is a binary star system, consisting of Mira A, a thermally pulsing asymptotic giant branch star with a mass of $\approx 1.17 M_{\odot}$ [Wyatt and Cahn, 1983], and Mira B, a smaller low-mass white dwarf [Sokoloski and Bildsten, 2010]. The system resides $\approx$ 300 light years from the sun, and Mira A was the first non-supernova variable brightness star discovered [Hoffleit, 1997]. It is also currently synthesizing heavy elements through the main s-process. Image taken from [Karovska et al., 1997].

The name "asymptotic giant branch" is derived from the location of a star in a color-magnitude diagram known as a Hertzsprung-Russell (HR) diagram. An HR diagram is made by plotting the measured luminosity of a star against its surface temperature. Figure 1.6 is an example HR diagram for the stars in the globular cluster M15. For the first stage of a star's life, it exists in the main sequence (MS) portion of the HR diagram. During this stage, hydrogen is fused into helium in the core of the star through a series of reactions that eventually produce:

$$4\mathrm{H} \rightarrow^{4} \mathrm{He} + 2e^{+} + 2\nu + 26.7\mathrm{MeV} \tag{1.2}$$

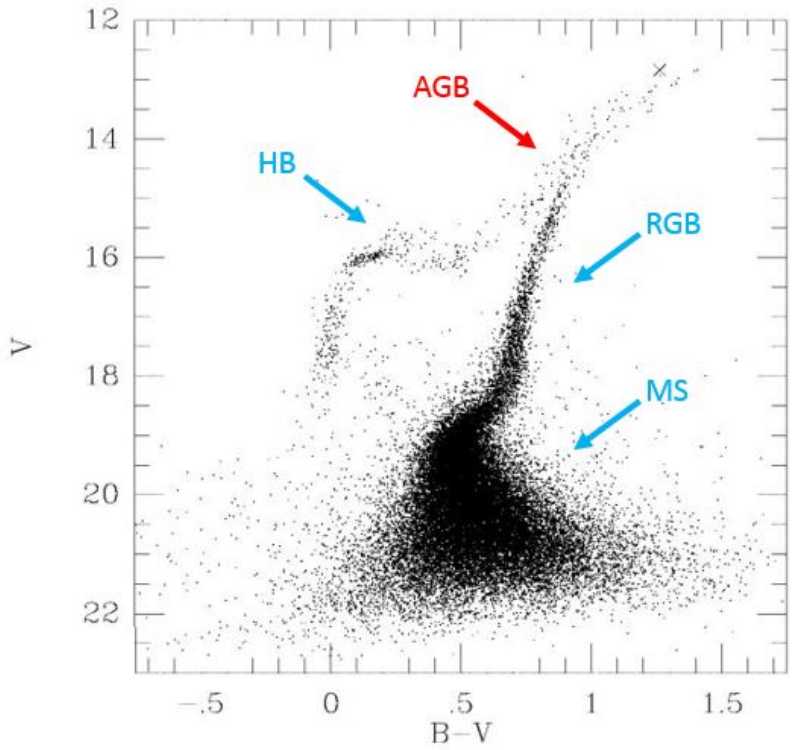

Figure 1.6: Color-magnitude diagram of stars in the globular cluster M15. The photometry was taken using the WFPC2 camera on the Hubble Space Telescope [van der Marel et al., 2002]. The x-axis is a B-V color index, and the y-axis is the absolute magnitude. The asymptotic giant branch (AGB) is labeled in red, and the horizontal branch (HB), red giant branch (RGB), and main sequence (MS) are labeled in blue.

Stars with a mass of $0.6M_{\odot} < M < 8M_{\odot}$ will remain on the main sequence for hundreds of millions or billions of years. Eventually, the star will exhaust the hydrogen in its core, and will undergo envelope expansion, core contraction, and ascension into the red giant branch (RGB) section of the HR diagram. At this point, the core of the star is burning helium through the reaction:

$$^{4}\text{He} + ^{4}\text{He} \rightarrow ^{8}\text{Be} - 91.8\,\text{keV} \tag{1.3}$$

Beryllium-8 is very unstable, and has a half life of only $\approx 6.5 \times 10^{-17}$s [Lin et al., 1974]. As the helium core contracts, the temperature rises to around 3×10^{8}K, at which point ^{8}Be is produced at a faster rate than it decays. At this time, fusion into the stable isotope ^{12}C

occurs through the reaction:

$$^{8}\text{Be} +^{4} \text{He} \rightarrow^{12} \text{C} + 7.4\,\text{MeV} \tag{1.4}$$

While the core is fusing helium, a hydrogen shell outside the core continues to burn. Eventually, the core of the star exhausts its supply of helium, and consists primarily of carbon and oxygen. During this phase, known as the early asymptotic giant branch phase (E-AGB), the star derives its energy from helium fusion in a shell surrounding the core. As the helium shell is exhausted, the star enters the thermally pulsing asymptotic giant branch phase (TP-AGB), and primarily burns hydrogen in a thin shell surrounding the nearly exhausted helium shell.

After burning for between 10^4 and 10^5 years, enough helium is created in the hydrogen burning shell to reignite the helium burning shell underneath in an explosive process known as a *helium shell flash*. These flashes dredge up material from the core of the star into the helium burning layer. For more detail on the helium flashes, see [Busso et al., 1999, Herwig, 2004, Iben Jr and Renzini, 1983, Sneden et al., 2008, Straniero et al., 2006]. In between thermal pulses, the s-process can synthesis heavy elements in a region of the star known as a "carbon pocket" using the following reaction as a neutron source:

$$^{13}\text{C} +^{4} \text{He} \rightarrow n +^{16} \text{O} + 2.215\,\text{MeV} \tag{1.5}$$

However, during the thermal pulses, ^{22}Ne in the core, either present from an earlier population star or synthesized from ^{14}N as described in Section 1.2.1, is dredged up into the helium burning shell. During these thermal pulses, neutrons for the s-process are provided by the reaction:

$$^{22}\text{Ne} +^{4} \text{He} \rightarrow n +^{25} \text{Mg} - 0.48\text{MeV} \tag{1.6}$$

For stars with a mass $M > 4M_{\odot}$, temperatures are expected to be high enough that

^{22}Ne(α,n)^{25}Mg is the primary source of neutrons for the main s-process. Figure 1.7, taken from [Reifarth et al., 2014], illustrates a thermal pulse within an AGB star.

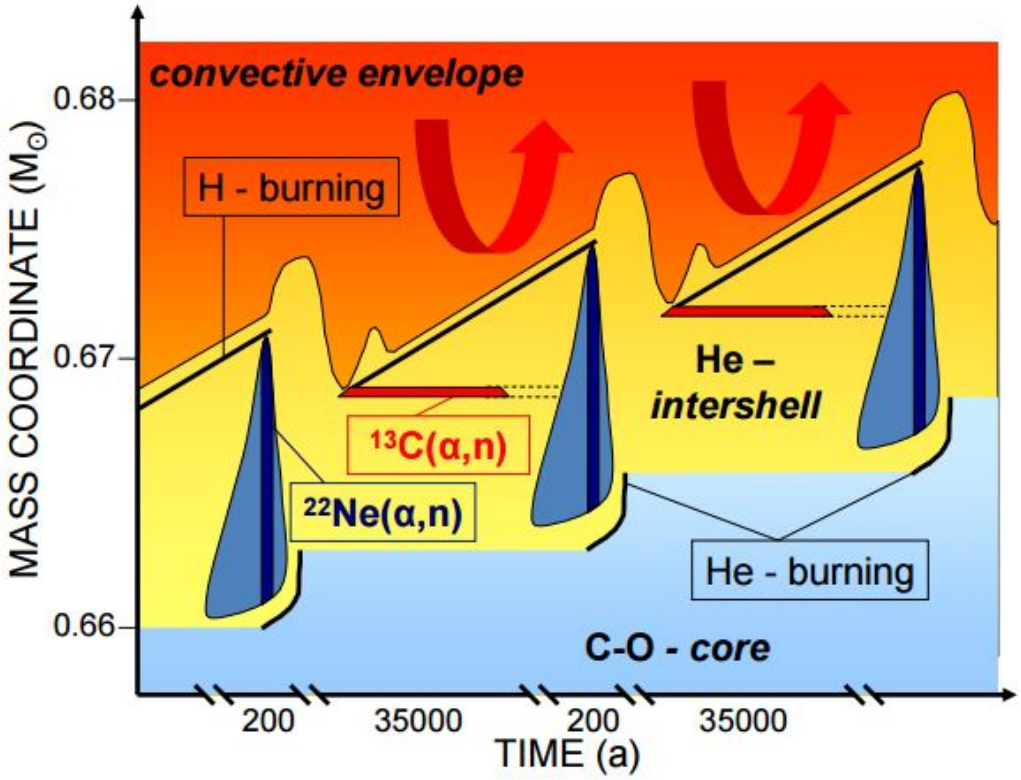

Figure 1.7: An example AGB star undergoing thermal pulse. The y-axis is a relative mass coordinate spanning the thickness of the helium burning shell, and the x-axis is time given in annus (years). Thermal pulses are associated with a disruption of the H burning layer, expansion of the C-O core, and heavy element synthesis using the ^{22}Ne(α,n)^{25}Mg reaction as a neutron source. Figure taken from [Reifarth et al., 2014].

1.4 The Importance of ^{22}Ne(α,n)^{25}Mg

The ^{22}Ne(α,n)^{25}Mg reaction is the primary neutron source the s-process in massive ($M > 8M_\odot$) stars, the dominant neutron source for the s-process in large ($M > 4M_\odot$) TP-AGB stars, and an additional neutron source for smaller ($M < 4M_\odot$) TP-AGB stars. The ^{22}Ne(α,γ)^{26}Mg reaction is equally important, as it competes with the ^{22}Ne(α,n)^{25}Mg reaction for available α particles. Both of these reactions are poorly measured, and have

a significant effect on our understanding of heavy element nucleosynthesis. [Longland et al., 2012] compiled and analyzed current data for the ^{22}Ne(α,n)^{25}Mg, and the competing ^{22}Ne(α,γ)^{26}Mg reactions, and showed that the uncertainties in the measurements have a significant effect on the abundance of elements up to mass number 100.

The importance of these two reactions extends beyond the understanding of the origin of the heavy elements. The ^{22}Ne(α,n)^{25}Mg reaction could also explain unusual elemental enhancements in metal-poor AGB stars, such as rubidium [García-Hernández et al., 2006, 2009, Karakas et al., 2012, Lugaro and van Raai, 2007, Pignatari et al., 2005], and affects elemental abundances frequently used to date galactic nucleosynthesis [Browne and Berman, 1981, Cowan et al., 1991, Hainebach and Schramm, 1976, Woosley and Fowler, 1979]. Additionally the ^{22}Ne(α,n)^{25}Mg and ^{22}Ne(α,γ)^{26}Mg reactions have a significant effect on the expected abundances of ^{24}Mg, ^{25}Mg, and ^{26}Mg. This is important because magnesium ratios can be precisely measured in presolar dust grains, and magnesium is one of the few elements that can have isotopic ratios derived from stellar spectra (such as ^{26}Mg/^{24}Mg and ^{25}Mg/^{24}Mg) [Yong et al., 2003a,b]. Using estimated reaction rate uncertainties for ^{22}Ne(α,n)^{25}Mg and ^{22}Ne(α,γ)^{26}Mg, [Karakas et al., 2006] showed that relative abundances of ^{25}Mg and ^{26}Mg predicted by stellar models can vary by up to 60%, impacting the magnesium ratio measurements in presolar grains.

Supernovae are also affected by the ^{22}Ne+α rates. Massive stars produce the iron isotope ^{60}Fe during the convective carbon-shell burning stage through the s-process [Chieffi and Limongi, 2002, Pignatari et al., 2010]. During type II supernova, ^{60}Fe and ^{26}Al are ejected, and are both γ-ray emitting radionuclides. The abundance ratio of these two isotopes provides stellar models a very sensitive constraint [Woosley and Heger, 2007]. It has also been shown that in type Ia supernovae, ^{22}Ne(α,n)^{25}Mg influences the electron mole fraction, affecting the nature of the explosion [Timmes et al., 2003]. Additionally, $\approx$ 1000 years prior to the explosion, neutrons produced by ^{22}Ne(α,n)^{25}Mg could affect the carbon abundance, which would alter the ^{56}Ni production, and therefore affect the peak

luminosity of the explosion [Piro and Bildsten, 2008].

1.5 This Study

The β-decay rates relevant to the s-process are well measured, but many of the neutron cross sections and reaction rates for neutron production are not well understood. The focus of this study is to improve the measurement of the ^{22}Ne(α,γ)^{26}Mg reaction, and develop technologies needed to improve the understanding of the ^{22}Ne(α,n)^{25}Mg reaction.

Chapter 2 discusses the nuclear physics behind reaction rates and nuclear capture. Chapter 3 details the accelerators used and the modifications needed to produce the α-particle beam used.

Chapter 4 details the design and fabrication of targets capable of withstanding the significant damage caused by α-particles. Three targets were designed, fabricated, and tested, and one was chosen for the ^{22}Ne(α,γ)^{26}Mg measurement. This represents the first successful design of a blister-resistant nuclear target, and a paper on the targets has been accepted for publication [Hunt et al., 2018].

Chapter 5 describes the detectors used in the measurement of the ^{22}Ne(α,γ)^{26}Mg reaction, and additional detectors that were characterized for the eventual measurement of the ^{22}Ne(α,n)^{25}Mg reaction. A significant effort was made in this dissertation to develop new capture-gated detector technologies to differentiate between low energy neutrons of interest and high energy contaminant neutrons. Additionally, never-before-made measurements of detector resolution and efficiency were performed. This work has been published in [Hunt et al., 2016].

Chapter 6 discusses the measurement of the 831 keV resonance in ^{22}Ne(α,γ)^{26}Mg reaction, and details the methods and values used in the calculations of the resonance strength. The results of Chapter 6 are currently being written to submit for publication. Chapter 7 provides a summary of the findings of this dissertation.

Chapter 2

Nuclear Reactions

The electromagnetic force is well understood, and the Coulomb interaction between charged particles is precisely known. The strong nuclear force however, is much more complex, and the reactions are much more difficult to predict. The calculations for nuclear interactions involving more than a few nucleons are computationally impractical, and useful information can only be obtained using experimentally measured approximations of the effective potentials. These approximations are customized to a specific energy of a specific reaction (with some exceptions). The next few sections outline some of the fundamentals of nuclear reactions, their measurements, and how these models apply to the ^{22}Ne(α,n)^{25}Mg and ^{22}Ne(α,γ)^{26}Mg reactions. It should be noted that many of the equations and information in this chapter are taken from [Iliadis, 2015] and references therein. Resonance energies discusses in this chapter are given in the center-of-mass frame, though in all other chapters the resonance energies will be given in the laboratory frame, unless stated otherwise.

2.1 Thermonuclear Reaction Rates

Thermonuclear reaction rates are a quantitative way of representing the probability of a nuclear reaction occurring within a stellar environment. The physical quantity known as the cross section, σ, is the probability that a particular nuclear interaction occurs between two nuclei (a target nucleous and incident nucleous), and is defined as:

$$\sigma \equiv \frac{N_r/t}{N_i/(tA) \times N_t} \tag{2.1}$$

where N_r/t is the number of interactions per unit time, $N_i/(tA)$ is the number of incident particles per unit area per unit time, and N_t is the number of target nucleous within the target area. The cross section has dimensions of area, and larger cross sections correspond to larger probabilities that the correlated reaction will occur. Cross section is usually expressed in barns, defined as:

$$1\ b \equiv 10^{-24}\ cm^2 \tag{2.2}$$

It is important to remember that in stellar environments, nuclei are not monoenergetic. The nuclei have a spread of energies that can usually be expressed using a Maxwell-Boltzmann distribution:

$$\phi(v) = 4\pi v^2\ (\frac{\mu}{2\pi kT})^{\frac{3}{2}} e^{\frac{-\mu v^2}{(2kT)}} \tag{2.3}$$

where v is velocity, T is stellar temperature, k is Boltzmann's constant, and μ is the reduced mass, given by:

$$\mu = \frac{M_i M_t}{M_i + M_t} \tag{2.4}$$

where M_i and M_t are the incident and target nuclei masses, respectively. The cross section and velocity distribution functions can be combined to form a reaction rate, defined as:

$$\langle \sigma v \rangle = \int_0^\infty \phi(v) v \sigma(v) dv \tag{2.5}$$

Nuclei in a stellar plasma are nonrelativistic and nondegenerate, excluding special cases (see, for example, [Wolf, 1965]). This allows the velocity to be replaced by the kinetic energy using the relationship:

$$v = \sqrt{\frac{2E}{\mu}} \tag{2.6}$$

It is possible to rewrite this equation substituting energy for velocity, which gives:

$$N_A\langle\sigma v\rangle = N_A\,(\frac{8}{\pi\mu})^{\frac{1}{2}}\frac{1}{(kT)^{\frac{3}{2}}}\int_0^\infty \sigma(E)Ee^{-\frac{E}{kT}}dE \tag{2.7}$$

where N_A is Avogadro's number. This equation is known as the reaction rate, and can be solved if the cross section ($\sigma(E)$) can be experimentally determined. This chapter will focus on capture of a particle by a nucleus, followed by emission of electromagnetic radiation in the form of a γ-ray, or emission of a neutron.

2.2 Resonant Contributions

Radiative-capture cross sections generally display two distinct characteristics at low energies: an overall energy dependence showing smooth, exponential increase with beam energy known as the non-resonant contribution, and sharp spikes superimposed over the smooth curve known as the resonant contribution, which is illustrated in Figure 2.1.

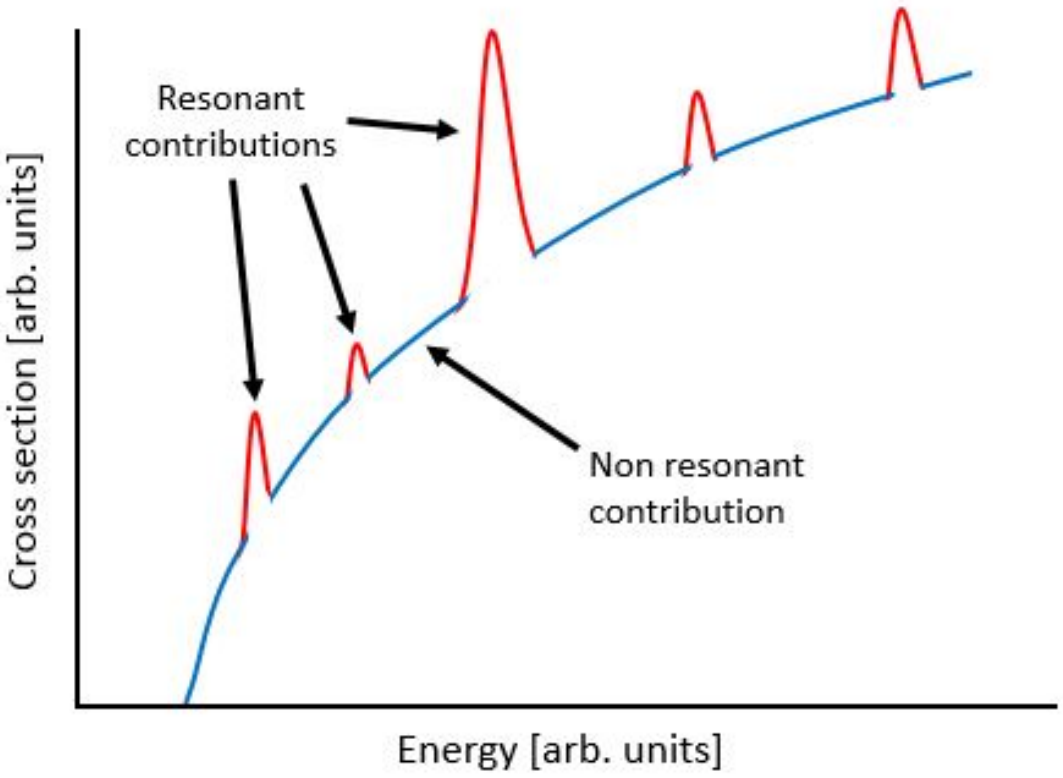

Figure 2.1: Illustration of resonant and non-resonant contributions to a cross section. Red peaks represent resonances, and the smooth blue line represents the non-resonant contributions.

Resonant captures, represented by the red peaks in Figure 2.1, do not vary smoothly, and have highly energy-dependent cross sections; the cross section of resonance dominated reactions can vary by orders of magnitudes over very narrow energy ranges. Resonances occur when the wavefunction of an incoming particle matches the internal wavefunction at the boundary where the Coulomb and strong forces are approximately equal in strength. Since the entrance channel energy is the combination of the Q-value for the reaction and the resonance energy, the equation describing the energy of the resulting state of the excited nuclei is:

$$E_x = Q + \frac{m_T}{m_T + m_\alpha} E_\alpha \frac{2}{1 + \sqrt{1 + 2E_\alpha m_T/(m_T + m_\alpha)^2 c^2}} \tag{2.8}$$

where E_x is the excitation energy, E_α is the bombarding particle energy, Q is the Q value for the reaction, and m_T and m_α are the masses of the target and bombarding particle, respectively.

2.2.1 Narrow Resonances

The total width of a resonance is defined as the sum of all the partial widths of allowed decays, and is usually expressed as:

$$\Gamma = \sum_i \Gamma_i \tag{2.9}$$

where Γ is the total width, and Γ_i are the partial widths of all decay channels (partial widths are a way to describe a probability, but in units of energy. See [Iliadis, 2015] for more information on partial widths). If a resonance is narrow enough (< 3 keV), the cross section can be represented by the Breit-Wigner equation:

$$\sigma_{BW}(E) = \frac{\lambda^2 \omega}{4\pi} \frac{\Gamma_{en}\Gamma_{ex}}{(E - E_R)^2 + (\Gamma/2)^2} \tag{2.10}$$

where Γ_{en} and Γ_{ex} are the partial widths for the entrance and exit channels respectively, λ is the de Broglie wavelength, defined as:

$$\lambda = \frac{2\pi\hbar}{\sqrt{2\mu E}} \tag{2.11}$$

and

$$\omega = \frac{(2J + 1)(1 + \delta_{01})}{(2J_i + 1)(2J_t + 1)} \tag{2.12}$$

where J is the spin of the resonance state, J_i is the spin of the incident particle, J_t

is the spin of the target, and δ_{01} is the Kronecker delta needed to create an extra factor of 2 for the case of identical target and projectile nuclei. For narrow resonances, the Maxwell-Boltzmann distribution can be assumed to be constant, allowing Equation 2.7 to be written as:

$$N_A\langle\sigma v\rangle = N_A\,(\frac{8}{\pi\mu})^{\frac{1}{2}}\frac{1}{(kT)^{\frac{3}{2}}}e^{-\frac{E}{kT}}\int_0^\infty E\,dE \tag{2.13}$$

Substituting the Breit-Wigner formula (Equation 2.10 into Equation 2.13, and assuming that the partial widths are constant, the reaction rate becomes:

$$N_A\langle\sigma v\rangle = N_A\,\frac{2\omega\sqrt{2\pi}\hbar^2\Gamma_{en}\Gamma_{ex}}{(\mu kT)^{\frac{3}{2}}\Gamma}\,e^{-\frac{E}{kT}}\int_0^\infty \frac{\Gamma/2}{(E_R-E)^2+\Gamma^2/4}dE \tag{2.14}$$

This is solvable, because:

$$\int_{-\infty}^{\infty}\frac{a}{(b-x)^2+a^2}dx = \pi \tag{2.15}$$

The narrow resonance reaction rate can now be written as:

$$N_A\langle\sigma v\rangle = N_A\,(\frac{\sqrt{2\pi}}{\mu kT})^{\frac{3}{2}}\hbar^2 e^{-E/kT}\omega\frac{\Gamma_{en}\Gamma_{ex}}{\Gamma} \tag{2.16}$$

It is often convenient to define the following relationship:

$$\omega\frac{\Gamma_{en}\Gamma_{ex}}{\Gamma} = \omega\gamma \tag{2.17}$$

where $\omega\gamma$ is the resonance strength.

The assumptions of an energy independent Maxwell-Boltzmann distribution and partial widths allowed the reaction rate for narrow resonances to be reduced to Equation 2.16. It can be seen from this formalism that an experimental measurement of the resonance strength is sufficient to obtain an accurate approximation of the reaction rate for a narrow-resonance-dominated stellar reaction, such as the ^{22}Ne(α,γ)^{26}Mg reaction.

2.2.2 Resonances in ^{22}Ne(α,n)^{25}Mg and ^{22}Ne(α,γ)^{26}Mg

Several direct measurements of the ^{22}Ne(α,n)^{25}Mg reaction have been performed since the early 1980s [Drotleff et al., 1993, Giesen et al., 1993, Harms et al., 1991, Jaeger et al., 2001, Wolke et al., 1989], and only a single direct measurement of the ^{22}Ne(α,γ)^{26}Mg reaction has been published [Wolke et al., 1989]. With the exception of [Giesen et al., 1993], all of these measurements were performed at Institut für Strahlenphysik in Stuttgart, Germany, using gas targets. Figure 2.2 shows the excitation function of the ^{22}Ne(α,n)^{25}Mg reaction measurement made by [Jaeger et al., 2001] on the left, and the measured cross section of the ^{22}Ne(α,γ)^{26}Mg reaction made by [Wolke et al., 1989] on right. It can be seen from the graphs that both reactions are dominated by narrow resonances.

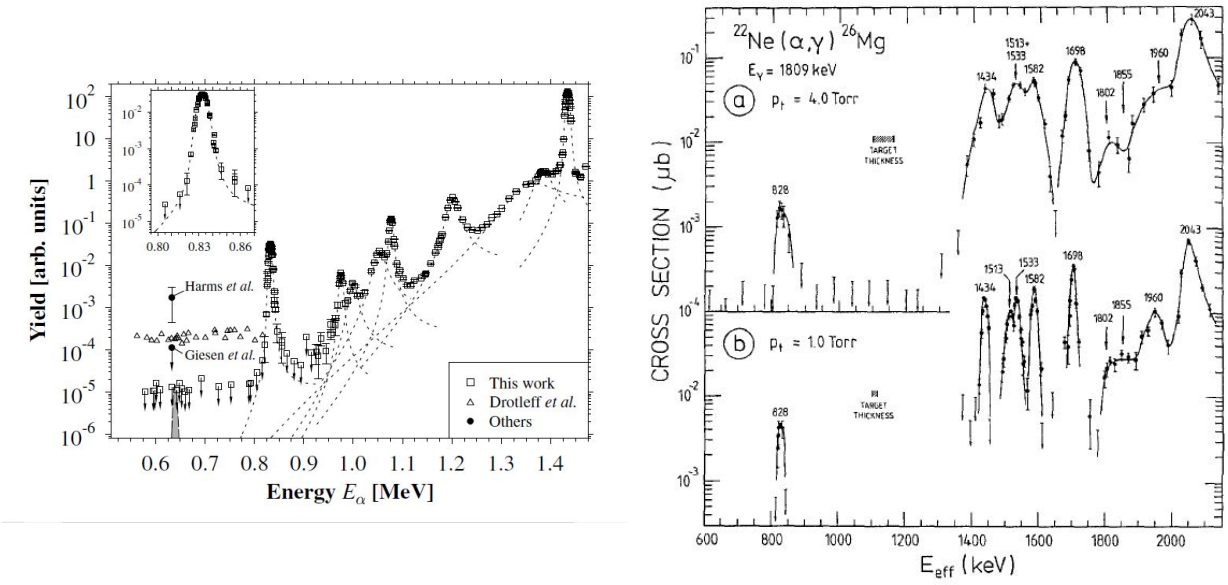

Figure 2.2: (Left) The excitation function for the ^{22}Ne(α,n)^{25}Mg reaction taken from [Jaeger et al., 2001]. This measurement was made with ^{3}He proportional counters, and an extended gas cell target. The additional image in the upper left is an enhanced view of the 831 keV resonance. (Right) The measured cross section of the ^{22}Ne(α,γ)^{26}Mg reaction by [Wolke et al., 1989]. This measurement was made by detecting the 1809 keV γ-ray emitted from the deexcitation of the first excited state of the resulting ^{26}Mg nucleus, and also used a gas cell target. The top graph of the ^{22}Ne(α,γ)^{26}Mg measurement represents a measurement with a 4.0 Torr target gas pressure, and the bottom graph represents a 1.0 Torr gas pressure. Both measurements were performed at the Institut für Strahlenphysik in Stuttgart, Germany.

Most of the s-process interactions utilizing the ^{22}Ne(α,n)^{25}Mg and ^{22}Ne(α,γ)^{26}Mg reactions takes place in stellar environments with a temperature of $\approx$ 300 MK (see Chapter 1 for more information on the s-process astrophysical sites). The center-of-mass energy region corresponding to this temperature amounts to $E_{cm} = 600 \pm 300$ keV. To determine the contribution individual resonances (and direct capture) have to the total reaction rates, a Monte Carlo method embedded in the code RATESMC was used to analyze resonant reaction contributions.

For every individual parameter contributing to a reaction rate (see Equation 2.16), there is an associated probability distribution representing the uncertainty of that parameter. For example, resonance strengths are represented with log-normal distributions, resonance energies are Gaussian, and upper limits on partial widths use Porter-Thomas distributions. For a given temperature, RATESMC randomly samples each parameter, and calculates the total reaction rate. This is repeated 10,000 times per temperature, resulting in a total recommended reaction rate based on the 0.50 quantile of the reaction rate distribution. For a more detailed explanation of this method, see [Iliadis et al., 2010, Longland et al., 2010b]

For the ^{22}Ne(α,n)^{25}Mg and ^{22}Ne(α,γ)^{26}Mg reactions, relevant parameters were taken from STARLIB [Sallaska et al., 2013] and used as input to RATESMC. Contribution plots were produced, indicating the importance of each resonance to the total reaction rate at a given temperature, shown in Figure 2.3. The y-axis represents the fractional contribution of each process or resonance to the total reaction rate (for example, at a temperature of 0.02 GK in ^{22}Ne(α,γ)^{26}Mg, the 76 keV resonance dominates the total reaction rate), and the thickness of each individual "band" represents the uncertainty in that fractional contribution. The dotted line encompasses all resonances and processes (including direct capture) that account for < 0.1 fraction of the reaction rate. All resonance energies shown are in the center-of-mass frame.

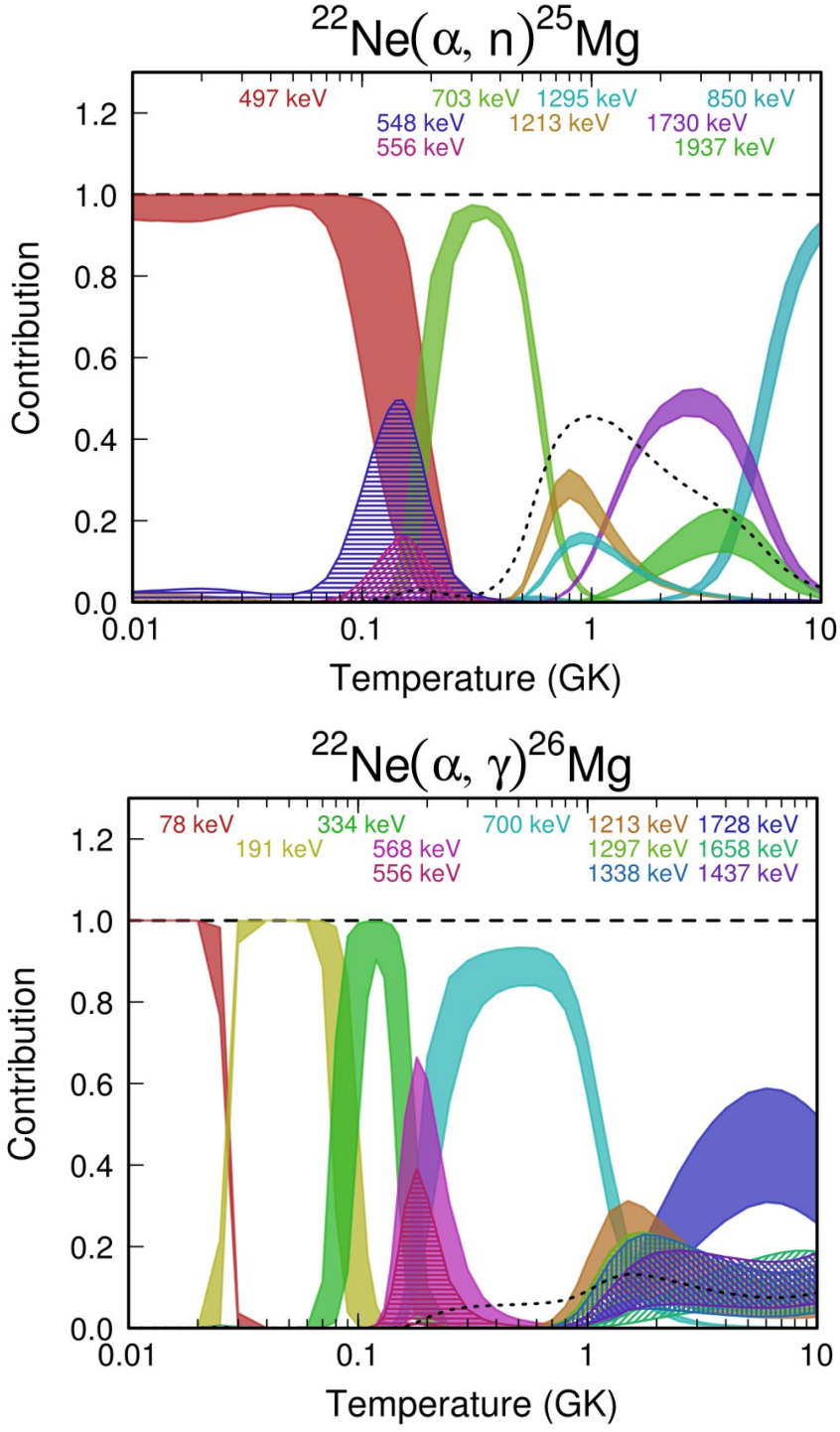

Figure 2.3: Resonance contribution plots for the ^{22}Ne(α,n)^{25}Mg reaction (top) and the ^{22}Ne(α,γ)^{26}Mg reaction (bottom) in the center-of-mass frame. The y-axis represent the fractional contribution to the total reaction rate for each individual process, the thickness of each resonance's "band" represent the uncertainty in that contribution, and the dotted line represents all contributions with < 0.1 fractional contribution. The 703 keV (831 keV lab frame) resonance dominates both reaction rates for the 300 MK temperature regime most important for the s-process.

At 300 MK, both reaction rates are dominated by the 831 keV (703 keV center-of-mass frame) resonance. This resonance has long been identified as one of the most important resonances to the s-process, and has been measured several times, with the measurement results summarized in Table 2.1. The table shows that the measured resonance strengths of the 831 keV resonance in ^{22}Ne(α,n)^{25}Mg disagree by a factor of up to 3 (and a detailed reading of the references listed reveals that the resonance strengths of the higher energy resonances disagree by up to a factor of 5), which is well outside the quoted uncertainties.

Reference	Resonance Energy (keV)	$\omega\gamma$ (eV)	Resonance Width Γ (keV)
[Harms et al., 1991]	830 ± 3	$(8.3 \pm 2.4) \times 10^{-5}$	≤ 3
[Giesen et al., 1993]	828	$(2.34 \pm 0.77) \times 10^{-4}$	...
[Drotleff et al., 1993]	831 ± 3	$(1.8 \pm 0.3) \times 10^{-4}$	≤ 3
[Jaeger et al., 2001]	832 ± 2	$(1.18 \pm 0.11) \times 10^{-4}$	0.25 ± 17

Table 2.1: Past measurements of the ^{22}Ne(α,n)^{25}Mg 831 keV resonance.

Sources of systematic error potentially responsible for the disagreement in measured resonance strength discussed in the literature include uncertain densities of the gas targets used, and neutron contamination from the ^{13}C(α,n)^{16} reaction. The only measurement made of low energy resonances in the ^{22}Ne(α,γ)^{26}Mg reaction (by [Wolke et al., 1989]) was not hindered by the neutron contamination, but still used the same gas cell target, which could have the same unknown systematic uncertainties. A large focus of this dissertation is the development and characterization of technologies and techniques to reduce or eliminate these systematic uncertainties.

It should be noted that an argument has been made that the 831 keV resonances in ^{22}Ne(α,n)^{25}Mg and ^{22}Ne(α,γ)^{26}Mg cannot both correspond to the same excited state in ^{26}Mg. This argument was put forward by [Koehler, 2002] who showed that the implied γ-ray partial width measured by [Wolke et al., 1989] ($\Gamma_\gamma = 76 \pm 56$eV) was far larger than the average γ-ray partial width in this range ($\Gamma_\gamma = 3$eV). However, [Longland et al., 2012] argues that the large uncertainty for the partial widths in [Wolke et al., 1989] makes it very possible that both resonances excite the same state. It should also be noted that the

high level density of ^{26}Mg around the excitation energy for this resonance adds significant ambiguity to the question of distinct resonances. The exact resonance energy of 831 keV resonance in ^{22}Ne(α,γ)^{26}Mg was not measured in this study, so it is assumed in this dissertation that the ^{22}Ne(α,γ)^{26}Mg resonance of interest is located at 831 keV, and not the 828 keV originally reported by [Wolke et al., 1989].

2.3 Non-Resonant Contributions

While the focus of this study was the measurement of the ^{22}Ne(α,γ)^{26}Mg resonance-dominated reaction, a detector was studied to aid in the eventual measurement of the ^{22}Ne(α,n)^{25}Mg reaction (see Chapter 5). This detector could differentiate between the low energy ($\approx$ 300 keV) neutrons from the reaction of interest and high energy ($\approx$ 3 MeV) neutrons from the primary contaminating reaction, ^{13}C(α,n)^{16}, which is a non-resonant reaction at these energies.

A non-resonant reaction, known as a direct capture reaction, occurs when a target nucleus captures an incident particle and emits a particle (such as a γ-ray), forming a bound state of a final nucleus in a single step. The interaction is actually between the incident particle and the electromagnetic field of the target nucleus, as depicted in Figure 2.4. The target nucleus can be approximated as an inert core, and the cross section for direct capture interactions vary smoothly with energy (because of the dependence on the electromagnetic interactions). Because of the simplicity of direct capture, the energy of the emitted γ-ray can be approximated by the equation:

$$E_\gamma = Q_{i\gamma} + E_i - E_x \tag{2.18}$$

where E_γ is the energy of a single direct capture primary, E_i is the center-of-mass energy of the incident nucleus, E_x is the bound state energy, and $Q_{i\gamma}$ is the separation energy of the target nucleus. For the full relativistic expression, see Equation C.14 in

[Iliadis, 2015].

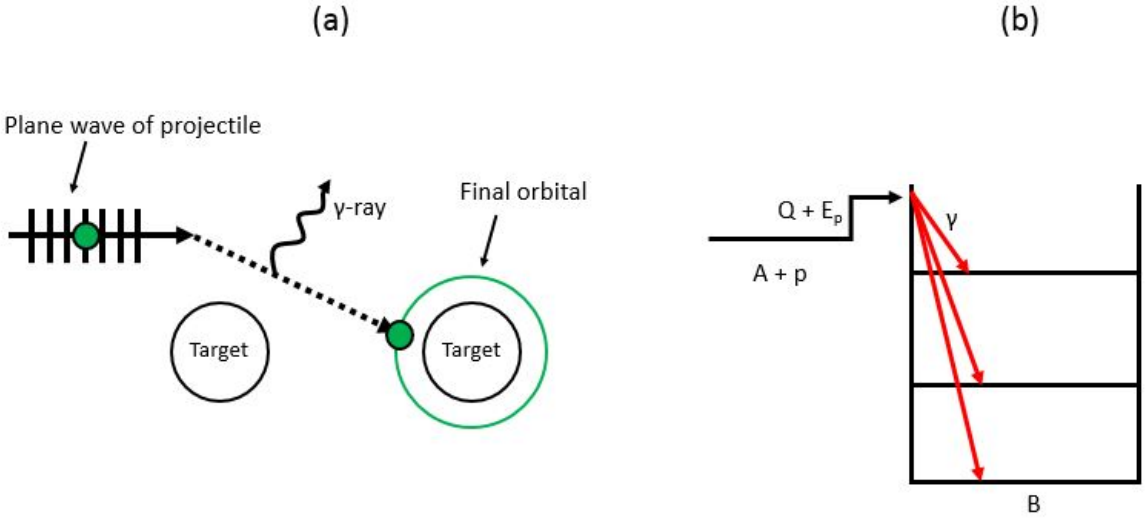

Figure 2.4: Illustration direct capture. a) A particle incident on a target nucleus interacts with the electromagnetic field and transitions directly into a bound state (figure adapted from [Rolfs and Rodney, 1988]). b) An energy level diagram of (a). A represents the initial target nucleus, p is an incident proton, E_p is the energy of the incident proton, and B is the final nucleus.

The ^{22}Ne + α reactions proceed through the compound nucleus ^{26}Mg, which has a relatively high energy of excitation ($Q_{\alpha\gamma}$ = 10614.74(4) keV [Wang et al., 2017]), and are dominated by resonant capture. Because of this, the direct capture contributions to the cross sections of the ^{22}Ne(α,n)^{25}Mg and ^{22}Ne(α,γ)^{26}Mg reactions are negligible at stellar temperatures (see [Longland et al., 2010b] for details).

The overview of non-resonant interactions has been intentionally kept brief for this dissertation, and is primarily mentioned to give a general understanding of the ^{13}C(α,n)^{16}, which is of importance to Chapters 4 and 5. For a more detailed explanation of non-resonant capture, see [Iliadis, 2015].

Chapter 3

Accelerators

Three accelerators were utilized in the present measurements. The measurements themselves were performed at the Laboratory for Experimental Nuclear Astrophysics (LENA) at the Triangle Universities Nuclear Laboratory (TUNL) in Durham, North Carolina (a schematic of LENA is shown in Figure 3.1 with all major beamline components and accelerators labeled). LENA is equipped with a JN Van de Graaff accelerator that was modified in the present work to produce α particles, and an Electron Cyclotron Resonance (ECR) source used to produce a number of the targets used in this study. An Eaton NV-3206 ion implanter located at the University of North Carolina at Chapel Hill was also used to produce a number of the targets used in this study.

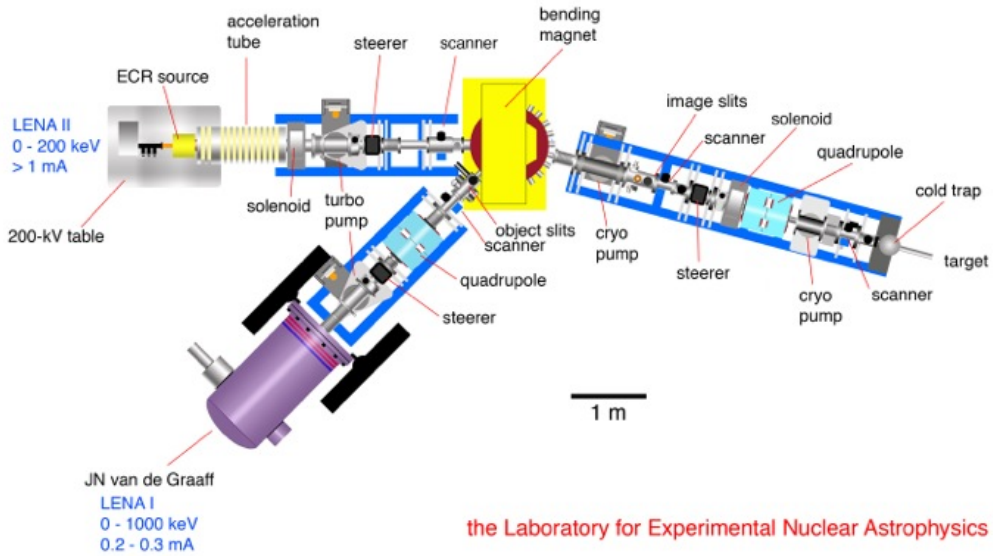

Figure 3.1: Schematic for the LENA experimental area. Major beamline components, steering elements, vacuum systems and target chamber components are clearly labeled.

3.1 JN Van de Graaff Accelerator

The JN Van de Graaff accelerator (hereafter referred to as the *JN*) is a High Voltage model JN-type accelerator at LENA that has been modified to accommodate a radio-frequency ion source and associated high-output beam. A plasma is formed by an RF oscillator capacitively coupled to a quartz ion plasma source bottle, and is intensified by an external magnetic field produced by permanent magnets. Gas is fed into the bottle via a controlled gas leak, and the RF electric field excites electrons, causing collisions between the electrons and neutral gas particles. Once the electrons acquire enough kinetic energy, these collisions ionize the gas, striking a plasma. The plasma is confined by the axial magnetic field, and can be positioned along the source bottle through adjustment of metal clips on the quartz bottle responsible for producing the RF electric field. The plasma is then extracted using a variable electric potential of 0-3 kV applied to a metal probe at the end of the ion source. During standard operation at the energies of interest to this study, the JN ion source is held under $\approx$ 170 psi of a nitrogen, carbon dioxide, and sulfur hexafluoride gas mixture to electrically insulate the terminal and acceleration column.

Once a sustain plasma is generated, the extraction and focusing component inject the charged particles into an acceleration column capable of accelerating voltages up to 1 MV. The charged particles are then focused and steered through a set of narrow slits before passing through the analyzing magnet. The magnet selects the energy of the beam via a feedback circuit that balances beam current on the horizontal slits at the exit of the magnet. A Terminal Potential Stabilizer (TPS) then adjusts the terminal voltage as necessary to guarantee the correct beam energy is obtained. Calibration of the analyzing magnet is achieved through several measurements of well-known resonance reactions, which are shown in Table 3.1. For a desired beam energy of E, the magnetic field of the analyzing magnet, B, is determined by:

$$B = \frac{k}{q}(2mc^2E + E^2)^{1/2} \tag{3.1}$$

where q and m are the charge and mass of the ions being accelerated, and k is the calibration constant [Rolfs and Rodney, 1988]. After passing through the analyzing magnet the beam encounters another set of magnetic steerers and quadrupole shaping magnets, followed by a rastering system that scans the beam across the target face in a grid pattern at a frequency of ≈ 2 Hz to guarantee uniform charged particle deposition on the target. The beam then passes through a scanner that allows for determination of the size and shape of the beam spot before finally reaching the target.

Reaction	Γ (eV)	E_r^{lab} (keV)
^{18}O(p,γ)^{19}F	150.82(9)	130(10)
^{26}Mg(p,γ)^{27}Al	292.06(9)	< 37
	338.4(1)	< 40
	453.8(1)	< 81
^{27}Al(p,γ)^{28}Si	202.8(9)	
	326.97(5)	< 38
	405.44(10)	< 42

Table 3.1: Tabulation of resonances used for the LENA analyzing magnet calibrations [Iliadis, 2007].

Targets were held at the end of the LENA beamline in a target chamber, illustrated in Figure 3.2. The charged particle beam first travels through a liquid nitrogen cooled copper shroud which reduces contaminant buildup on the target. The beam then travels through a 1.27 cm diameter collimator placed before the target to ensure that the beam spot does not extend beyond the implanted region of the target. A secondary electron suppression ring right before the target is biased to -300 V and prevents emission of secondary electrons from the target, improving the accuracy of the measurement of the integrated beam current. The vacuum in the target chamber is maintained at 5×10^{-7} Torr by a turbo pump and oil-less scroll pump.

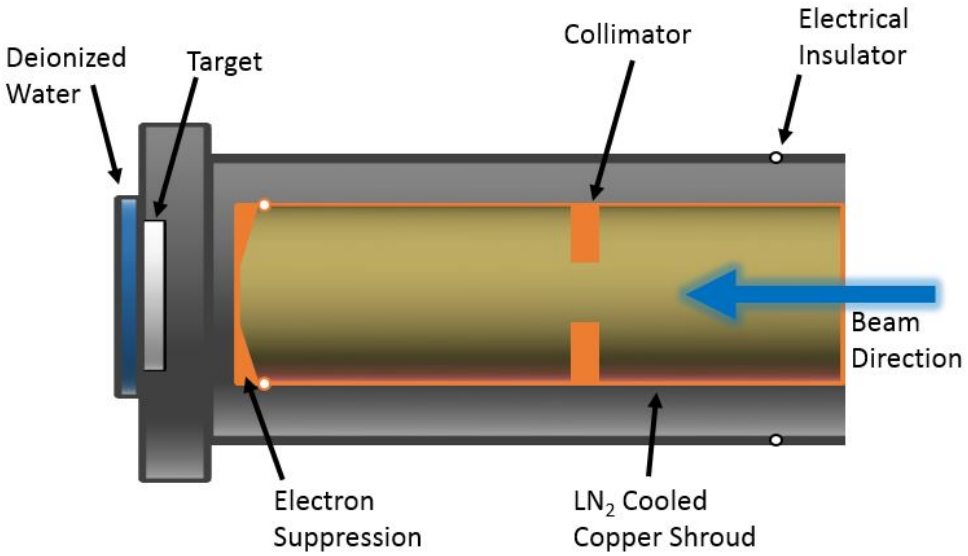

Figure 3.2: Schematic drawing of the LENA target chamber. The beam passes through a liquid nitrogen cooled copper shroud (to reduce buildup of contaminants on the target), a collimator, a secondary electron suppression ring (-300 V bias) and finally strikes the target in a water-cooled holder. The target holder is electrically isolated to allow the measurement of the accumulated charge of the incident charged particle beam.

3.1.1 JN Test Stand

The JN at LENA typically produces and accelerates protons, and modifications were needed for the ion source to produce the helium plasma needed to create the α particles necessary to measure the ^{22}Ne(α,γ)^{26}Mg reactions. The JN accelerator sees heavy use in LENA, so modifications needed to be thoroughly planned and tested to avoid unnecessary accelerator downtime. To accomplish this, the JN ion source was duplicated onto a test bench (hereafter referred to as the *test stand*) and modifications were tested before being replicated on the JN. Figure 3.3 shows the test stand used for these modifications. A hydrogen plasma was first created to serve as a benchmark for testing of the helium plasma, and a current of $\approx$ 0.5 mA was measured at the focus electrode. It was discovered that changing the hydrogen gas to helium, and altering the gas pressure and certain

RF tuning parameters was required to produce the maximum current from ionized helium at the focus electrode. This helium plasma had a current of ≈ 0.4 mA at the focus electrode.

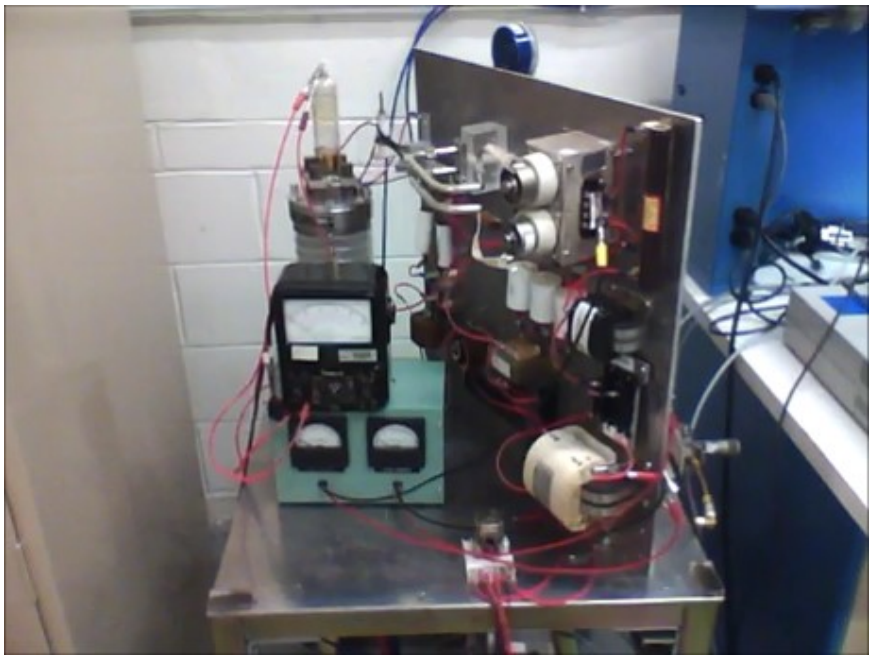

Figure 3.3: The duplicate JN ion source (test stand). The plasma bottle is mounted on a short acceleration column in the background, and the electronics responsible for producing and extracting the plasma are on a vertical aluminum sheet for easy access. Current and voltage monitors are in the foreground, and the hydrogen and helium gas sources are behind the vertical aluminum sheet.

3.1.2 JN Modifications

After identifying needed modifications on the test stand, The JN bell tank was depressurized and opened to allow the modifications to be made to the ion source. To test and modify the JN ion source, an ammeter was attached to the focus electrode, and the three electrodes after the focus electrode were held at the extraction potential. This forced plasma acceleration by the extraction electrode to deposit its charge on the focus electrode, allowing the beam current to be read by the ammeter. Table 3.2 provides typical operating parameters for maximum beam at the focus electrode.

Parameter	Hydrogen	Helium
Grid current	3 mA	3 mA
Plate current	350 mA	450 mA
Extraction voltage	1.7 kV	2.0 kV
Gas pressure	1.6 $\times 10^{-6}$ Torr	2.4 $\times 10^{-6}$ Torr
Twin-lead length	3 inch	3 inch
Current at focus electrode	0.3 mA	0.25 mA

Table 3.2: Typical tuning parameters for maximum beam current at the focus electrode. The JN was open and exposed to atmosphere for these tests, and specific values (such as gas pressure and extraction voltage) will be changed slightly when accelerating beam the to the target.

Because the JN had never produced α particles before, the accelerator needed additional calibration for precise beam energies. First, the calibration for protons was used and the mass of an α particle was substituted into Equation 3.1 in place of the proton mass. Because of the accuracy of measured atomic masses, this is thought to produce an accurate calibration.

To confirm this, a direct calibration using the 400 keV and 814 keV resonances in ^{7}Li(α,γ)^{11}B reaction [Green et al., 1962, Hardie et al., 1984] was performed. a ^{7}Li target was produced by evaporating thin layer of LiF on a tantalum backing. The resonances were measured using the bending magnet calibrations described above were used and the yields were determined from the primary γ-ray from the $R \rightarrow 4445$ keV transition in the 814 keV resonance, and the primary γ-ray from the $R \rightarrow 0$ keV transition in the 400 keV resonance. The front edges of the calibration are shown in Figure 3.4. It was confirmed that the beam was properly calibrated using the initial method, and no additional adjustments to the calibration were necessary. A value of 2 keV is used for the energy resolution of the JN, as that is the quoted energy resolution of the bending magnet.

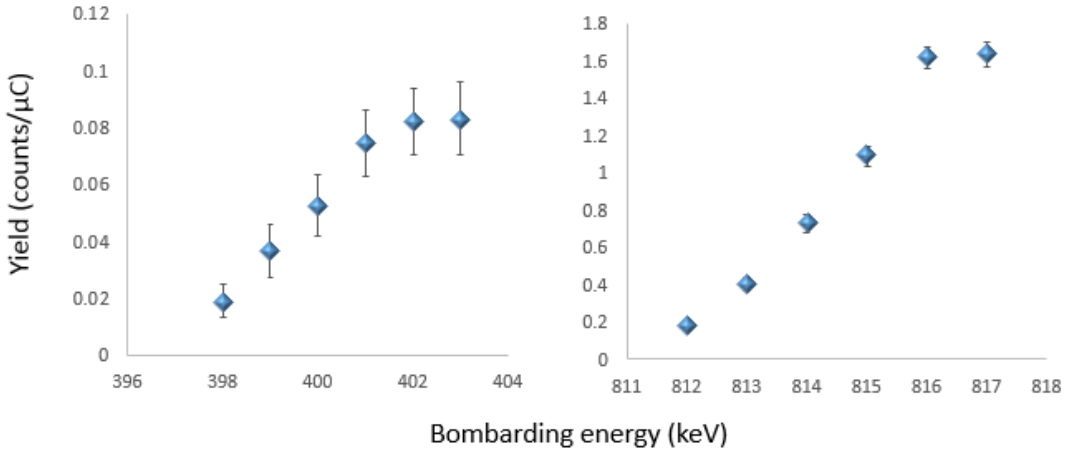

Figure 3.4: Yield curves of the 400 (left) and 814 (right) resonances in the ^{7}Li(α,γ)^{11}B reaction. The γ-rays observed were from the $R \rightarrow 4445$ keV transition in the 814 keV resonance, and the $R \rightarrow 0$ keV transition in the 400 keV resonance.

3.2 Eaton Ion Implanter

3.3 temp1

The tantalum and fused silica targets for this study were implanted (see Chapter 4 for details on tantalum targets, fused silica targets, and target implantation) with ^{22}Ne using an Eaton NV-3206 ion implanter with a modified end station at the University of North Carolina at Chapel Hill. Shown in Figure 3.5, the implanter is capable of producing ion beams using a variety of gas sources with an energy range of 20-200 keV. For these targets, neon ions were produced by using a low-pressure gas discharge within the Freeman ion source. The gas was ionized with electrons emitted by a tungsten filament, and the ionized gas was extracted with a 20 kV power supply. The ions were then passed through a 90 degree analyzing magnet, allowing the ^{22}Ne ions to be selected with a slit located at twice the radius from the end of the magnet (similar to the analyzing magnet used with the JN). The magnet was adjusted to select for $^{22}Ne^{+}$, which corresponded to a magnetic field of 0.503 T. The mass resolution of the analyzing magnet in the Eaton NV-3206 ion implanter is listed at 1% with a mass range of up to 125 amu. This guarantees that only

$^{22}Ne^{+}$ is accelerated through the magnet to the target backing.

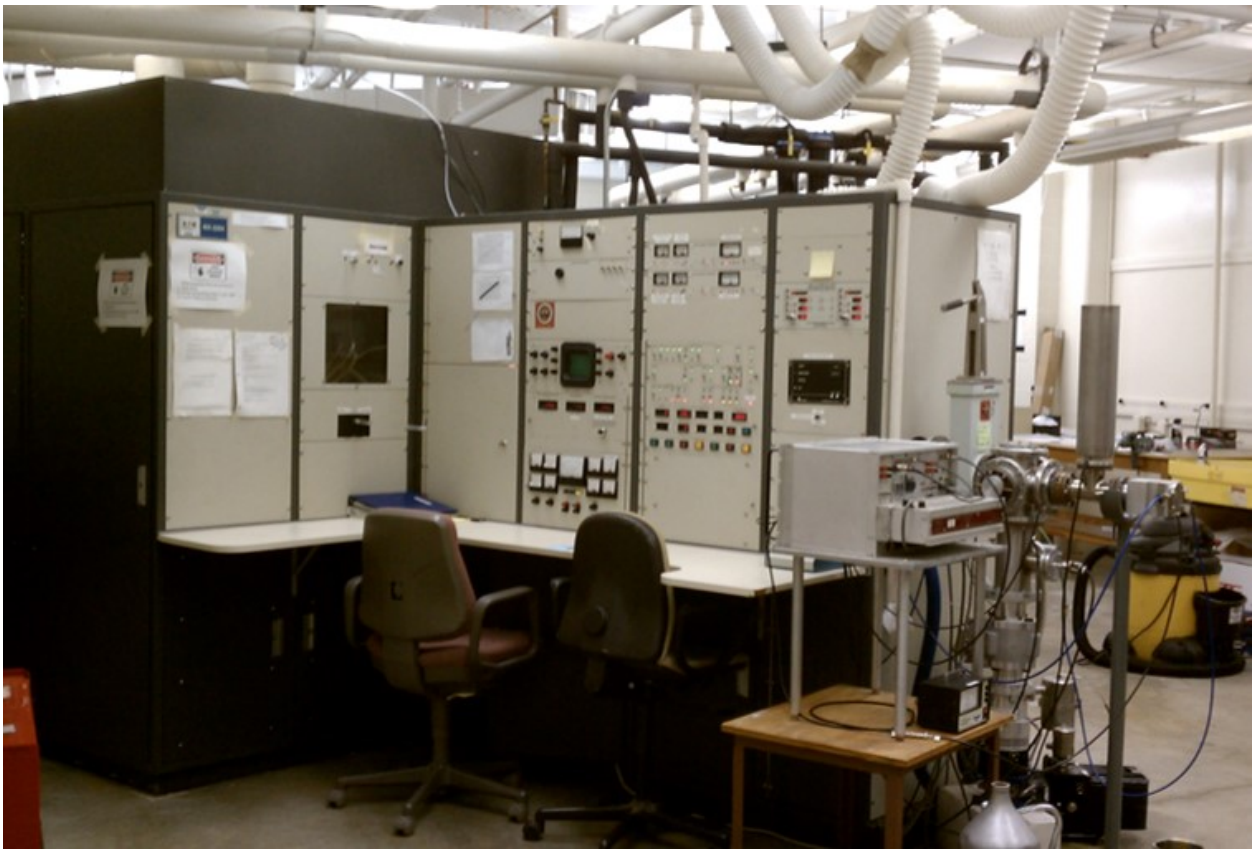

Figure 3.5: The Eaton NV-3206 ion implanter at UNC-CH. This accelerator was decommissioned in the summer of 2018.

Figure 3.6 shows the major components of the implanter. Ions are produced in the source using a resistively heated tungsten filament. These ions are mass separated in the analyzing magnet before being accelerated down the column. The ions pass through quadrupole shaping magnets and steering magnets which focus the beam and steer it to the target. A beam rastering system and beam collimator guarantee the beam is evenly spread across the target in a 2.54 cm diameter circle, and a liquid-nitrogen-cooled copper shroud prevents contaminants from plating onto the target surface. The target holder was water cooled to dissipate excess heat from the implantation and was electrically isolated to allow the incident $^{22}Ne^{+}$ dose to be measured. The geometry of the implanter target chamber was modeled after the chamber used in LENA and is held below 5×10^{-7} Torr

by a turbo vacuum pump. The Eaton ion implanter was capable of producing $\approx 200\mu$A of ^{20}Ne+ on the target, and $\approx 15\ \mu$A of ^{22}Ne+ on the target using natural neon gas in the plasma chamber.

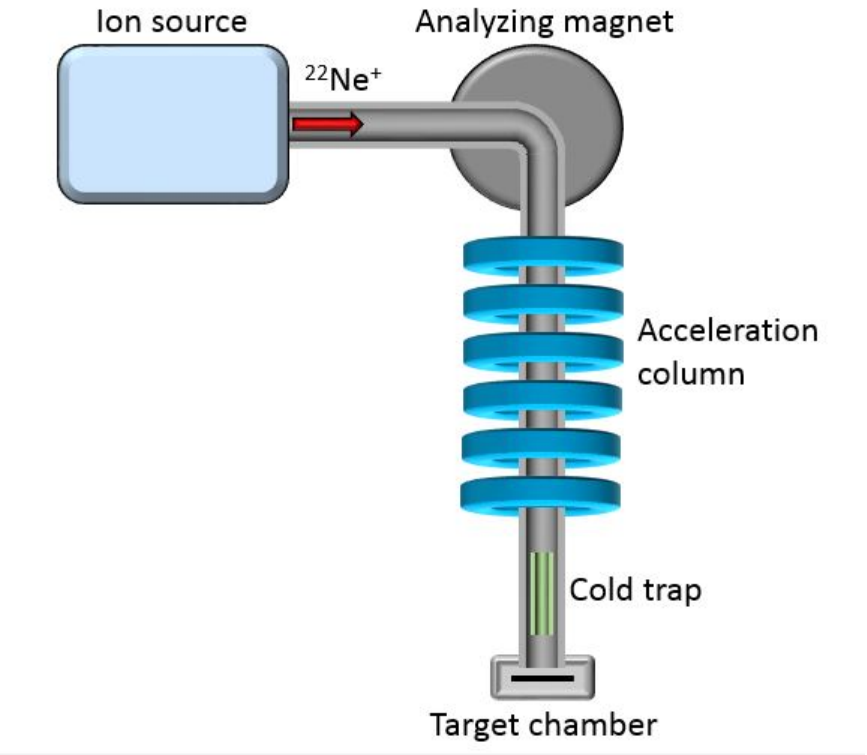

Figure 3.6: Schematic of the Eaton NV-3206 implanter at UNC-CH. $^{22}Ne^{+}$ ions are produced in the source, mass separated in the analyzing magnet, and accelerated through the column and cold trap before implanting into the target backing.

3.4 Electron Cyclotron Resonance (ECR) Source

A number of hardware problems with the Eaton ion implanter led to its decommission before all the targets needed for this study were implanted. To finish implantation, the Electron Cyclotron Resonance (ECR) source at LENA was modified to produce a $^{22}Ne^{+}$ beam. The ECR generates a plasma by injecting microwaves into a chamber at with a frequency corresponding to the electron cyclotron resonance frequency (as defined by a uniform magnetic field within the plasma chamber). If alternating electric field of the

microwaves is synchronous with the cyclic period of the free electrons, a resonance is obtained, greatly increasing the kinetic energy of the free electrons. Collisions between the free electrons and gas particles within the chamber result in ionization of the gas and formation of a plasma.

The acceleration column (shown in Figure 3.7 for the ECR was specially designed to extract, focus, and accelerate very high current beams (> 10 mA of proton beam). Modifications to the gas injection system and microwave tuning parameters allowed the ionization of neon.

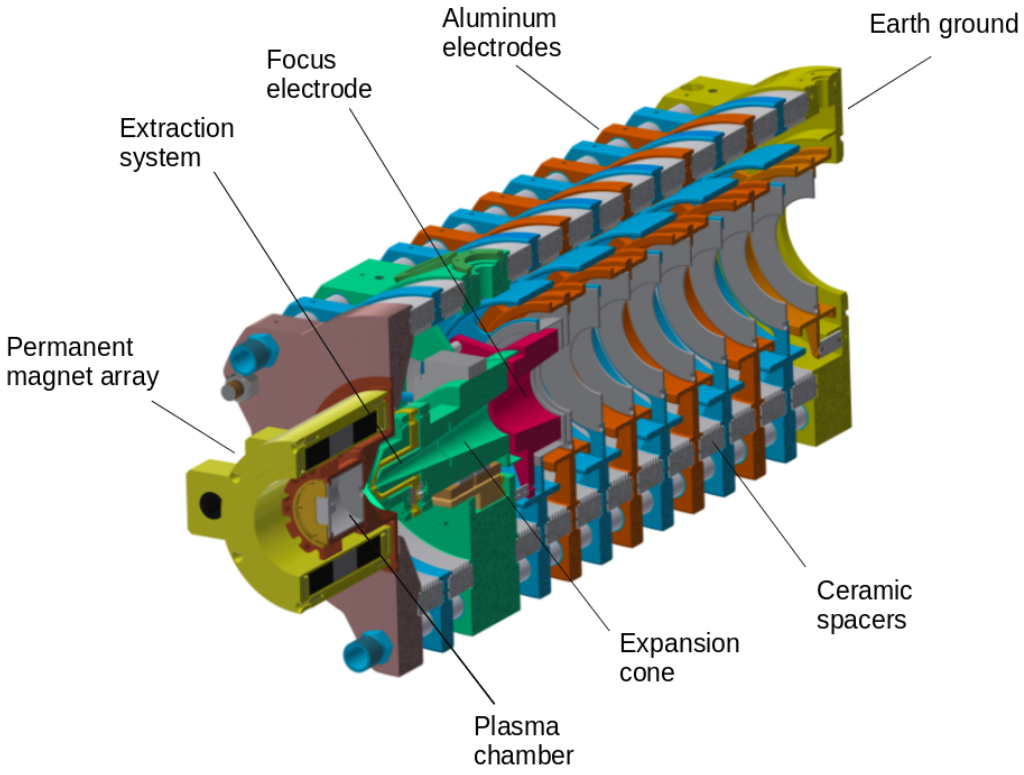

Figure 3.7: Cut-away view showing the ECR ion source and acceleration column with all major components labeled. Image taken from [Cooper et al., 2018].

A temporary implantation line was constructed on the spare 30° left port on the analyzing magnet, providing the ability to differentiate between isotopes of neon. The implantation line was equipped with electrostatic focusing, magnetic steering, and magnetic rastering elements to ensure the maximum uniform particle deposition on the target. A

target chamber similar to that shown in Figure 3.2 was installed on the end of the implantation line, and the pressure in the beamline was held below 3×10^{-7} Torr by a turbo vacuum pump. The modified ECR source and new implantation line provided $\approx$ 1mA of ^{20}Ne+ on the target, and $\approx$ 75 μA of ^{22}Ne+ on the target using natural neon gas in the plasma chamber. This accelerator was used to implant the sintered metal and porous evaporated metal targets designed and tested in this study (see Chapter 4 for details on these targets).

Chapter 4

Targets

Problems with previous measurements of the ^{22}Ne(α,n)^{25}Mg and ^{22}Ne(α,γ)^{26}Mg reactions were mentioned in Chapter 2, one of which was an issue of understanding the density of gas targets used. Instead of a gas target, implanted targets were chosen for this study primarily for their uniform thickness and stability under high intensity ion bombardment. The aim of this chapter is to summarize the target backing preparation, implantation, contaminant reduction techniques, and new target designs developed to prevent beam induced damage.

The targets used for preliminary testing in the ^{22}Ne(α,γ)^{26}Mg reaction measurement and contaminant studies were fabricated using tantalum target backings. The tantalum (99.95% metals basis purity, excluding niobium) was purchased in 0.5 mm thick, 20 cm $\times$ 20 cm sheets from Alfa Aesar. The sheets were cut at the UNC machine shop, producing 25 target backings per sheet. Each backing measured 38 mm $\times$ 38 mm with a 3 mm diameter hole cut in one corner (see Fig. 4.1).

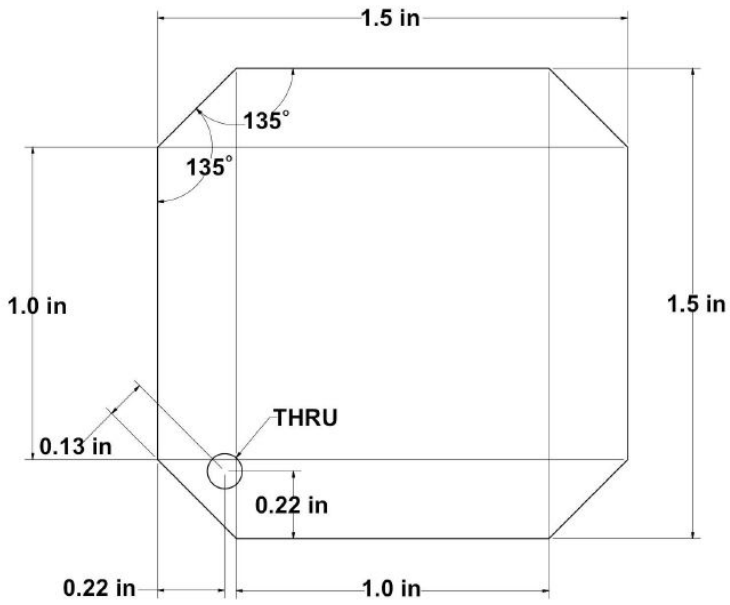

Figure 4.1: A schematic drawing of the target backings used for some of the of the experiments described in this dissertation.

4.1 Preparation of Target Backings

Metal target backings typically have impurities that can cause beam induced background under particle bombardment. To reduce the background from impurities, care was given to the handling, storage, and preparation of the target backings, ensuring cleanliness and reducing impurities. The target backings and implanted targets were stored in a polycarbonate vacuum box, shown in Fig. 4.2. The target box was constructed by the UNC machine shop. The vacuum was generated using an oil-free dry piston pump attached to one of the ports on the top of the box. This method of storage prevents dust buildup on the target face, and minimizes oxidization and gettering of the target face.

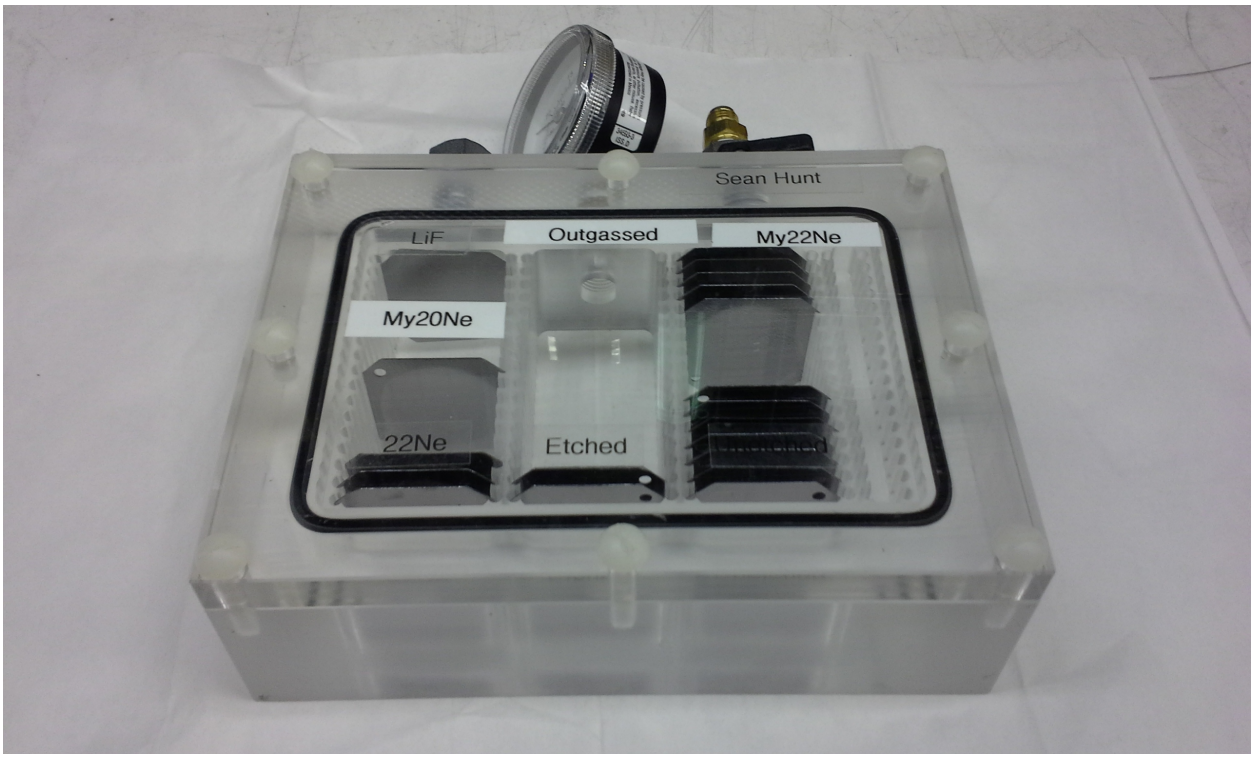

Figure 4.2: The polycarbonate target box used to store backings and implanted targets under vacuum.

4.1.1 Wet Etching

The first process in the preparation of tantalum target backings is known as wet etching. Wet etching removes oxide layers, machining oil, fingerprints, and any other surface contaminants acquired during production of the tantalum backing material through chemical dissolution in acid. The acid solution used consisted of five parts 95% sulfuric acid (H_2SO_4), two parts 70% nitric acid (HNO_3), and two parts 50% hydrofluoric acid (HF) mixed together in that order [Vermilyea, 1953]. The HF acid is highly corrosive, and reacts strongly with both glass and metal, so the mixture was contained within a teflon beaker, and handled under a fume hood with extensive personal protective equipment. A pair of Tefzel ethylene tetrafluoroethylene (ETFE) tongs with a small hook on the end were fastened to the punched hole in the corner of the backing, and the targets were dipped into the acid mixture, as illustrated in Figure 4.3. The reaction between the tantalum and

the acid mixture is highly exothermic, so the teflon beaker containing the acid was stored in an ice bath. Each target was submerged for a total of 60 seconds in 20 second intervals, allowing for the target to cool off in deionized water when not in the acid mixture. The etching process reduces the thickness of the backing from 0.5 mm to 0.35 ± 0.05 mm thick, removing surface impurities and machining blemishes. Each batch of acid was capable of etching three tantalum backings, after which the acid needs to be replaced. Finally, each etched backing was washed with 200 proof ethanol and left to dry.

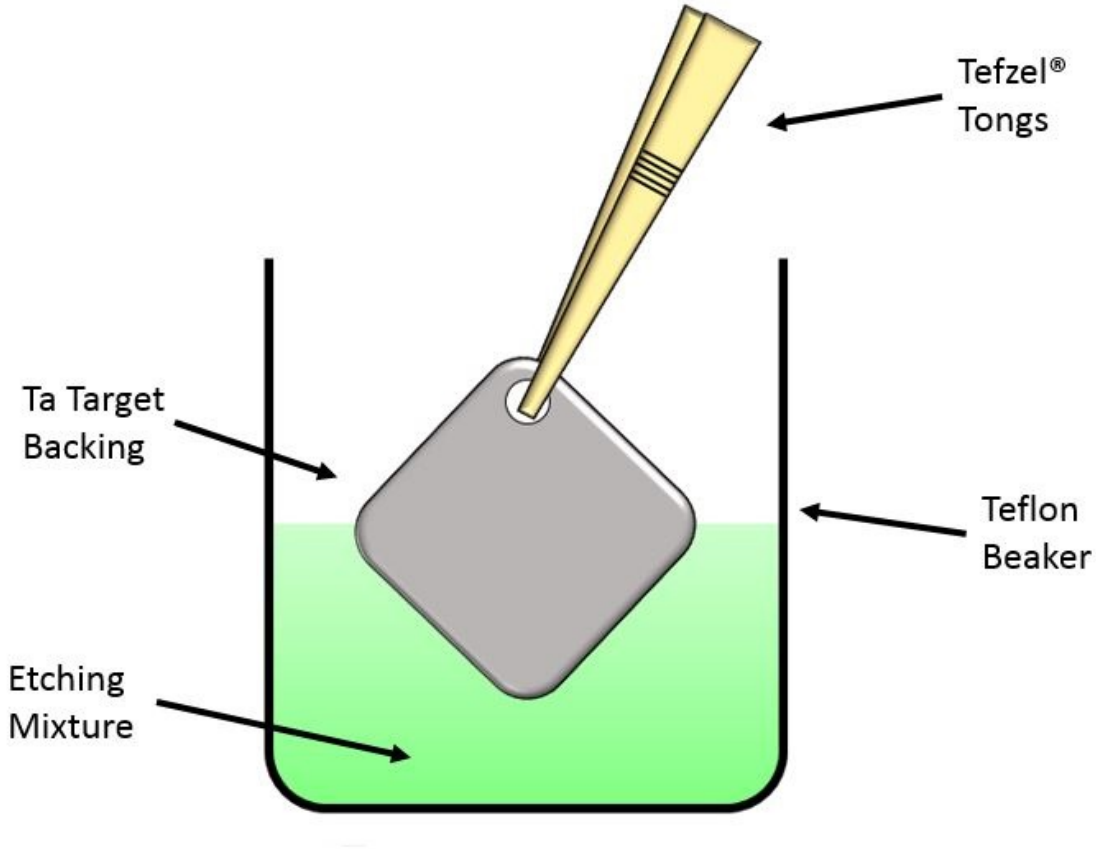

Figure 4.3: Illustration of the etching procedure.

4.1.2 Resistive Heating

Even after wet etching removes surface impurities, additional contaminants remain within the backings, usually from the metallurgical processing responsible for purifying the metal. To remove these, the high vacuum oil-free evaporator system at LENA (shown in Fig. 4.4) was used to resistively heat the backings to drive out remaining contaminants. A single tantalum backing was held between two copper electrodes with internal water cooling. The tantalum was held under a high vacuum (10^{-7} Torr) created by a cryogenic cooling pump. Approximately 300 A of current was passed through the backings, heating them and causing them to glow a bright, uniform orange. Gas pressure within the evaporator would rise to approximately 10^{-6} Torr while outgassing, and would return to normal operating pressures of 10^{-7} Torr after approximately 15 minutes of operation, indicating that the contaminates had been purged. The current would then be slowly turned down, and after the target cooled off (approximately an hour) it was returned to the target vacuum box shown in Fig. 4.2.

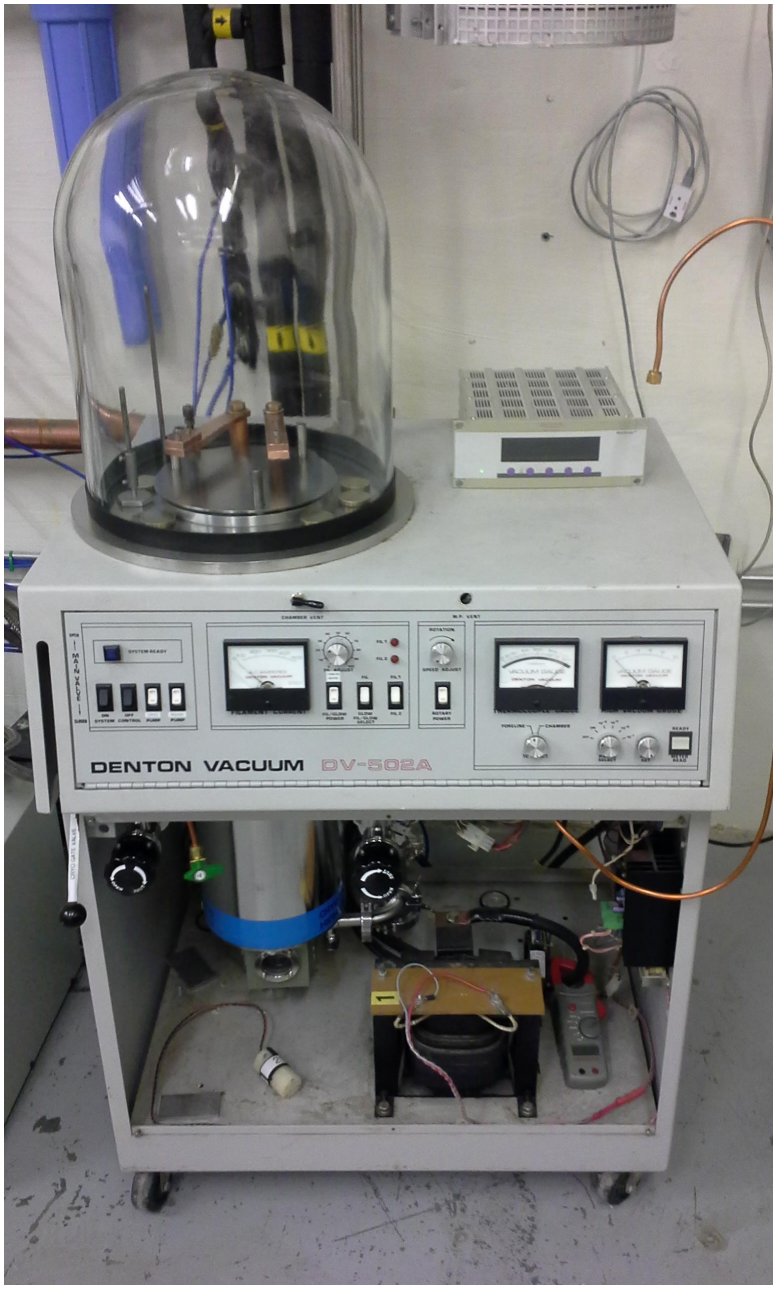

Figure 4.4: The high vacuum oil-free evaporator system at LENA. Target backings are held between the copper electrodes inside the bell jar and subjected to high current for resistive heating.

4.1.3 Dose Calculations

The cleaned tantalum backings were implanted with ^{22}Ne using an Eaton NV-3206 ion implanter described in Chapter 3. To maximize the number of implanted ^{22}Ne ions,

the target was implanted until saturation of the neon was reached. The stoichiometry is defined as the ratio of active target nuclei to the number of nuclei that do not participate in the reaction of interest, and previous work in the LENA lab involving implantation of ^{22}Ne in tantalum showed a saturation stoichiometry of $\approx$ 3:1 Ta:Ne. The charge accumulation necessary to reach ^{22}Ne saturation of the target backings is given by:

$$Q = \frac{N_n}{\epsilon}(1.602 \times 10^{-19} C) \tag{4.1}$$

Where N_n is the number of neon atoms striking the target backing, and ϵ is the implantation to sputtering efficiency (estimated in this work to be a conservative 0.25). The value of N_n is determined by

$$N_t = \frac{a}{b}\frac{\rho_t V N_A}{A_n} \tag{4.2}$$

Where $\frac{a}{b}$ is the expected stoichiometry (3 in this case), ρ_t is the mass density of the target backing, N_a is Avogadro's number, A_n is the atomic mass of the backing atoms, and V is the volume, defined as:

$$V = \pi r^2 d \tag{4.3}$$

where r is the radius of the implantation region (in this case, r is set by the collimator to be 1.27 cm), and d is the penetration depth of the implanted ions. In this case, d was calculated using the SRIM-2008.04 computer application [Ziegler and Biersack, 2008]. For the 30 keV targets used in this study, the necessary dose to achieve saturation was calculated to be $\approx$ 0.2 C of charge.

4.2 ^{22}Ne Implantation

Implantation for the initial tantalum targets was performed using the Eaton ion implanter (see Chapter 3) with an average beam current to target of ≈ 20 μA. At this beam intensity, it took ≈ 5 hours to implant each target to ≈ 0.35 C, which is above the saturation point to account for uncertainty in calculated dosage required. A total of four targets were produced to explore the possibility of reducing carbon contamination that interfered with previous measurements of the ^{22}Ne(α,n)^{25}Mg and ^{22}Ne(α,γ)^{26}Mg reactions. Table 4.1 shows the settings for the implantation of $^{22}Ne^{+}$ into the solid backings used for the four targets. (as mentioned in Chapter 3, the Eaton implanter has been decommissioned. The parameters here are only to allow comparison between these settings used for the targets in this study, and the settings listed in prior dissertations that used the Eaton implanter).

Parameter	Value
Implantation energy	25.0 keV
Chamber vacuum	4×10^{-7} Torr
Beamline vacuum	5×10^{-7} Torr
Scan amplitude X	8 o'clock
Scan amplitude Y	8 o'clock
Beam centering X	2 o'clock
Beam centering Y	9 o'clock
Focus X	2 o'clock
Focus Y	2 o'clock
Filament current	6.00 rotations
Magnet current	1.78 rotations
Discharge current	4.5 A
Extraction current	5.0 mA
Collimator current	15 μA
Average beam current	25 μA
Accumulated charge	0.35 C

Table 4.1: Typical tuning parameter settings for implantation of $^{22}Ne^{+}$ into tantalum with the UNC ion implanter. Settings using "o'clock" reference the position of the dial relative to a clock face. It should be noted that filament current begins at 6.00 rotations, but steadily decreases over the course of the run as the filament deteriorates.

4.3 Carbon Contamination

Past solid target measurements of the ^{22}Ne(α,n)^{25}Mg reaction discovered large neutron backgrounds originating from the ^{13}C(α,n)^{16}O reaction [Giesen et al., 1993]. Carbon is typically deposited on the targets during implantation, and can be produced from several sources. Carbon buildup has been observed on targets implanted at UNC, and is hypothesized to originate from the glue within the acceleration column, outgased from rubber O-rings, and especially from the oil diffusion pump, which has been identified as a major source of carbon contamination in other implanters [Tsai et al., 1979]. Figure 4.5 shows an implanted target and non-implanted backing. The red arrow points to the region of implantation demarcated by the slightly discolored circle is thought to be caused by contaminants not captured by the liquid nitrogen cold trap that coalesce on the target backing. The implantation beam heats the target, baking the carbon on the surface and driving some of it into the tantalum target backing. In an attempt to reduce neutron background caused by the ^{13}C(α,n)^{16}O reaction, three different cleaning methods were tested to eliminate surface carbon: piranha solution, pentane, and O_2 plasma cleaning.

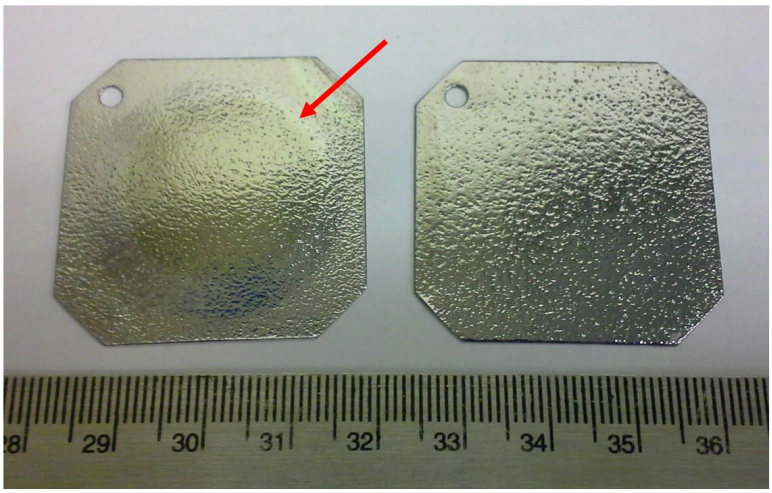

Figure 4.5: A contrast adjusted image of an implanted target (on the left) and a non-implanted backing (on the right). The red arrow indicates the region of implantation, visible as a slightly darker ring in the center of the target backing.

4.3.1 Piranha Solution Cleaning

The first cleaning method used was a piranha solution, which is highly acidic, and a powerful oxidizer. It is traditionally a 3:1 mixture of sulfuric acid (H_2SO_4) and 30% hydrogen peroxide (H_2O_2). The piranha solution undergoes an energetically favorable dehydration of hydrogen peroxide to form hydronium ions, bisulfate ions, and atomic oxygen via:

$$H_2SO_4 + H_2O_2 \rightarrow H_3O^+ + HSO_4^- + O \tag{4.4}$$

The free radical oxygen species in this reaction is extremely reactive, and allows the solution to dissolve elemental carbon, which is normally difficult to remove from delicate surfaces (like an implanted target) because of the high chemical stability and typically graphite-like hybridized bonds of carbon allotropes. The most likely way the free radical oxygen can attack the carbon is by disrupting the stable carbon-to-carbon surface bonds, allowing the oxygen and carbon to form a carbonyl group, as in the process:

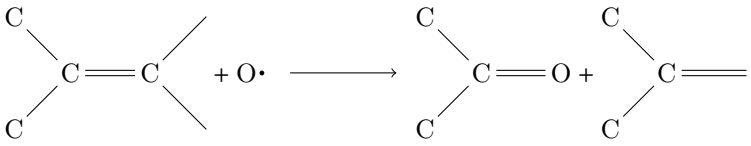

In this situation, an electron bonding pair from the central carbon is essentially "stolen" by the oxygen. This allows further reactions to convert the carbonyl groups to carbon dioxide, such as through the process:

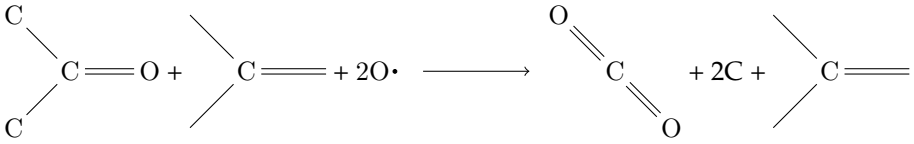

which operates on the order of minutes.

A piranha solution was mixed according to the above description in a teflon container placed in an ice bath. The mixture was kept under a fume hood to minimize exposure to

hazardous fumes. One of the four tantalum targets mentioned in Section 4.2 was placed in the piranha solution and left $\approx$ 30 minutes to ensure all carbon contaminants fully dissolved.

4.3.2 Pentane Cleaning

The second method for carbon cleaning used the organic solvent pentane. Pentane is a colorless alkane with a low odor, high volatility, rapid evaporation rate, and the chemical formula C_5H_{12} [Barton, 1991]. Pentane has entirely non-polar bonds (C-C and C-H only), making it a good solvent for non-polar contaminants, such as carbon.

A target was placed with the implanted face up on a clean work surface. Pentane was applied to a Kimwipe which was slowly dragged across the surface of the implanted region of the target. This process was repeated while constantly changing wipes and reapplying pentane. After $\approx$ 10 minutes of cleaning, blackish streaks of (what is presumed to be) carbon became visible (see Fig. 4.6). This process was continued until no more streaks were observed ($\approx$ 40 minutes).

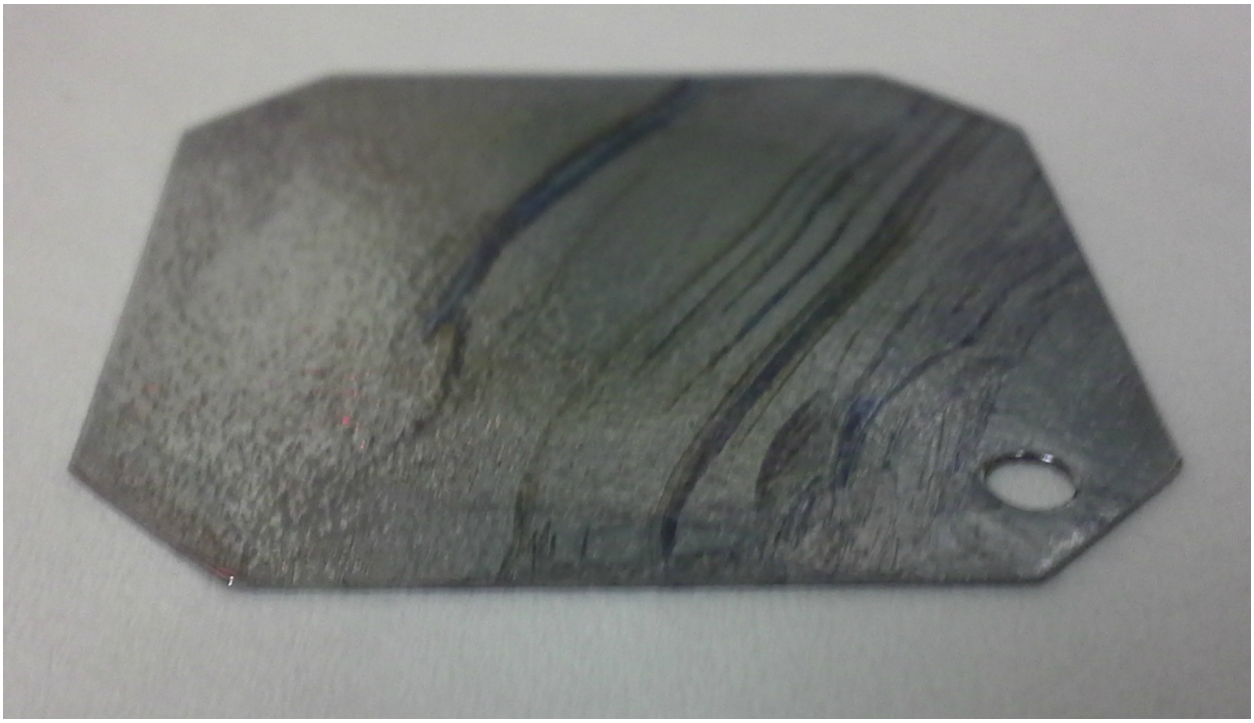

Figure 4.6: An implanted target in the process of pentane cleaning. The black streaks are assumed to be carbon or carbon composite buildup.

4.3.3 O_2 Plasma Cleaning

A final method of carbon cleaning was the use of an oxygen plasma, which cleans surface contaminants through two processes. The plasma's activated species produce photons in the short wave ultraviolet range, which is very effective at breaking apart organic bonds (C-H, C-C, C=C, C-O, etc.), allowing the plasma (O, O^+, O^-, O_2^+, O_2^+-, O_3, O_3^+, O_3^-, metastable excited states, and free electrons [Pizzi and Mittal, 2003]) to form H_2O, CO, CO_2, and light hydrocarbons. These new compounds have relatively high vapor pressures, and quickly evaporate into the vacuum-like pressures of the plasma chamber.

Figure 4.7: The Grow Research AutoGlow plasma cleaner used to eliminate carbon.

One of the implanted tantalum targets was taken to Chapel Hill Analytical and Nanofabrication Laboratory (CHANL). The target was placed in CHANL's Grow Research AutoGlow O_2 plasma cleaner (shown in Figure 4.7), and left inside for ≈ 15 minutes. No visible changes to the surface of the target were detected.

4.3.4 Carbon Comparison

The JN accelerator (see Chapter 3 for more information on the JN) was not operational during the beginning of this experiment, preventing a measurement of the carbon on the targets or the quantity of implanted neon before cleaning. The consistency of charge accumulated across targets allows the assumption of equal carbon deposition/implantation for each. Additionally, past use of ^{22}Ne implanted tantalum targets [Kelly, 2016] fabricated in the same manner as this study allows for the assumption of constant ^{22}Ne yields for each target. Because of the lack of initial measurements and the above assumptions, the targets can only be compared to each other to look for large deviations in carbon

content and implanted ^{22}Ne.

Yield curves of the implanted ^{22}Ne targets were made using the ^{22}Ne(p,γ)^{23}Na reaction. The 479.3(8) keV resonance [Kelly, 2016] was used to measure the yield curves shown in Fig. 4.8. The 6270 keV γ-ray from the $9252 \rightarrow 2982$ keV [Longland et al., 2010a] primary transition in ^{23}Na was monitored to determine the yield.

A Markov Chain Monte Carlo (MCMC) code developed in `R` by Richard Longland called `YCurve.R` was used to fit and analyze the yield curve for each target (shown in Fig. 4.8). This code uses an iterative minimization function to calculate parameters such as resonance energy, beam width, target thickness, straggling constant, and integrated yield. The results of the yield curves indicate there is no significant degradation of ^{22}Ne in the targets as a result of the various cleaning methods.

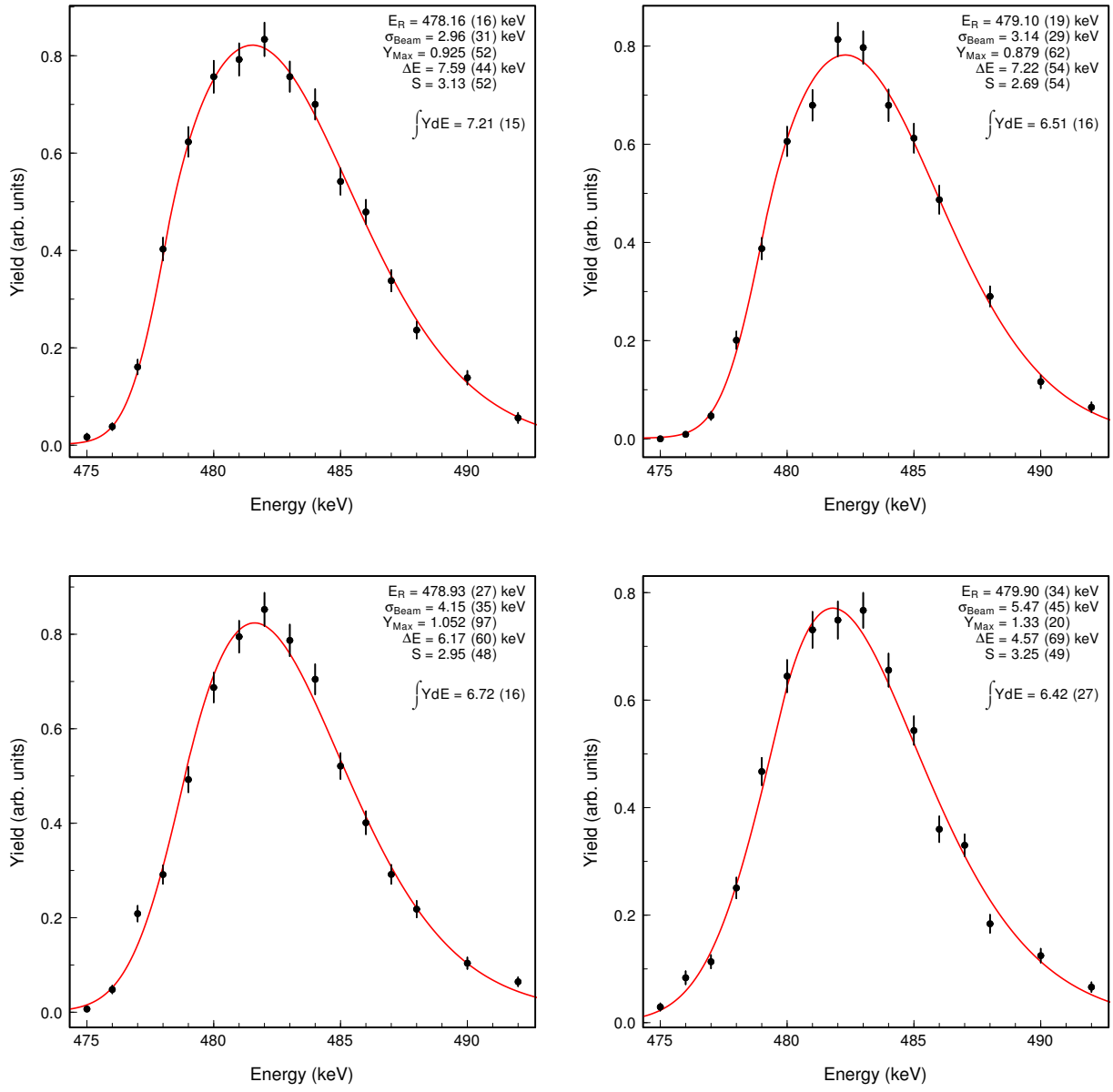

Figure 4.8: ^{22}Ne(p,γ)^{23}Na Yield curves for targets cleaned through various methods. Black data points were measured using the JN Van de Graaff accelerator at LENA, and the red fit was generated using an MCMC fitter. The fitter uses arbitrary units for yield, which were counts/μC in this case. The γ-ray monitored for these measurements was the 6270 keV γ-ray from the $9252 \rightarrow 2982$ keV primary transition in ^{23}Na. (Top left) yield curve for target cleaned using pentane (see Section 4.3.2). (Top right) yield curve for target cleaned using piranha solution (see Section 4.3.1). (Bottom left) yield curve for target cleaned using oxygen plasma (see Section 4.3.3).(Bottom right) yield curve for uncleaned target. In the upper right of each plot there is listed in order: resonance energy, beam energy width, maximum yield, target width, straggling, and integrated yield. There appears to be no significant negative effect on the ^{22}Ne yield using the various cleaning methods.

To measure the carbon contamination on each target, the target chamber (see Chapter 3) was removed and cleaned with Bear-Tex, ethanol, and acetone to remove any carbon deposited near the target (the components cleaned are shown in Fig. 4.9). After cleaning the collimator, carbon was measured using the ^{12}C(p,γ)^{13}N direct capture reaction at 435 keV beam energy. This energy was chosen to avoid resonances in both ^{22}Ne and ^{12}C. The direct capture of ^{12}C(p,γ)^{13}N was measured using an emitted 2339 γ-ray.

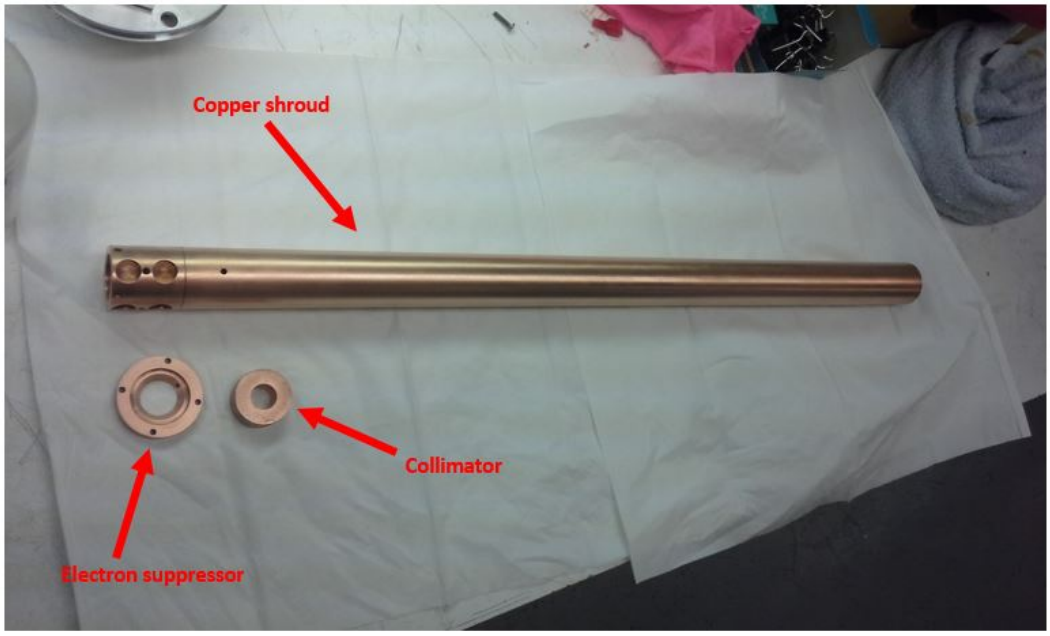

Figure 4.9: The dissembled target chamber at LENA. The copper shroud, electron suppressor, and collimator are all shown here. All three components were cleaned with Bear-Tex, ethanol, and acetone to remove carbon.

Figure 4.10 shows the results from the carbon test. Targets cleaned with pentane, O_2 plasma, and piranha solution were compared to targets without any cleaning. No significant reduction in carbon content was detected between the cleaned targets, and the uncleaned target. An argument could be made that the cleaning process actually increased carbon contamination, but some of the cleaning methods (such as the plasma cleaning) does not have a known mechanism by which carbon could be deposited. It is possible that initial carbon contents before cleaning varied slightly, and cleaning either resulted

in small or no reduction of the carbon. This indicates the presence of significant sub-surface carbon beyond the influence of conventional cleaning methods. The carbon was most likely deposited onto the target during implantation, and then driven into the target backing by the ^{22}Ne beam.

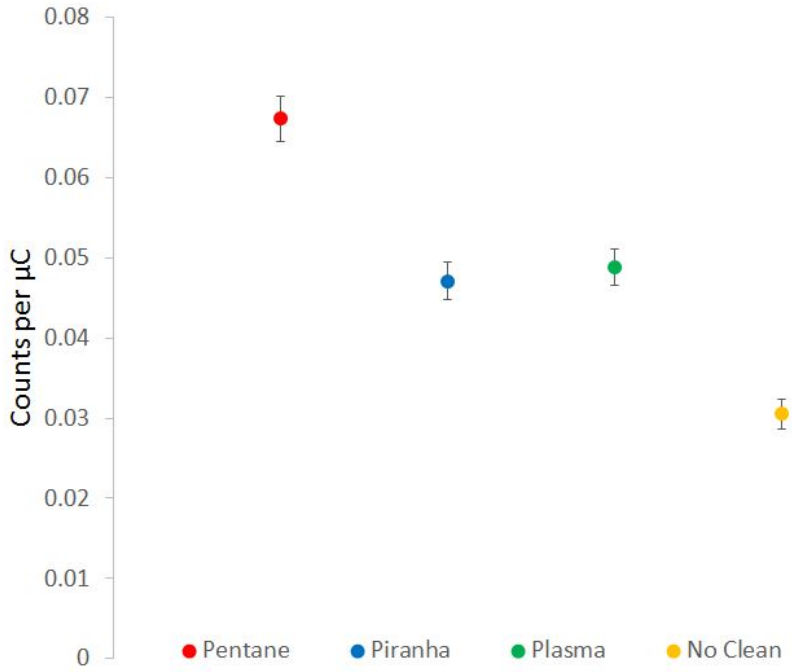

Figure 4.10: Relative comparison of measured carbon on 4 targets with different cleaning methods. Carbon was monitored using the 2339 keV γ-ray from direct capture of ^{12}C(p,γ)^{13}N reaction at 425 keV beam energy. Carbon was not significantly lower in the cleaned targets, indicating that carbon contamination is not limited to the surface.

It was determined that no significant carbon reduction could be achieved through surface treatment of the targets. This inability to eliminate the carbon contamination motivated the development of the fast neutron spectrometer detailed in Chapter 5.

4.4 Target Blistering

It was discovered during initial attempts to measure the ^{22}Ne(α,γ)^{26}Mg reaction that standard tantalum backings experienced greater-than-expected degradation after 0.1 C

of accumulated charge under $\approx$ 850 keV α-particle bombardment. The phenomenon responsible for this is known as *blistering*, and occurs when small bubbles of helium form in the target [Marochov and Goodhew, 1988, Van Veen et al., 1983]. Blistering has also been shown by others to cause significant target degradation [Erents and McCracken, 1973, Evans, 1977, 1978, Johnson et al., 1999, Kaminsky and Das, 1974].

Estimates for the amount of deposited charge needed to measure the ^{22}Ne(α,γ)^{26}Mg reaction with the detector setup used for this experiment made the use of these tantalum targets highly impractical. Other backing materials were explored in an attempt to identify a backing material capable of withstanding α-particle bombardment without blistering. A significant effort was made to develop a blister resistant target for this and future α-particle measurements. The research for the the blister-resistant targets has been published in [Hunt et al., 2018].

Figure 4.11 illustrates the effect and the resulting destruction of surface target material. High pressure helium bubbles from α-particle bombardment form within the metallic lattice, as depicted in part (a). Once enough pressure has built, the bubbles burst through the face of the target, destroying the surface of the target backing and resulting in a significant loss of implanted or evaporated target material, as illustrated in part (b).

Blistering is distinct from damage caused by excessive power deposition from intense particle bombardment on the target. Damage from excessive power deposition, referred to in this dissertation as *heat damage*, can occur with an incident beam of any particle type. Blistering only occurs when certain gases are implanted into metals, and usually results in burn marks on the target and a steady decrease of target material with continued ion bombardment.

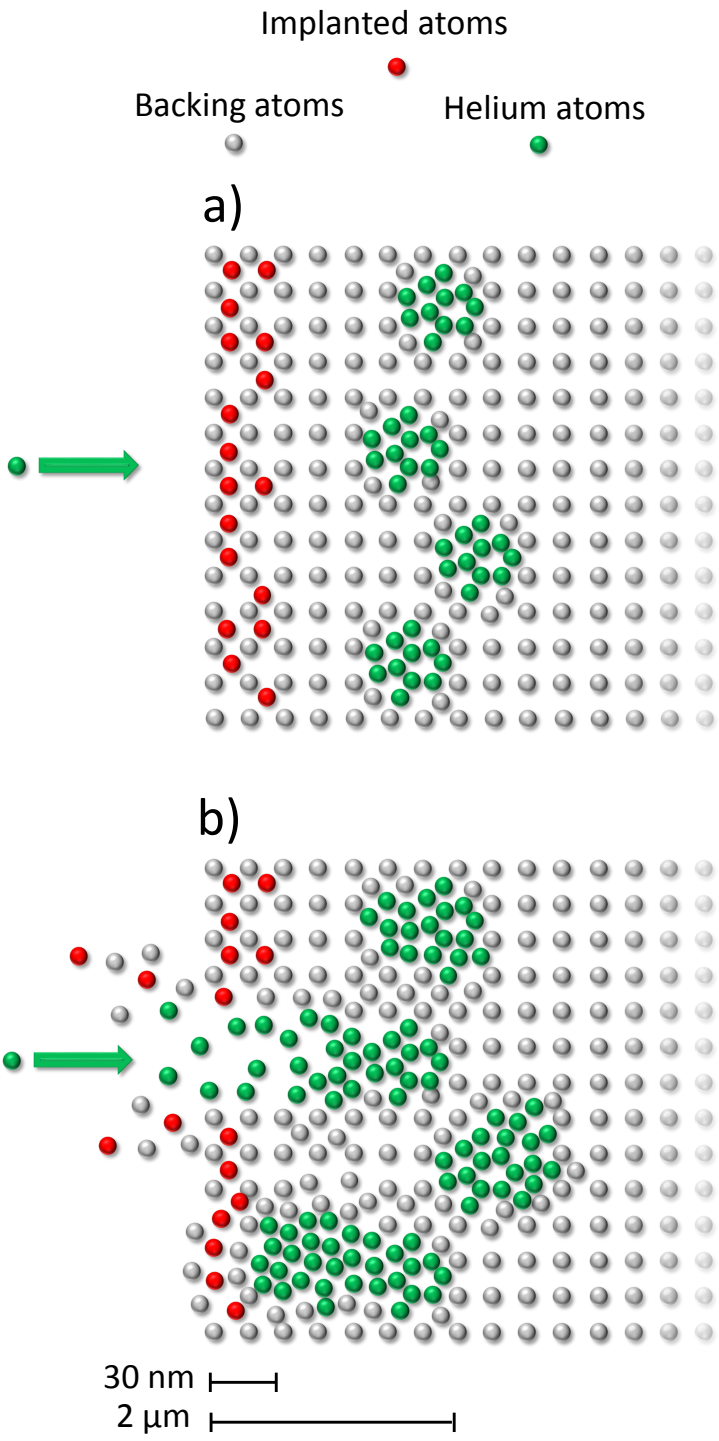

Figure 4.11: Illustration of blistering in a metal target of crystal structure. (Gray) Metal backing atoms; (Red) Implanted target atoms; (Green) Helium atoms. (a) Bubble formation during α-particle bombardment, but before blistering occurs. (b) Destruction of the surface of the implanted target once the helium bubbles grow large enough to rupture through the surface.

When helium is implanted into a metal, it migrates through the atomic lattice until it encounters a structural imperfection, called a loop dislocation. At a certain dose of implanted ions, the pressure inside the dislocation is sufficient to "punch" out of the loop dislocation (*loop punching*) to form a bubble. This limiting pressure is given by [Trinkaus, 1983]

$$P = \frac{2\gamma + \mu b}{R} \tag{4.5}$$

where γ is the surface free energy, b is the Burgers vector (representing the magnitude and direction of a lattice distortion resulting from a dislocation), μ is the sheer modulus, and R is the bubble radius. Typical pressures for bubble formation using this model range from 9 GPa in aluminum to 40 GPa in molybdenum.

If helium is implanted continuously after the formation of a bubble, the bubble will continue to grow. It has been shown [Mansur and Coghlan, 1983] that the modified van der Waals equation of state, given by

$$P' = \frac{nkT}{V - nB} \tag{4.6}$$

accurately approximates the behavior of helium inside the bubble. Here, P' is the pressure inside the bubble, T is the temperature, B is the van der Waals volume correction coefficient, k is the Boltzmann constant, and n is the particle number in moles.

At bombarding energies in the million electron volt range, small bubbles ($R < 2$ nm) form close to the metal backing surface (within ≈ 5 μm). Continuous α-particle bombardment will cause the bubbles to grow, according to Equation (4.6) with internal pressures limited by Equation (4.5). With enough bombardment, the bubbles rupture through the surface of the target, resulting in a significant loss of evaporated or implanted target material.

Figure 4.12 depicts the progression of blistering in a titanium backing implanted with ^{22}Ne ions during bombardment with 900 keV α-particles. Panels (a), (b), (c), and (d) show

the same target after an accumulated ion beam charge of 0.2 C, 0.4 C, 0.6 C, and 0.8 C, respectively. The images demonstrate the visible changes to the surface of the target, but it should be noted that significant degradation of implanted target material (^{22}Ne; see below) can be observed with as little as 0.1 C of accumulated charge.

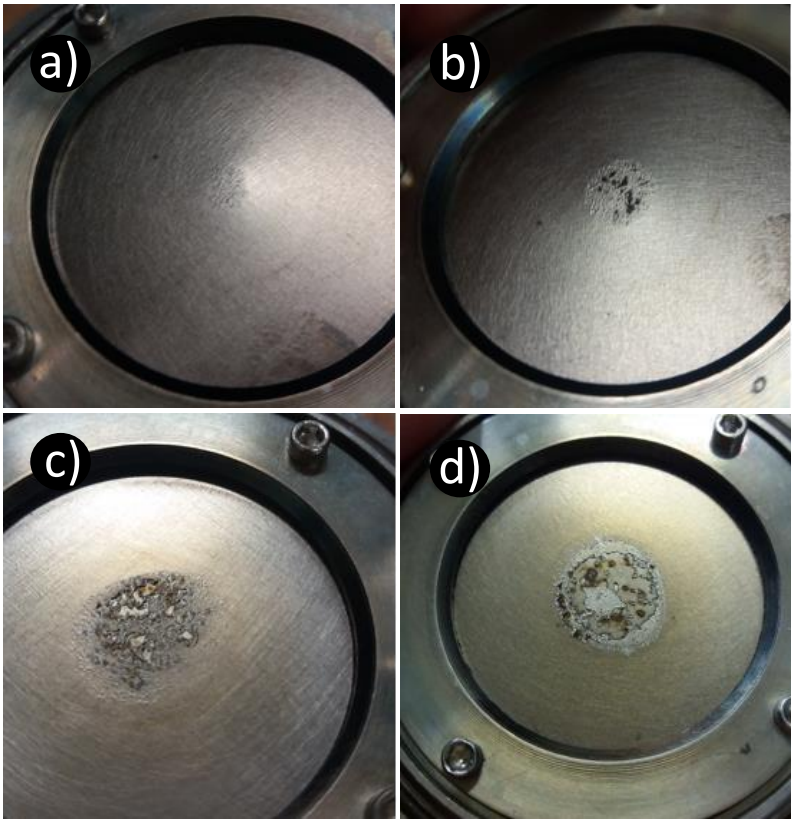

Figure 4.12: Example of the progression of blistering in a titanium backing implanted with ^{22}Ne ions caused by the bombardment with α-particles of 900 keV energy. The α-particle intensity was kept low, near 30 μA, to prevent heat-related damage to the target. Panels (a), (b), (c), and (d) correspond to accumulated charges of 0.2 C, 0.4 C, 0.6 C, and 0.8 C, respectively. The effects of blistering in the center region become more apparent with increasing charge accumulation. After an accumulated charge of 0.8 C, the target is heavily damaged.

The targets in this portion of the dissertation were fabricated by implanting ^{22}Ne ions into backings using both the Eaton NV-3206 and the ECR source discussed in Chapter 3. All targets in this study were implanted at an energy of 75 keV using the maximum beam intensity available at each accelerator. Targets were tested and characterized using the JN

Van de Graaff accelerator also discussed in Chapter 3. Like the yield curves produced in Section 4.3.4, the targets in this section were monitored using the the 479.3(8) keV (laboratory frame) resonance in the ^{22}Ne(p,γ)^{23}Na reaction. The γ-ray monitored for the yield curve had an energy of 6270 keV, corresponding to the 9252 $\rightarrow$ 2982 keV primary transition in ^{23}Na [Longland et al., 2010a]. The γ-rays were measured using LENA's coaxial high purity germanium (HPGe) detector discussed in Chapter 5.

4.5 Blister-Resistant Targets

To illustrate the loss of target atoms caused by blistering in a typical nuclear reaction experiment, a target was made by implanting ^{22}Ne ions into one of the tantalum backing (described earlier in this chapter) with an incident dose of $\approx$ 0.45 C. The yield curve (i.e., the ^{22}Ne concentration profile), measured using the the 479 keV resonance in ^{22}Ne(p,γ)^{23}Na, is shown in Figure 4.13a. The ^{22}Ne has a thickness of $\approx$ 10 keV, and a stoichiometry of $\approx$ ^{22}Ne$_1$Ta$_3$. After this measurement, the target was exposed to an α-particle beam of 900 keV energy and 30 μA intensity, resulting in a total accumulated charge of 0.5 C. Another attempt to measure a ^{22}Ne(p,γ)^{23}Na yield curve was made, but only upper limits for the intensity of the 6270 keV γ-ray could be determined (blue data points in Figure 4.13a). In other words, blistering during α-particle bombardment had removed all implanted ^{22}Ne atoms.

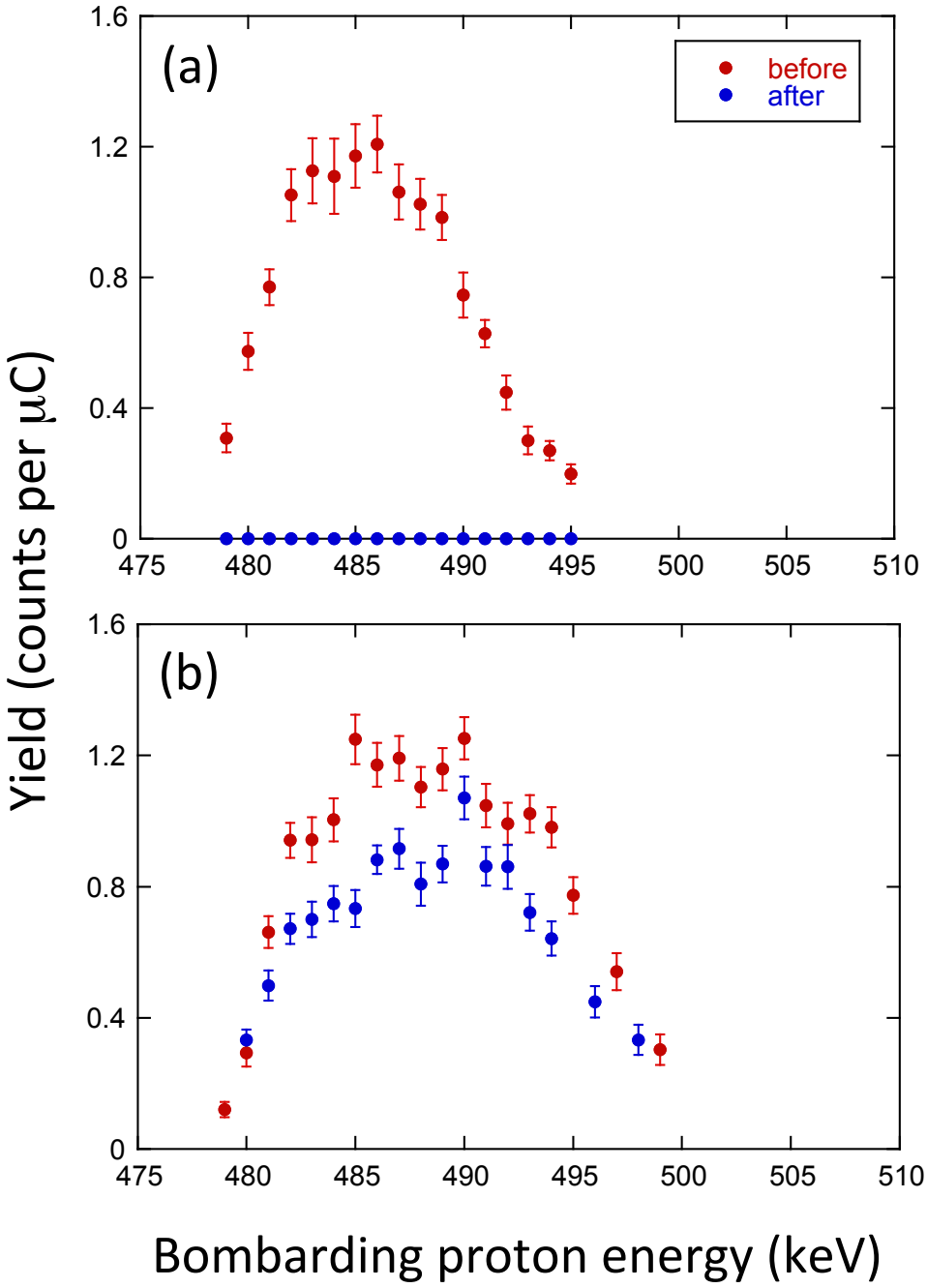

Figure 4.13: Yield curves for the 479 keV (laboratory frame) resonance in ^{22}Ne(p,γ)^{23}Na, measured by using the observed intensity of the 6270 keV γ-ray from the decay of ^{23}Na. The red and blue data points correspond to the yield before and after α-particle bombardment. (a) Tantalum sheet implanted with ^{22}Ne ions. Notice that only upper limits for the yield could be obtained after α-particle bombardment with an accumulated charge of 0.5 C (blue data points), demonstrating the severe loss of ^{22}Ne concentration caused by blistering. (b) Fused silica target implanted with ^{22}Ne ions. The maximum yield declines by $\approx 20\%$ after α-particle bombardment with an accumulated charge of 0.65 C.

The following subsections describe the fabrication and testing of three types of blister-resistant targets, the final of which was ultimately used to measure the ^{22}Ne(α,γ)^{26}Mg reaction in this dissertation.

4.5.1 Fused Silica Targets

Fused silica, sometimes referred to as fused quartz, is a glass (amorphous silicon dioxide) that is formed by melting a silicon-rich chemical precursor in combination with flame oxidation at temperatures around 1700 K [Voorhees et al., 1974]. The lack of additives typically used in glass-making to lower the melting point (such as borontrioxide, metaphosphates, or sodium compounds) results in a clear glass that is low in contaminants and has a very high gas diffusion coefficient [Lee et al., 1962, Masaryk and Fulrath, 1973, Swets et al., 1961]. The high diffusion coefficient (the exact value for the helium diffusion coefficient is dependent on temperature, with ranges of $\approx$ 0.25 - 600 $\times$ 10^{-7} cm^2/s for temperatures between 25 - 1000 C [Swets et al., 1961]) allows the implanted, electrically-neutralized α-particles to disperse throughout the backing and into the water cooling system on the back face of the target, preventing bubble formation and associated blistering. The situation is shown schematically in Figure 4.14.

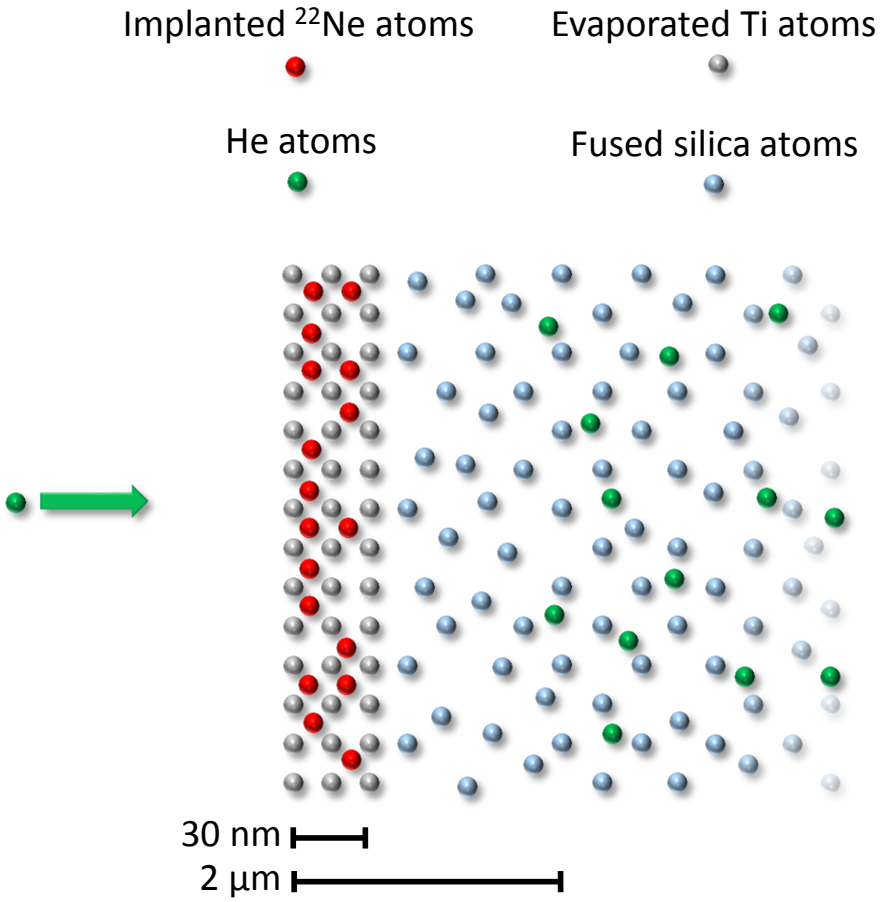

Figure 4.14: Structure of a fused silica target. (Light blue) Fused silica backing atoms forming an amorphous matrix; (Gray) Evaporated Ti atoms; (Red) Implanted ^{22}Ne atoms; (Green) Helium atoms. The incident helium atoms diffuse quickly through the fused silica matrix, which prevents high-pressure bubbles from forming. Compare this situation with the one depicted in Figure 4.11.

Fused silica has long been studied as a material to contain high level nuclear waste, in part because the high helium diffusion coefficient reduces the damage from blistering [Matzke and Vernaz, 1993]. In addition to high gas diffusion rates, fused silica can be made chemically pure, thereby reducing the ion-beam-induced background in a nuclear reaction measurement. For more details on the types of fused silica glass and their associated impurities, see [Ferreira Nascimento and Zanotto, 2007].

The fused silica backings used in our experiment were discs with a diameter of 3.81

cm, and a thickness of 1.59 mm, made of polished GE 124 glass[1] purchased from Technical Glass Products®. An image is shown on the right side in panel (a) of Figure 4.15. A thin surface metal layer must be evaporated onto the fused silica backing to hold the implanted ^{22}Ne atoms, since noble gases implanted directly into the fused silica would diffuse through the matrix. This layer must be thin enough to allow the α-particles to pass through before coming to a stop within the fused silica backing, and also be thick enough to hold the desired layer of implanted target material (Figure 4.11). Titanium was chosen for this study because it has a lower effective stopping power than most metals, resulting in a higher nuclear reaction yield [Iliadis, 2015].

The projected range of 900 keV α particles in titanium metal is ≈ 2 μm, according to the SRIM package [Ziegler et al., 2013]), while the projected range of ^{22}Ne ions implanted at 100 keV is ≈ 30 nm. This lead to a 200 nm thick layer of titanium to be chosen for evaporation onto the fused silica backing. This layer also allowed for integrating the current deposited by the ion beam, despite the fact that fused silica is an electrical insulator, by providing the charge deposited by the incident α particles a short path to ground (≈ 3 μm, the penetration depth of the α particles in fused silica after losing energy in the titanium layer).

The smooth surface of the fused silica has a tendency to cause the evaporated titanium layer to peel away. For this reason, the fused silica backing was "frosted" using a 20 psi glass bead blaster before evaporation. This process creates a pitted glass surface to which the titanium can better affix. An image of a frosted backing is shown on the left side in panel (a) of Figure 4.15. It should be noted that excessive frosting of the glass can weaken the backing. If high pressure (> 40 psi) water is used for target cooling, frosting should be kept to a minimum to prevent the backing from fracturing under the differential pressure of the vacuum on one face and water cooling on the opposite face.

[1]The manufacturer provided the following tracer element concentrations (in parts-per-million): OH^- (33); Al (20.3); Ca (1.8); Fe (1.9); Li (1.0); Mg (0.5); Na (1.3); Ti (1.4).

After a thin titanium layer was evaporated onto the frosted glass surface, it was implanted with ^{22}Ne ions using a dose of ≈ 1 C using the Eaton ion implanter (see Chapter 3). Images of the evaporated and implanted surfaces are shown in panels (b) and (c) of Figure 4.15.

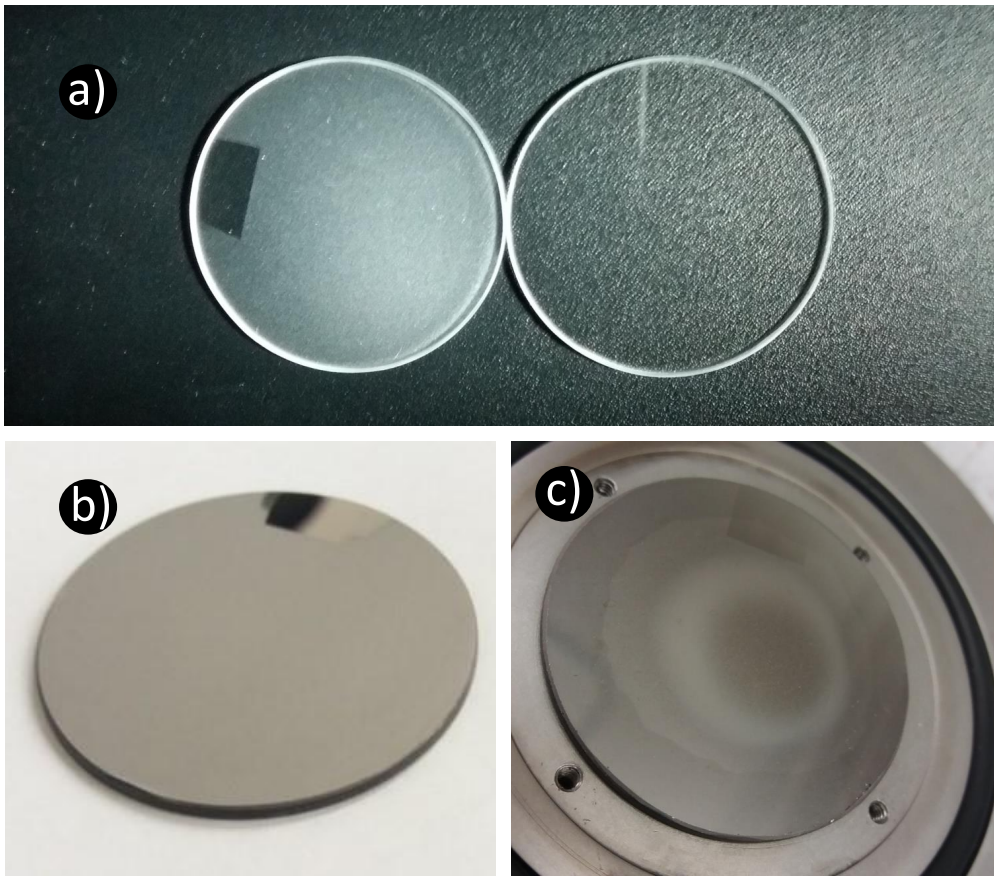

Figure 4.15: Preparation of a fused silica target. (a) Fused silica backings before (right) and after (left) being frosted using a glass bead blaster. (b) Frosted fused silica backing after evaporation of a thin titanium layer. (c) Target after implantation of ^{22}Ne into the thin titanium surface layer.

Yield curves of the ^{22}Ne(p,γ)^{23}Na reaction are displayed in Figure 4.13b. The red points show the the yield before any α-particle bombardment. This target is thicker compared to the implanted tantalum target (Figure 4.13a) because of the larger range of ^{22}Ne ions in titanium compared to tantalum. However, the heights of the yield curves (red points in Figure 4.13) are comparable. For the fused silica target, the measured maximum yield

corresponds to a stoichiometry of $\approx {}^{22}Ne_1Ti_5$.

The fused silica target was then exposed to a 900-keV energy α-particle beam with an intensity of 30 μA. The total accumulated charge was 0.65 C. No visible marks of blistering, such as those shown in Figure 4.12, were observed on the target surface after α-particle bombardment. A second yield curve was measured after α-particle bombardment, which is displayed as the blue data points in Figure 4.13b. It can be seen that the maximum yield degraded by $\approx 20\%$ after α-particle bombardment. This result represents a significant improvement over the implanted tantalum target, which showed a complete loss of the implanted ^{22}Ne concentration after a similar accumulated α-particle charge.

Signs of heat damage (Section 4.4) in the form of minor burn marks on the surface and an odor of burnt metal were noticed when the target was removed from the vacuum chamber after α-particle bombardment. Fused silica has a relatively low coefficient of thermal conductivity ($\approx 2.7 \times 10^{-3}$ cal cm^{-1}sec^{-1}K^{-1} [Wray and Connolly, 1959]), which prevents these targets from withstanding high ion beam powers. Further tests indicated that heat damage starts to become noticeable at beam powers > 25 W cm^{-2}, corresponding to an α-particle beam of ≈ 30 μA intensity at 900 keV energy.

Fused silica targets exhibit significant blister resistance, and have low contaminant concentrations [Ferreira Nascimento and Zanotto, 2007]. Therefore, they will likely be advantageous in many nuclear physics experiments that utilize moderate beam intensities. However, these targets will be subject to heat damage at high beam powers in excess of 25 Wcm^{-2}, making them sub-optimal for measuring reactions requiring intense beam, such as the ^{22}Ne(α,γ)^{26}Mg.

4.5.2 Sintered Metal Targets

Sintered metal is produced by compacting and molding a mass of small metal grains, typically with pressure or heat, without reaching the melting point. The result is a porous matrix, and a target can be produced by implanting ions into the surface layer of such

a backing. The situation is illustrated in Figure 4.16, showing a titanium sintered backing (gray) with a ^{22}Ne-implanted surface region (red), which is exposed to a helium ion beam (green). The beam traverses the target region and comes to a stop deeper inside the sintered backing. High-pressure helium bubbles may form inside the grains. When the bubbles explode, they will burst into the inter-grain pore space, without damaging the implanted target surface. The size of the grains is important in this regard. If the grain size is smaller than the size of the bursting helium bubbles (< 100 nm; see Section 4.4), loop punching may not occur as helium atoms diffuse through the sintered matrix rather than congregate at lattice impurities (Section 4.4).

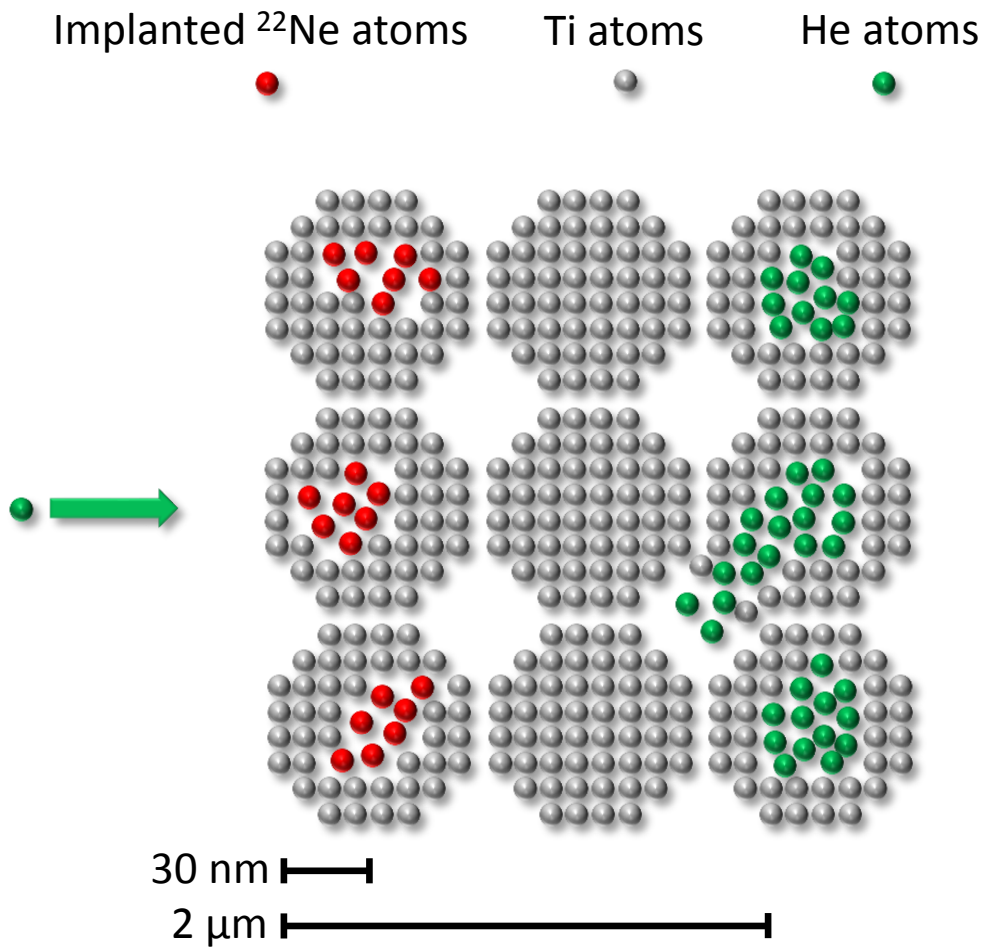

Figure 4.16: Structure of a sintered titanium target. (Gray) Titanium atoms, forming grains of a crystal structure, separated by cavities (pores); (Red) Implanted ^{22}Ne atoms; (Green) Helium atoms. Helium bubbles form in the titanium grains and burst into the inter-grain volume, preventing damage to the implanted target material near the surface.

Sintered metals are typically sold based on pore size (usually between 3 nm and 200 μm). We purchased sintered titanium metal discs with a diameter of 3.81 cm and a thickness of 1.59 mm from Porvair Filtration Group®. The average pore size was 100 nm.

Because of the porous nature of sintered metal, it is not possible to directly water cool the back of the target and maintain vacuum. Therefore, we sealed the back of the target by

affixing a 0.5 mm thick nickel sheet with Armstrong A-12 Epoxy® to the sintered titanium backing. The nickel sheet was then exposed to direct water cooling during our measurements. Figure 4.17 shows the round sintered titanium disk mounted atop a square nickel sheet.

Figure 4.17: Sintered titanium target. The round disk is the sintered titanium backing, and the irregular dark spot on the surface is the region with implanted ^{22}Ne atoms. The brown square around the disc is epoxy affixing it to the square nickel sheet. The target holder is seen behind the target.

The sintered titanium backing was implanted with singly-charged ^{22}Ne ions using a dose of ≈ 1 C using the ECR source modified to produce a neon beam (see Chapter 3). Yield curves of the 479 keV resonance in ^{22}Ne(p,γ)^{23}Na are displayed in Figure 4.18a. The red data points show the reaction yield before any α-particle bombardment. The target was then exposed to an α-particle beam of 400 keV energy and 50 μA intensity for a total

accumulated charge of 0.5 C.[2]

A second ^{22}Ne(p,γ)^{23}Na yield curve was then measured, which is shown as the blue data points in Figure 4.18a. It can be seen that the maximum yield decreased by $\approx 20\%$. The magnitude of the degradation is similar to the result for the fused silica target (Section 4.5.1 and Figure 4.13b), but nevertheless represents a significant improvement over the performance of an implanted tantalum sheet (Figure 4.13a) that exhibited a complete loss of implanted ^{22}Ne atoms after a similar incident α-particle dose.

[2]Problems with the accelerator prevented us from using an α-particle beam of 900 keV for this measurement. However, it has been shown that helium bubble formation in metals occurs at all bombarding energies [Marochov and Goodhew, 1988]. Furthermore, we have observed blistering with a 400-keV α-particle beam incident on an implanted tantalum target.

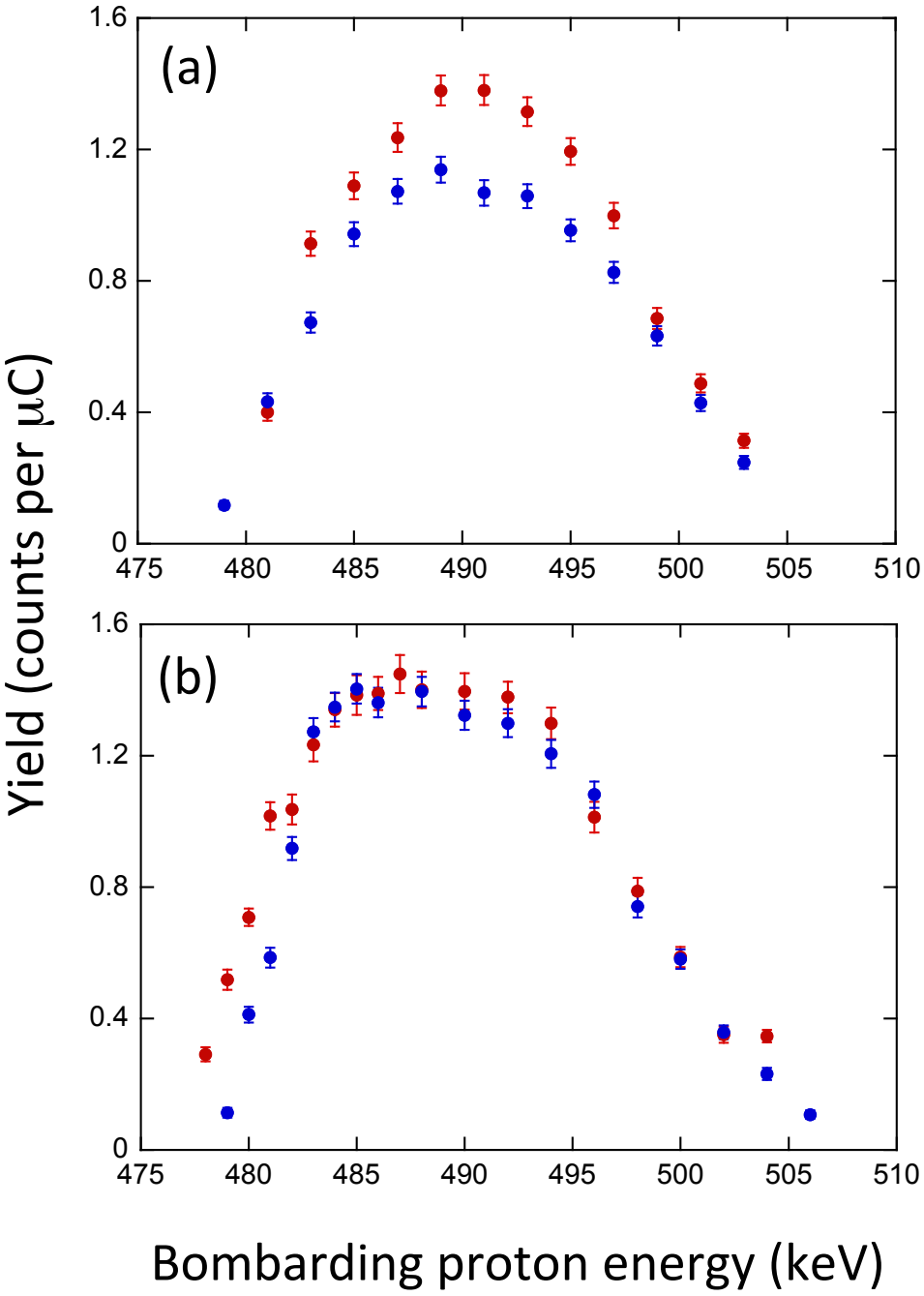

Figure 4.18: Yield curves for the 479 keV (laboratory frame) resonance in ^{22}Ne(p,γ)^{23}Na, measured by using the observed intensity of the 6270 keV γ-ray from the decay of ^{23}Na. The red and blue data points correspond to the yield before and after α-particle bombardment. (a) Sintered titanium backing implanted with ^{22}Ne ions. The maximum yield declines by $\approx 20\%$ after α-particle bombardment with an accumulated charge of 0.5 C. (b) Porous titanium target implanted with ^{22}Ne ions. Notice that the maximum yield height does not change after α-particle bombardment with an accumulated charge of 1.5 C.

No visible effects of blistering, such as those shown in Figure 4.12, were observed on the target surface after α-particle bombardment. However, as was the case for the fused silica target (Section 4.5.1), we observed minor burn marks and an odor of burnt metal after the target was removed from the vacuum chamber. Further tests showed that an α-particle beam power exceeding 20 W cm^{-2} will result in heat damage to the sintered titanium target. This effect, rather than blistering, is the suspected cause of the decline in the maximum yield shown in Figure 4.18a.

Sintered metals have been shown to have a lower thermal conductivity than solid metals. The thermal conductivity is inversely proportional to the porosity (up to a reduction factor of 3 at 45% porosity; see Figure 3 of [Kononenko et al., 1968]). This is partly because of the lower density, and partly because of insulating gases present within the intergrain space [Januszewski et al., 1977, Kononenko et al., 1968]. Insulating gases are absent in the environment of the vacuum chamber. Although the thermal conductivity of sintered metals in a vacuum is not well measured, it is likely that the lower density will contribute to a lower overall thermal conductivity when compared to a solid metal backing. The observed heat damage could potentially be mitigated by either utilizing a sintered metal of higher thermal conductivity (e.g., nickel or tantalum), or by using thinner sintered metal discs.

In addition, the epoxy affixing the sintered titanium backing to the water-cooled titanium sheet (Figure 4.17) will contribute to a decrease in the thermal conductivity of the target. A better method of sealing the back surface of the backing will likely improve the thermal conductivity.

4.5.3 Porous Metal Targets

When a metal layer is evaporated at a slow rate (several nanometers per minute) onto a heated metal surface, it can form a porous structure of interlocking metal crystals [Bauer,

1958], also called porous metal. If the evaporated layer extends beyond the range of incident α particles, they come to rest within the interlocking crystal matrix. Helium bubbles will likely not form in such a medium during α-particle bombardment if the crystals are smaller than the typical diameter of helium bubbles in solid metals (Section 4.4). If, on the other hand, the crystals are larger than the helium bubbles, the latter will burst into the inter-crystal volume, thereby preventing blister damage to the implanted or evaporated material at the target surface.

A target with a porous titanium surface layer was fabricated as follows. A thick (> 3 μm) layer of titanium was first evaporated onto a 0.5 mm thick titanium backing at a rate of ≈ 7 nm per minute. Subsequently, ^{22}Ne ions were implanted with the ECR neon beam into the porous surface with an incident dose of ≈ 1 C. The morphology of the target surface will be discussed in Section 4.5.4.

Yield curves of the 479 keV resonance in ^{22}Ne(p,γ)^{23}Na are displayed in Figure 4.18b. The red data points show the reaction yield before any α-particle bombardment. The target was then exposed to an α-particle beam of 900 keV energy and 50 μA intensity for a total accumulated charge of 1.5 C. A second ^{22}Ne(p,γ)^{23}Na yield curve was then measured, which is shown as the blue data points in Figure 4.18b. It can be seen that the maximum yield did not change as a result of helium beam exposure.

We did not observe any visible signs of blistering on the target surface. Neither did we notice any signs of heat damage in the form of burn marks on the target surface or an odor of burnt metal after removing the target from the vacuum chamber. The porous titanium target could withstand an α-particle beam power of 40 W cm^{-2}, corresponding to a bombarding energy of 900 keV and an intensity of $\approx$ 50 μA. Further tests showed that higher α-particle beam intensities resulted in signs of heat damage in the form of burn marks on the target surface. It appears likely that the heat damage could be reduced by increasing the thermal conductivity, either by using an improved target cooling design or by preparing porous backings of metals with a higher thermal conductivity.

Table 4.2: Summary of present results. All targets were implanted with ^{22}Ne ions of 75 keV energy and incident dose of between 0.5 and 1 C.

Target/ backing	Charge/energy[a] (C)/(keV)	Beam power[b] (Wcm^{-2})	Target loss[c] (%)
Ta	0.50/900	40	≈ 100
fused silica	0.65/900	25	18 ± 5
sintered Ti	0.50/400	20	22 ± 7
porous Ti	1.5/900	40	≈ 0

[a] Accumulated charge and energy of incident He^+ ions on target.
[b] Helium beam power deposited on target.
[c] Reduction in ^{22}Ne concentration as measured by the maximum yield before and after α-particle bombardment.

It should be noted that resistive evaporation is not the only method of fabricating a porous crystalline metallic structure, although it is convenient for metals with relatively low melting points. Electron beam evaporation or chemically induced crystal growth methods, such as de-alloying of NiM thin films [Sun et al., 2004, Wang and Balk, 2014] allow for greater control over deposition rate and crystal growth, and would produce targets with a higher thermal conductivity.

4.5.4 Atomic Force Microscopy

The porous titanium target showed the highest blister resistance, and, in addition, the lowest heat damage, of all targets investigated in this work. The porous targets were imaged to confirm the presence of surface structures which would also imply the presence of subsurface porosity.

Surface morphology of evaporated metal films is highly dependent on evaporation rate, with slower deposition rates typically resulting in films with a smaller grain size and decreased surface roughness [Cai et al., 2005]. This can be attributed to a number of factors, including the evaporation rate-dependence of trace gas inclusion within the film (particularly oxygen) during vacuum vapor deposition, and the adatom (an atom

on the surface of a crystal) diffusion rate relative to the evaporation rate [Cai et al., 2005, Hofmann et al., 2003]. Assuming Stranski-Krastanov (also known as "layer-plus-island") type growth [Stranski and Krastanow, 1937], it is reasonable to assume that the subsurface porosity is correlated with the surface grain size.

To confirm the presence of Stranski-Krastanov structures, topographical data were collected with atomic force microscopy (AFM, MFP-3D Asylum Research, Santa Barbara, CA) in ambient laboratory conditions using oscillatory mode (AC, or tapping mode) imaging with silicon Olympus AC160 cantilevers, using a nominal resonance frequency ≈ 300 kHz, spring constant of ≈ 26 Nm^{-1}, and tip radius of ≈ 10 nm. In typical imaging, the free oscillation amplitude was ≈ 100 nm and imaging was performed between 70 nm and 80 nm (70-80% of the free oscillation amplitude). Images were taken at a fast scan axis frequency of 1 Hz. Just prior to collection of the data presented here, a calibration standard was imaged to verify accuracy of the data along the x, y, and z axes. The topographical data are accurate to <2%.

The AFM employed in this study used an optical lever method for monitoring calibrated cantilever motion (resolution < 1 nm) on a quadrant photo diode (QPD) sensor. The cantilever is driven just below resonance (at 95% of peak amplitude) and the sharp tip at the end of the cantilever is brought into intermittent contact with the surface, while the QPD monitors cantilever motion. A proportional-integral-derivative feedback loop controls a piezo translation stage that maintains an operator selected damping of the amplitude of the cantilever motion. As the sample is scanned beneath the tip, the feedback loop maintains a set point cantilever amplitude by modulating the height of the cantilever mount position with a calibrated (< 0.1 nm) piezo translation stage. The feedback driven movement of this piezo is what is collected as the topographical height data, and is combined with the (x, y) position of the sample to build a map of the sample surface topography.

Figure 4.19 shows the images obtained by the atomic force microscopy measurements

on four different samples. Panel (a) shows a blank titanium backing, revealing surface features typical of machine-cut stock sheet metal. Panel (b) depicts a layer of evaporated titanium. It appears to be composed of multiple interlocking titanium crystals, with an average size of ≈ 300 nm. Therefore, the image confirms the presence of a porous titanium layer. Panel (c) represents a porous titanium layer that was implanted with ^{22}Ne ions. Panel (d) shows an image after the target was bombardment with 0.5 C of α particles. It can be seen that the ^{22}Ne implantation appears to have sputtered away the surface layer, and the α-particle bombardment further modified the surface of the implanted region.

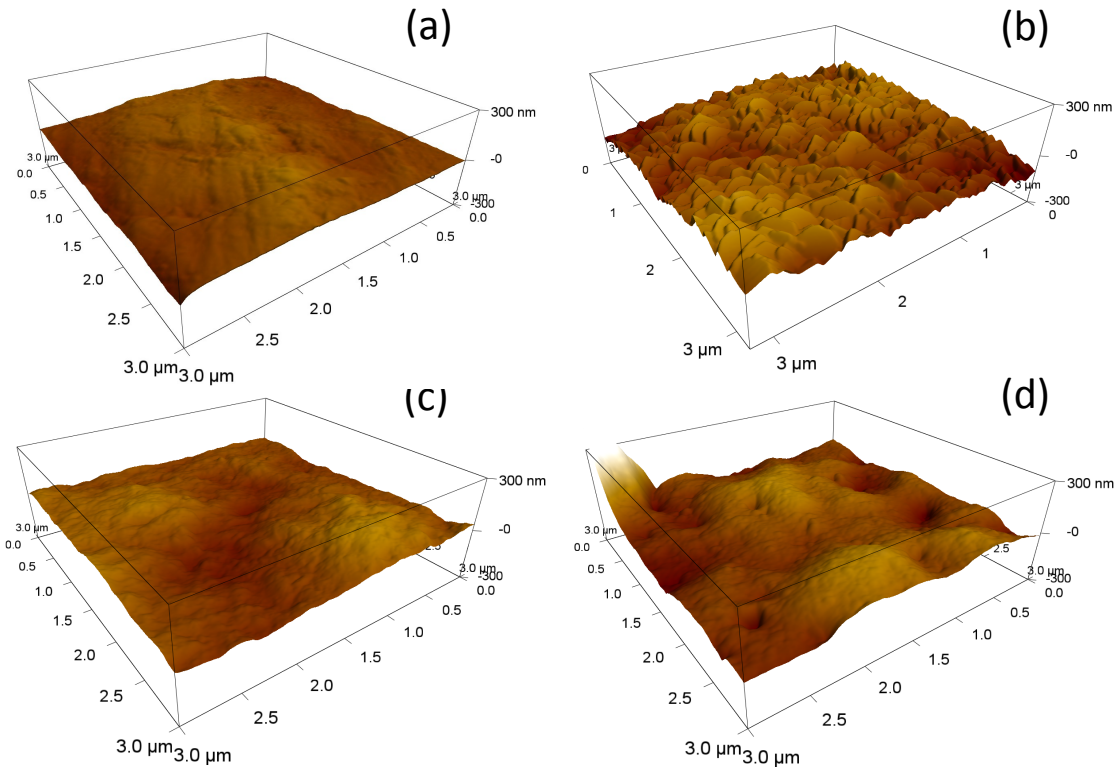

Figure 4.19: Atomic Force Microscopy (AFM) images. (a) Blank titanium backing; (b) Evaporated titanium layer. Note the interlocking crystalline structure, indicating a porous material; (c) Evaporated titanium layer after implantation with ^{22}Ne ions. The surface layer has been sputtered away; (d) Evaporated layer that has been implanted with ^{22}Ne and then exposed to a 30 μA α-particle beam of 900 keV energy for a total accumulated charge of 0.5 C.

4.6 Target for ^{22}Ne(α,γ)^{26}Mg Measurement

After it was determined that the porous titanium targets were blister-resistant, and withstood the greatest amount of heat damage, fabrication of targets for the measurement detail in Chapter 6 began. Unfortunately, only two targets could be implanted before technical issues ended the use of the ECR as an implanter. One of these two targets was destroyed by a faulty rastering system when using the high intensity α-particle beam with the JN, leaving only one target for use in the measurement of the 831 keV resonance in ^{22}Ne(α,γ)^{26}Mg. This will be discussed further in Chapter 6. The one porous titanium target used eventually saw a total of 4.4C accumulated charge using α-particle beam without showing any signs of blistering. The limit (or lack thereof) to the amount of α-particle bombardment the porous titanium targets can accumulate before blistering is not yet determined, but is at least 44 times greater than the accumulated charge needed to cause blistering in standard tantalum targets.

Chapter 5

Detectors

The ^{22}Ne(α,γ)^{26}Mg and ^{22}Ne(α,n)^{25}Mg experiments described in this dissertation produce different types of radiation and require two different types of detectors. LENA's High Purity Germanium Detector (HPGe) and sodium iodide (NaI) annulus were used to measure γ-rays from the ^{22}Ne(α,γ)^{26}Mg reaction, and are described in Section 5.1. The ^{22}Ne(α,n)^{25}Mg reaction was not measured in this research, but efforts were made to develop a detector system capable of measuring the neutrons from this reaction for a future experiment, and are detailed in Sections 5.4 and 5.5.

5.1 γ-ray Detector System

LENA's HPGe detector array consists of one 135% coaxial high purity germanium detector, sixteen thallium activated sodium iodide (NaI(Tl)) scintillators, five plastic scintillator paddles, and 10 mm thick lead shielding [Longland et al., 2006]. The HPGe detector is orientated at 0° with respect to the beam direction, and is placed flush with the end cap of the target chamber. The sixteen NaI(Tl) detectors are distributed in two annular eight-detector halves encircling the target chamber and HPGe detector. An aluminum frame surrounds the detector array and supports the 10 mm thick lead shielding to passively reduce the environmental background radiation. The five scintillator paddles, each 50 mm thick, are mounted on the lead walls to actively veto muons created by cosmic-ray interactions through a software anticoincidence condition.

Dimensions for the LENA HPGe detector were measured using a computed tomography (CT) scanner, and the dimensions for the annulus were provided by the manufacturer. Table 5.1 shows the dimensions, taken from Refs. [Carson et al., 2010] and [Howard et al., 2013].

HPGe parameters	Dimensions (mm)
End cap outer diameter	107.95 ± 0.02
Distance end cap-crystal	6.2 ± 0.5
Crystal length	91.6 ± 1.0
Crystal diameter	89.0 ± 0.5
Bulletizing radius	7.1 ± 0.5
Central hole diameter	8.5 ± 1.0
Central hole length	79.1
Central hole bottom radius	4.7
Vertical crystal displacement	-1.5 ± 0.5
Contact pin diameter	6.9 ± 0.5
Contact layer thickness	1.2
NaI(Tl) annulus parameters	**Dimension**
Inner radius	118.0 ± 0.5 mm
Outer radius	357.0 ± 0.5 mm
Crystal length	330.0 ± 0.5 mm
Segment spanning angle	$43.0 \pm 0.5^{\circ}$

Table 5.1: Dimensions of the HPGe detector and NaI(Tl) annulus. The HPGe dimensions were taken from [Carson et al., 2010] and the NaI(Tl) dimensions were taken from [Howard et al., 2013]

The detector array, pictured in Figure 5.1, uses a sophisticated $\gamma\gamma$-coincidence system to reduce background [Rowland et al., 2002]. The energy resolution of the HPGe detector is shown in Figure 5.4 and the energy resolution of the NaI(Tl) is $\approx$ 85 keV at 1.27 MeV γ-ray energy. Though the energy resolution of the HPGe detector is superior to the NaI(Tl) detectors, it has worse absolute efficiency, so the HPGe is used to measure γ-rays of interest, and the NaI(Tl) detectors are used as coincidence counters. Events within an adjustable software gate were recorded in a coincidence spectrum if events triggering the annulus detectors coincided in time and energy with events triggering the HPGe detector. Gates on the timing between HPGe and NaI(Tl) events and the energy of the events can be

chosen such that a γ-cascade produced by a beam-induced nuclear reaction is selectively preferred to events from environmental background.

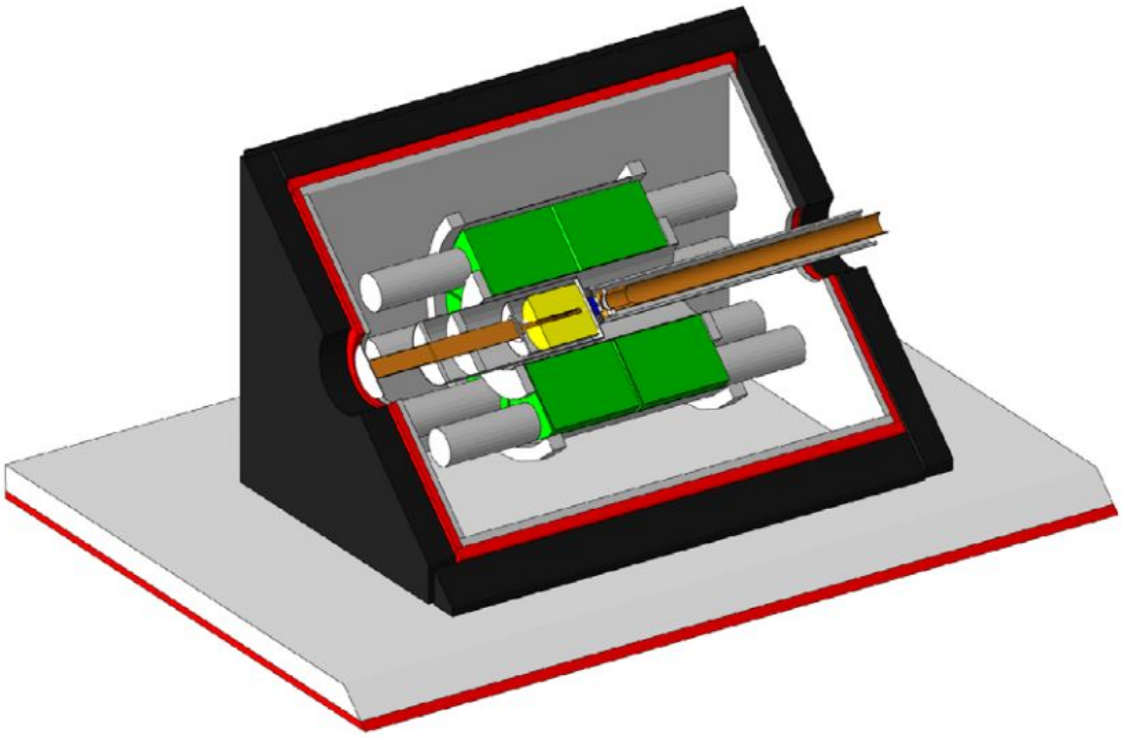

Figure 5.1: Cross sectional image of the LENA detector array, taken from [Howard et al., 2013]. The HPGe is shown in yellow, the NaI(Tl) is shown in green, the lead shielding is shown in red, and the plastic scintillator is shown in black. The beam travels down the beampipe on the left side of the image, and interacts with the target, producing a γ-ray cascade to be detected by the HPGe and NaI(Tl).

5.2 Coincidence Electronics

There are a total of 22 timing and energy signals that must be processed for the $\gamma\gamma$-coincidence system (the HPGe detector, 16 NaI(Tl) detectors, and 5 plastic scintillator paddles). The signals are processed using a mixture of Versa Module Eurocard bus (VME-bus) modules and Nuclear Instrument Modules (NIM). First, a signal from the HPGe detector is boosted with an on-board preamplifier, and the amplified signal is sent into a

spectroscopy amplifier to obtain energy information, and a timing filter amplifier (TFA) for timing information. The signal from the spectroscopy amplifier is set directly into an analog-to-digital converter (ADC). The TFA signal is sent into a constant fraction discriminator (CFD), which produces a logic signal that triggers a gate-delay generator downstream. This produces the master timing gate used to start a time-to-digital converter (TDC). A pulser is used to inject a signal into the HPGe's preamplifer to monitor deadtime.

Signals from the NaI(Tl) annulus are also sent into a spectroscopy amplifier and a fast filter amplifier (FFA). The signal from the spectroscopy amplifier is sent to the ADC and provides the energy of the NaI(Tl) events. The signal from the FFA is sent into a CFD, a 500 ns delay, and finally the TDC. The master timing gate caused by the HPGe detector starts the TDC, and the delayed timing signal from the annulus stops the TDC (the 500 ns delay is used because of the different response times between the HPGe detector and the NaI(Tl) detectors). Signals from the scintillator paddles are sent into a spectroscopy amplifier and TFA. The energy signal from the spectroscopy amplifier is sent into the ADC, and the timing signals from the TFA are sent into a leading-edge discriminator (LED). An anticoincidence condition between the scintillator paddles and the HPGe detector is set up using another TAC such that the HPGe signal is the start signal and the scintillator paddles is a stop signal, preventing data from being collected during cosmic ray induced muon events if the appropriate software gate is set. Figure 5.2 shows a detailed electronic schematic for the LENA detector coincidence system.

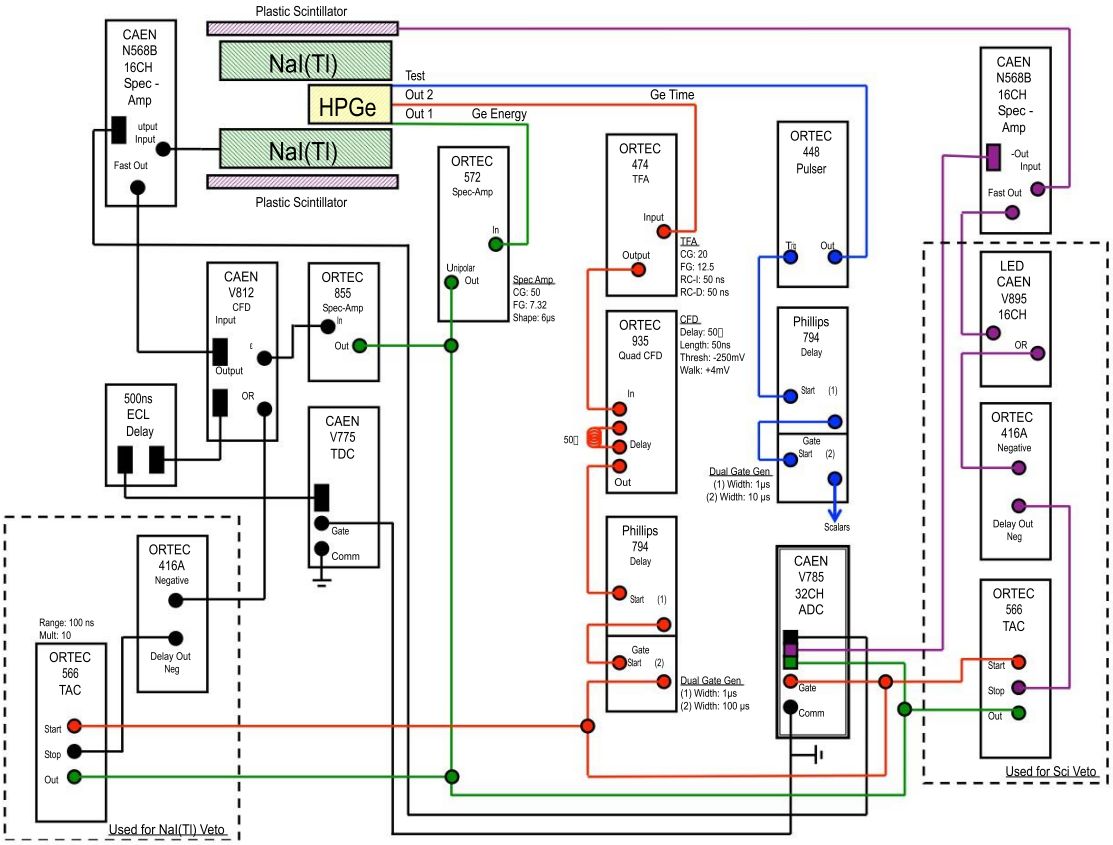

Figure 5.2: Schematic for the $\gamma\gamma$-coincidence detector setup at LENA. Image is taken from [Buckner, 2014]. See text for details.

A data acquisition system named `JAM` (a java-based system for nuclear physics) [Swartz et al., 2001] was used to process signals from the detector electronics and store data in an event-by-event structure. Logic determining the conditions for coincidence and anticoincidence are set in `JAM` using a `Java` sorting routing.

5.3 HPGe Efficiency and Resolution

Accurate nuclear measurements require the detector efficiency to be precisely understood. The measurement of the ^{22}Ne(α,γ)^{26}Mg relied heavily on the coincidence efficiency described in Section 6.5, but the majority of the measurements made in Chapter 4 did not require coincidence, and used only the HPGe portion of the γ-ray detector system. The efficiency and energy resolution of the detector system at LENA was measured precisely during the work detailed in [Kelly, 2016], and efficiency and energy resolution values from there were adopted with permission for this dissertation. The efficiency of the HPGe detector is shown in Figure 5.3.

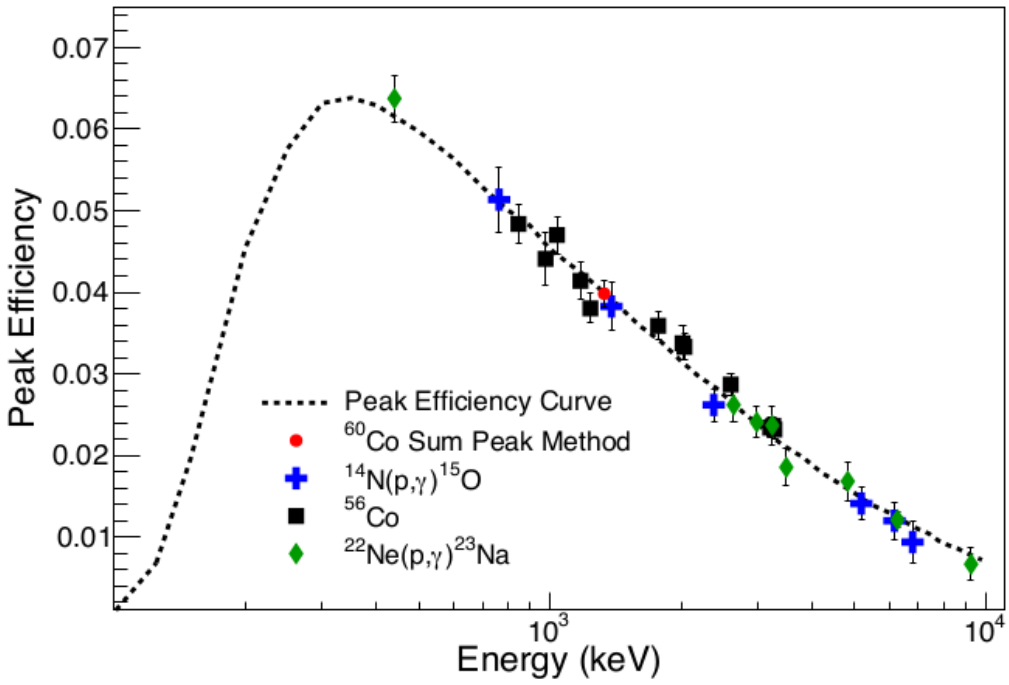

Figure 5.3: Peak efficiency plot for the HPGe detector. The dotted line is the normalized simulated efficiency, and the data points are measured data from ^{60}Co and ^{56}Co sources and the ^{14}N(p,γ)^{15}O and ^{22}Ne(p,γ)^{23}Na reactions. This plot and the efficiency values used for the measurements in Chapter 4 are courtesy of Keegan Kelly [Kelly, 2016]

.

The energy resolution (FWHM of detected γ-ray peaks) of the HPGe detector has been measured before using the 259 keV resonance in the ^{14}N(p,γ)^{15}O reaction, and is plotted

in Figure 5.4.

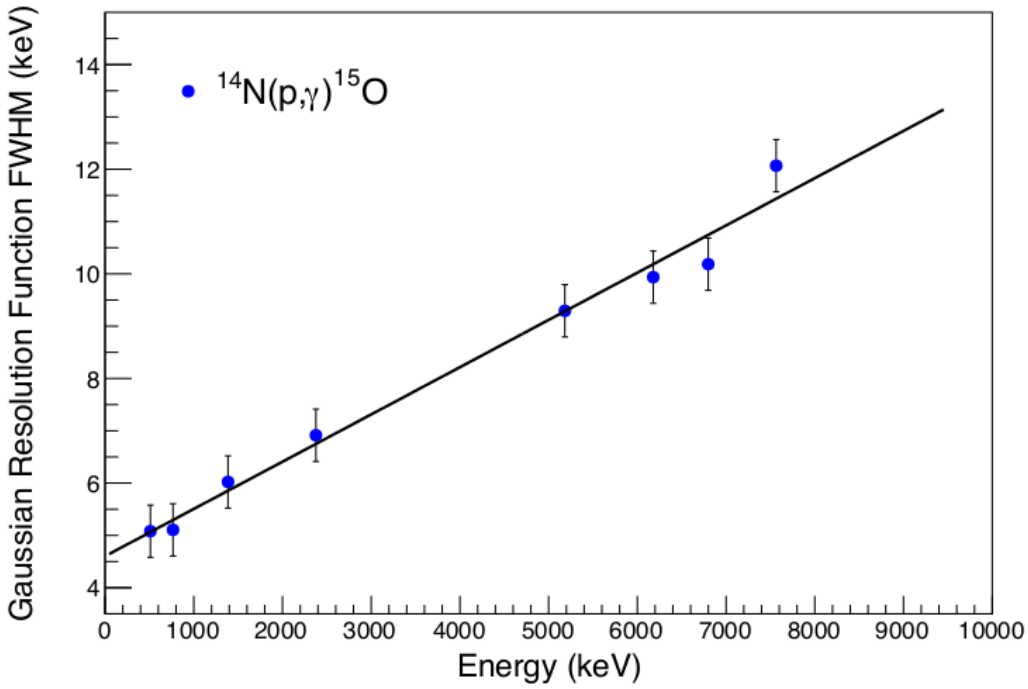

Figure 5.4: A trend of experimental peak Gaussian FWHM versus energy for the HPGe detector at LENA. Data points were obtained from the 259 keV resonance in ^{14}N(p,γ)^{15}O reaction. Image is courtesy of Keegan Kelly [Kelly, 2016]

.

The table shown for efficiency of the HPGe detector is without coincidence gating. The measurement of the resonance strength in Chapter. 6 used the full coincidence anti-coincidence setup described in Sections 5.1 and 5.2. The efficiency of the full coincidence setup is dependent upon the structure of the decay chain of the reaction of interest, which was simulated with `Geant4` and was analyzed using *Fraction Fitting*. These topics are discussed in depth in Chapter 6, and the details of the coincidence efficiency for the ^{22}Ne(α,γ)^{26}Mg measurement will be explained in that section.

5.4 BC-523A Detector

Previous direct measurements of the ^{22}Ne(α,n)^{25}Mg reaction saw significant contamination by high energy ($\approx$ 3MeV) neutrons produced by the ^{13}C(α,n)^{16}O reaction [Giesen

et al., 1993]. In an attempt to eliminate this beam-induced background contaminate, the viability of a boron-loaded capture-gated scintillator with fast neutron energy resolution, as shown in Figure 5.5, was explored. The work from this section has been published in [Hunt et al., 2016].

Figure 5.5: BC-523A boron-doped liquid scintillator. Blue tape was used to electrically insulate segments, and aluminum foil was used to electrically ground segments.

While standard liquid scintillators have long been used as fast neutron detectors [Post, 1950] because of their pulse shape discrimination (PSD) and timing abilities, they rarely provide reliable neutron energies [Bird and Burch, 1958]. This is primarily because of their nonlinear light output and their inability to differentiate between fully and partially moderated neutrons. A technique known as capture-gating, which uses standard organic liquid scintillator fluid and dopes it with high thermal neutron absorption cross section materials, such as ^{10}B, ^{6}Li, or ^{nat}Gd [Frehaut, 1976, Greenwood and Chellew, 1979, Greenwood et al., 1979] can allow for the differentiation between fully and partially moderated neutrons.

When a fast neutron strikes the capture-gated scintillator, the neutron will lose energy, producing a standard scintillation signal. If the neutron fully thermalizes and deposits

all of its energy into the detector, it has a chance to then capture onto the doping agent (in the case of the BC-523A detector, that doping agent is ^{10}B). The reaction products (α + ^{7}Li in the case of ^{10}B doping) will lose their energy in the active volume, producing a secondary scintillation pulse. This series of interactions produces a characteristic double-peaked signal when a neutron fully moderates in the detector. If only the characteristic double pulse signal is counted, all neutrons detected will be full energy deposition events, allowing the capture-gated scintillator to be used as full-energy neutron spectrometers [Post, 1950].

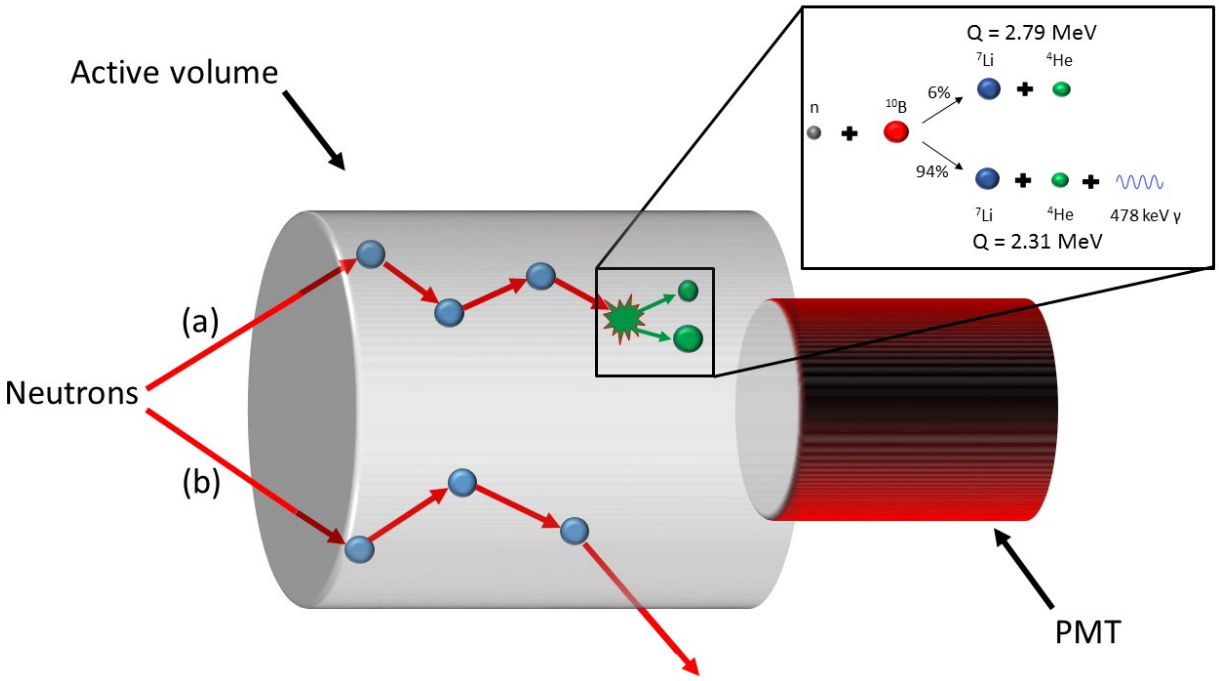

Figure 5.6: Illustration of neutron-induced events in a ^{10}B-doped liquid scintillator. (a) Full energy deposition and subsequent capture of a fast neutron, giving rise to the characteristic double pulse signal, illustrated in Figure 5.7a. (b) Partial energy deposition of fast neutron energy, giving rise to a single pulse signal, illustrated in Figure 5.7b.

Boron-doped scintillators have had extensive research performed on them [Jastaniah and Sellin, 2004, Pawełczak et al., 2011, Swiderski et al., 2008, Szczesniak et al., 2010, Williams et al., 2004], and the physics behind the scattering and capture interactions are well understood [Jastaniah and Sellin, 2004]. Figure 5.6 shows the sequence of events

when an incident neutron (shown in red) strikes the detector. The neutron first interacts with the hydrogen (shown as blue circles) in the scintillator fluid, causing those protons to recoil and produce a peak in the waveform of the signal. If the neutron loses most of its energy, it has a high likelihood of capturing onto the dopant via ^{10}B(n,α)^{7}Li because of the large thermal neutron cross section of ^{10}B. This interaction is fairly long-lived by scintillator standards, and takes place on average about 500 ns after the neutron moderates [Jastaniah and Sellin, 2004]. The energy released (Q-value) in the reaction is 2.31 MeV (94% probability) when the ^{7}Li is left in the first excited state, giving rise to the additional emission of a 478-keV photon, or 2.79 MeV (6% probability) when the ^{7}Li is left in the ground state (breakup products are shown in green). Moderation of the breakup products (mainly of the α-particle) in the scintillator fluid causes a second peak (capture peak) in the waveform of the signal. This process is illustrated as (a) in Figure 5.6, and in Figure 5.7a.

If an incident neutron interacts with the hydrogen in the scintillator fluid, but scatters out of the detector without capturing onto ^{10}B, only a single moderation peak is produced. This process is illustrated as (b) in Figure 5.6, and in Figure 5.7b. In practice, the signals can be more complicated, as noise on the tail of a moderation peak (see Figure 5.7c) may mimic a double-peak waveform and be mistaken for a capture event. If the double-peak signature of full neutron energy deposition can be differentiated from both a partial energy deposition event and from noise, the incident energy of the fast neutron can be estimated from the pulse height of the first (moderation) peak in the waveform.

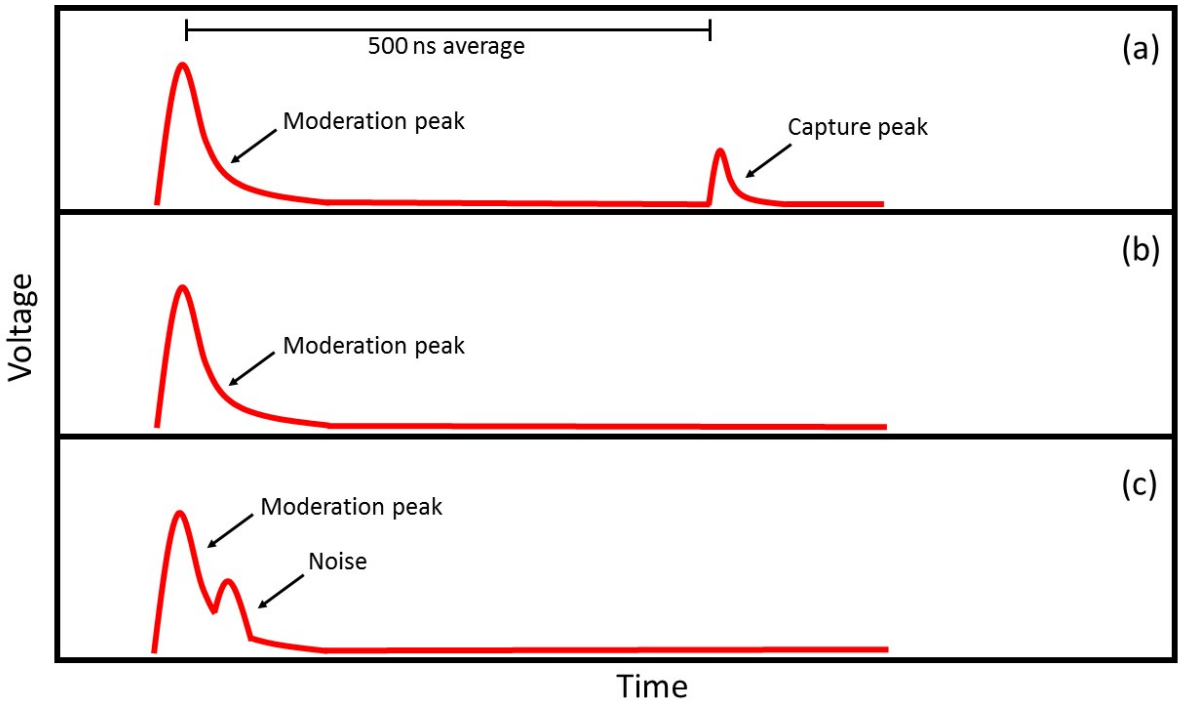

Figure 5.7: Illustrative waveforms of a ^{10}B-doped liquid scintillator. (a) From full energy deposition of an incident fast neutron. The first peak is caused by the recoil of protons in the scintillator fluid from the fast neutron, and the pulse height of this peak carries the information about the incident energy, while the second peak is caused by the moderated neutron undergoing a ^{10}B(n,α)^{7}Li reaction. The moderation pulse and capture pulse have an average time difference of 500 ns. (b) From an incident γ-ray or partial energy deposition of an incident fast neutron, with no ^{10}B(n,α)^{7}Li reaction occurring. Pulse height is not as indicative of incident particle energy because of the unknown fraction of energy deposited. (c) From noise on the tail. This signal can be mistaken for a double-peaked event if timing, pulse shape discrimination, and pulse height are not taken into consideration (see text for details).

5.4.1 Experimental Setup

The BC-523A detector has a scintillator cell with a diameter of 8.89 cm, and a length of 10.76 cm. The detector was manufactured by Saint-Gobain Crystals, and was fitted with a Hamamatsu R1307 head-on photomultiplier tube. Data were collected with a 12-bit 250 MHz (4 ns sampling step) digitizer collecting waveforms containing 520 samples each for a total digitization time of 1.04 μs for each waveform.

To use the BC-523A detector, the capture event needs to be properly identified and

reliably gated, the efficiency needs to be measured, and the energy resolution must be determined. To achieve this, two experiments with the BC-523A detector were conducted.

The first experiment used a 19.7 μCi Americium-Beryllium (AmBe) source placed $\approx$ 0.3 m from the detector. Approximately 1×10^6 events were recorded using a threshold on the internal constant fraction discriminator (CFD) set slightly above the noise level. These data were used to determine the pulse-shape discrimination capabilities of the detector, and to identify and gate on the capture signal. No radiation shielding was used in this experiment.

The second experiment was used to investigate the detector's intrinsic neutron detection efficiency and energy resolution for fast incident monoenergetic neutrons using the time-of-flight method. A weak (0.185 μCi), but well calibrated, ^{252}Cf source inside an argon gas scintillator was placed 1 m away from the BC-523A detector. The experimental area was a small room located in the back of LENA. Because of the small size of the room and the possibility for neutrons scattering off the walls and ceiling giving a false time of flight, the detector and source were both placed on small platforms elevated $\approx$ 1.5 m from the floor, and centered equidistant from the walls of the room.

When a ^{252}Cf fission event occurred, it created a signal in the argon gas scintillator that was used to trigger a constant fraction discriminator (CFD), which started a time-to-amplitude converter (TAC). A neutron from that ^{252}Cf fission event striking the BC-523A detector produced a pulse that triggered a CFD which acted as a stop signal for the TAC. This setup is illustrated in Figure 5.8. The nearly instantaneous travel-time of γ-rays produced from ^{252}Cf α decay was used to calibrate the TAC. The time-of-flight method was then used to measure the energy of each detected neutron. The 250 MHz digitizer was used to collect waveforms with 520 samples. During the run, $\approx 3 \times 10^5$ neutrons were detected.

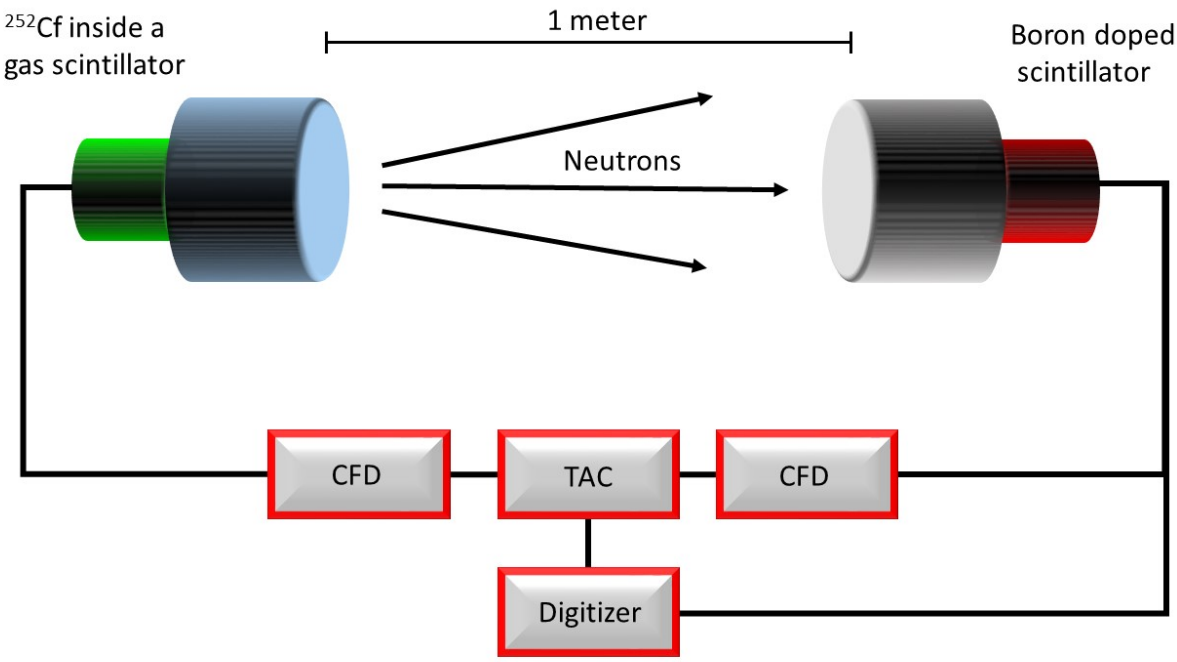

Figure 5.8: Illustration of the experimental setup for the second experiment. A ^{252}Cf neutron source inside a scintillator provided the start signal for the time-to-amplitude converter (TAC) through the constant fraction discriminator (CFD). The signal from the BC-523A detector was split, with one signal used to stop the TAC, and the other one sent to the digitizer. Waveforms of $\approx 3 \times 10^5$ events were recorded with the digitizer.

5.4.2 PSD and the Capture Event

Organic liquid scintillators typically display good pulse shape discrimination (PSD) of the moderation pulses for α-particles, neutrons, and γ-rays [Comrie et al., 2015]. However, in capture-gated scintillators, there is additional light quenching caused by the ^{10}B doping agent [Jastaniah and Sellin, 2004]. This light quenching inhibits the pulse shape discrimination at lower energies, making the capture event harder to distinguish from incident particles. Previous work on ^{10}B-doped capture-gated scintillators showed conflicting results for pulse shape discrimination of the capture event [Flaska and Pozzi, 2009, Pino et al., 2014], so attempts were made to provide a detailed analysis of the capture peak and the often misinterpreted noise.

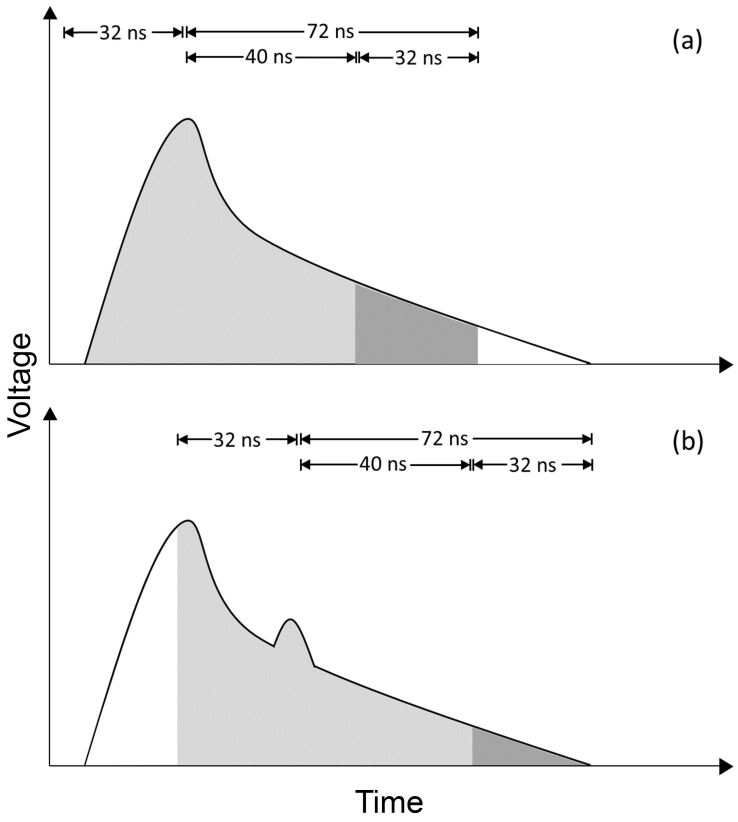

Figure 5.9: Illustration of the pulse shape discrimination (PSD) method used. (a) Typical scintillator (moderation) pulse. The total integrated charge, represented by the gray areas, is 104 ns in length and yields the total energy of a pulse. The tail integrated charge, represented by the dark gray area alone, is 32 ns in length and provides the PSD value used to differentiate between incident radiation types (neutrons, α-particles, γ-rays). (b) Example of PSD applied to a typical scintillator pulse with noise on the tail. If noise is not properly identified, it will be treated as a separate event, and yield erroneous values for energy and PSD.

The PSD method chosen for this study was the tail-to-total charge ratio [Flaska and Pozzi, 2007]. It has the advantage of good discriminatory properties between γ-rays and neutrons, because the charge integrated over the tail of a pulse differs for these two incident particles. This method was also used by the two groups with conflicting identification of the capture event [Flaska and Pozzi, 2009, Pino et al., 2014], making for convenient comparison. The tail integration started at 40 ns after the peak of a pulse, and ended 72 ns after the peak, as depicted by the dark gray area in Figure 5.9a. The total integration

started 32 ns before the peak, ended 72 ns after the peak, and is represented in Figure 5.9a by the light and dark gray areas. This interval was chosen to maximize neutron and γ-ray discrimination at all energies. It should be noted that this method has poor noise performance, as illustrated in Figure 5.9b. That figure shows a noise peak following the main moderation peak. If PSD is performed on the noise peak, both the tail charge and the total charge will be affected by the preceding moderation pulse. As a result, such noise events can be easily misidentified as other events, including capture pulses.

Data taken with the AmBe source in the first experiment described in Section 5.4.1 were analyzed in an attempt to identify the capture peak using pulse shape discrimination. Pulse shape discrimination was performed on each peak that triggered the internal constant fraction discriminator of the digitizer described in Section 5.4.1. The results are shown in Figure 5.10a, which display the signal tail integral versus the total integral (see Figure 5.9a) of every peak detected be the scintillator. The figure shows good discrimination between fast neutrons and γ-rays at all but the lowest energies, and also shows a separate structure, which will be referred to here as the *third branch*. Figure 5.10b shows only those events obtained when a moderation pulse (the first peak in Figure 5.7a) triggered the digitizer, but with PSD only applied to a peak that arrived more than 150 ns after the triggering pulse (long after the moderation pulse has decayed). The structures seen in Figure 5.10b do not match the third branch identified in Figure 5.10a. In Figure 5.10b, there can be seen an oval shaped region in the lower left, and a branch off the oval region. The events in these two regions will be collectively referred to as the *afterpulse region* events.

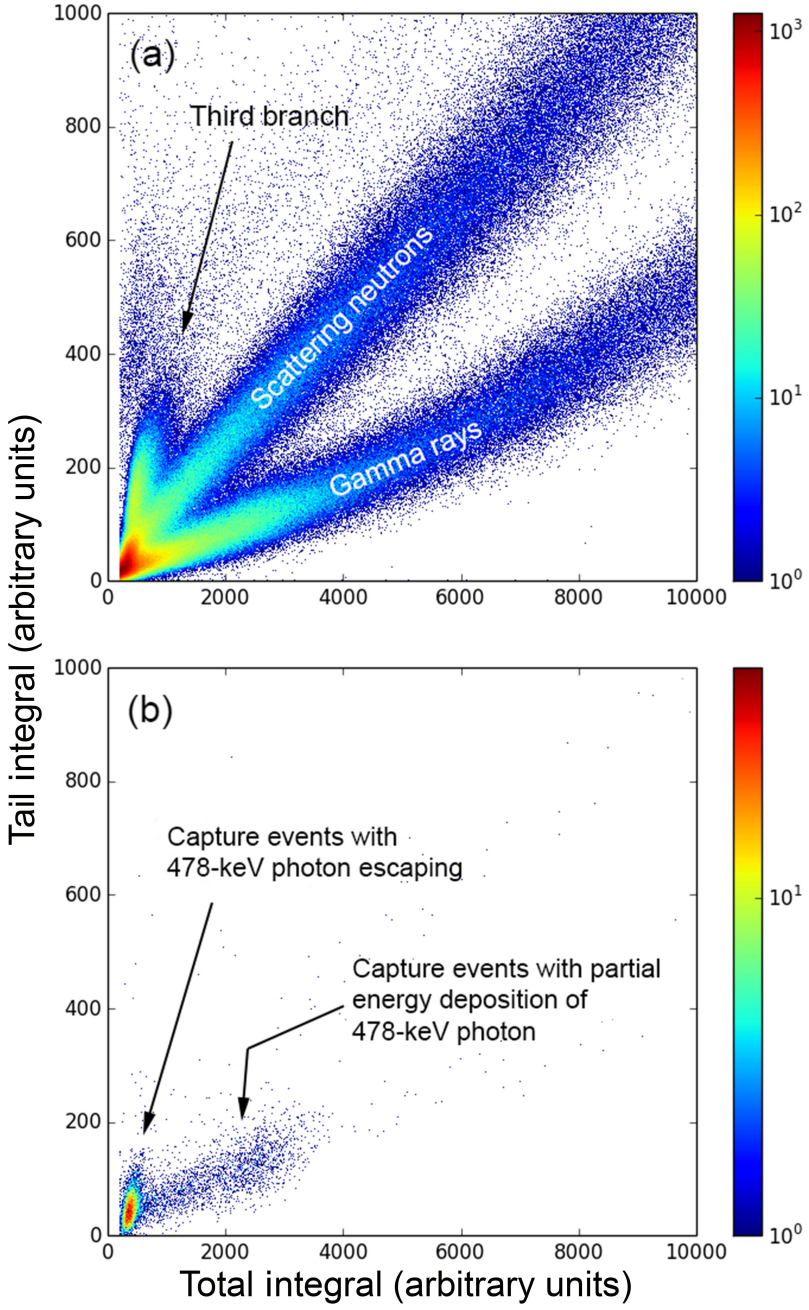

Figure 5.10: Pulse shape discrimination (PSD) histograms of tail integrated charge over total integrated charge (see Figure 5.9a) of each peak detected, obtained using an AmBe neutron source. (a) For all pulses triggering the digitizer; regions occupied by neutrons and γ-rays are labeled. The third branch has been identified as the capture peak in Ref. [Flaska and Pozzi, 2009]. (b) For events obtained when the moderation pulse triggered the digitizer, but with PSD only applied to the part of the signal arriving 150 ns after the triggering pulse. The oval shaped region is occupied by capture pulses with no energy deposition of the 478-keV photon produced in the ^{10}B(n,α)^{7}Li reaction (see Figure 5.6). The branch off the oval shaped region is caused by capture pulses with partial energy deposition by the 478-keV photon.

Conflicting results have been reported in the literature in connection with PSD for the capture pulse. Some research groups have identified the third branch in Figure 5.10a as the capture peak [Flaska and Pozzi, 2009, Peerani et al., 2012], while other groups have identified the afterpulse region in Figure 5.10b as the capture peak [Pino et al., 2014]. Two separate tests were performed on these regions to identify the capture events: a timing and a gating test.

5.4.3 Timing and Gating Tests

Neutron capture onto ^{10}B in the BC-523A detector has been well modeled [Jastaniah and Sellin, 2004], with the probability of a neutron capture as a function of time expressed as:

$$P(t) = \frac{1}{\tau} e^{-\frac{t}{\tau}} \tag{5.1}$$

where the parameter τ is the average capture lifetime, which depends only on the concentration of the doping agent (^{10}B) in the scintillator. Jastaniah also measured the average capture time after moderation to be $\approx$ 500 ns.

The time difference between a triggering event (usually a scattering neutron) and a pulse falling within the third branch of Figure 5.10a was measured to compare with the results of [Jastaniah and Sellin, 2004]. The histogram of the time difference between these two events is shown in Figure 5.11 and reveals a mean time difference of 136($\pm$10) ns, which disagrees with the value of $\approx$ 500 ns found by [Jastaniah and Sellin, 2004]. Therefore, it is unlikely that third branch events represent neutrons that are being captured after moderation.

It should be noted that the peak sensing algorithm is responsible for the sharp cutoff of the histogram around 130 ns. Altering the parameters of the algorithm can affect the mean capture by 10s of ns, which is insufficient to bring the average capture time of the

third branch events in line with the known value of ≈ 500 ns.

An identical timing test was performed on a triggering event and a pulse falling within the afterpulse region (the oval and branch shown in Figure 5.10b) and a histogram of the time difference between these two pulses is shown in Figure 5.11b. The average time difference is $501(\pm 30)$ ns, in agreement with the average capture time measured by [Jastaniah and Sellin, 2004] for the capture of neutrons after moderation. The timing tests indicate the third branch events previously thought to be the capture events are something else, and the afterpulse region contains the true capture event.

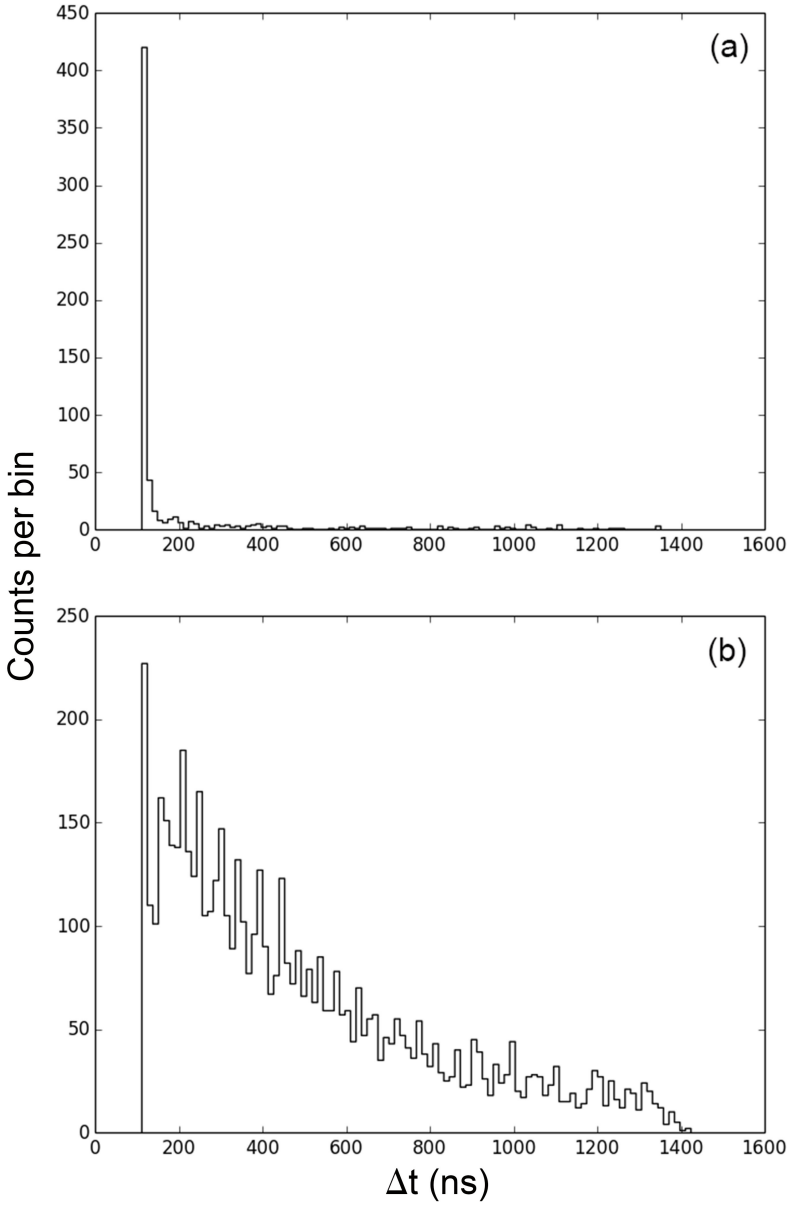

Figure 5.11: (a) Time difference between a pulse triggering the digitizer (usually caused by the moderation peak from a scattering neutron) and a later pulse that populates the third branch region in Figure 5.10a. The mean time difference is 136 ($\pm$10) ns, inconsistent with a predicted average value of 500 ns [Jastaniah and Sellin, 2004] for the time difference between a fast neutron moderation peak and the subsequent capture peak. (b) Time difference between a pulse triggering the digitizer and an event that populates the afterpulse region (the oval shaped region and the branch) in Figure 5.10b. The average capture time is 501 ($\pm$30) ns, consistent with the predicted value of 500 ns [Jastaniah and Sellin, 2004]. The data were obtained using the first experimental setup described in Section 5.4.1.

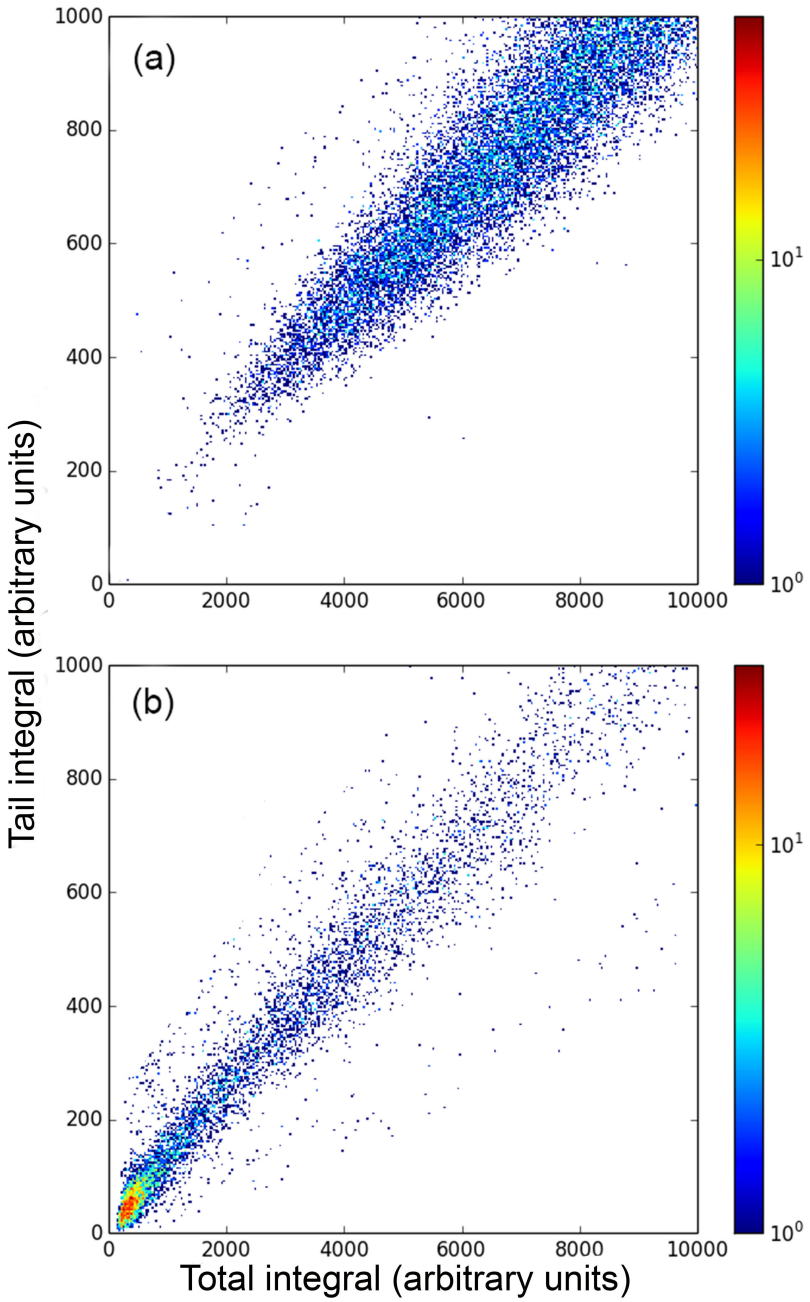

Figure 5.12: PSD histograms of tail integrated charge over total integrated charge (see Figure 5.9a), obtained using an AmBe neutron source. (a) Pulses that trigger the digitizer and are followed by a pulse falling into the third branch region of Figure 5.10a. The increasing number of events for increasing energy indicates that they are not associated with capture events (see text for details). (b) Pulses that trigger the digitizer and are followed by a pulse falling into the afterpulse region of Figure 5.10b. The increased number of events at decreasing energy indicates that they are associated with capture events. The majority of events in both of these plots fall within the scattering neutron region of Figure 5.10a.

To identify the origin of the third branch in Figure 5.10, the AmBe source described in the first experimental setup in Section 5.4.1 was used to analyze the triggering pulse for any waveform containing a third branch event in Figure 5.10a. Pulse shape discrimination was performed on only the triggering pulse and the results are shown in Figure 5.12a. The events have a large total integrated charge and a large tail integrated charge relative to the total charge. This indicates that the triggering pulses are primarily caused by high-energy incident neutrons. The increased number of events in Figure 5.12a with increasing energy also shows that there is a direct relationship between neutron energy and the likelihood to create a third branch event. Low-energy neutrons have a greater chance of thermalization and capture on ^{10}B than high-energy neutrons [Jastaniah and Sellin, 2004], indicating that the third branch events are caused by the neutrons least likely to produce a capture pulse. Furthermore, the neutron energy spectrum produced by an AmBe source favors the production of lower energy neutrons [Lebreton et al., 2007], indicating that the third branch events are very unlikely to be associated with capture events.

The triggering pulse for any waveform that has an event in the afterpulse region in Figure 5.10b was also analyzed. The PSD plot is displayed in Figure 5.12b, and shows that the majority of pulses have a small total integrated charge, but a large tail integrated charge relative to the total charge. These events are most likely caused by incident neutrons. The number of such events increases with decreasing energy, consistent with both the energy spectrum of the neutron source [Lebreton et al., 2007] and the higher chance for low-energy neutrons to moderate and capture on ^{10}B in the BC-523A scintillator [Jastaniah and Sellin, 2004].

The timing and gating tests show that the events in Figure 5.10b are caused by predominantly low-energy neutrons that produce a moderation peak and a subsequent capture peak, according to Figure 5.7a. When no 478-keV photon is produced in the ^{10}B(n,α)^{7}Li reaction, or if it is produced but leaves the detector without scattering (Figure 5.6), the event appears in the oval region in Figure 5.10b. If the 478-keV photon deposits part or

all of its energy in the detector, the events appear in the branch off the oval region. Gating on these events in Figure 5.10b will be referred to as *capture-gating*.

In contrast, the events located on the third branch in Figure 5.10a are most likely caused by high-energy neutrons that leave a fraction of their energy in the detector and that are accompanied by a noise peak on the tail of the preceding (moderation) peak, according to Figs. 5.7c and 5.9b. These results disagree with recent claims by other groups [Flaska and Pozzi, 2009, Peerani et al., 2012] that the third branch is caused by capture events. These conclusions are supported by [Pino et al., 2014], who showed that the third branch disappears when pile-up suppression software filters are turned on.

5.4.4 Energy Resolution Measurements

The measured energy resolution for the BC-523A detector using capture-gating is rarely reported in the literature. Data recorded with the ^{252}Cf neutron source (see Section 5.4.1) were analyzed to obtain the detector energy resolution for fast incident monoenergetic neutrons. If the capture peak is properly identified, the preceding moderation peak contains the information about the incident neutron energy. Recall that a moderation peak without a subsequent capture peak is most likely caused by a neutron that deposits only part of its energy in the detector. For this reason, neutron spectroscopy measurements, especially for higher incident neutron energies, are most meaningful after capture-gating is applied (i.e., gating on the oval and branch in Figure 5.10b; see Section 5.4.2), as it allows us to ignore partial energy deposition. The energy resolution is defined as:

$$R = \frac{FWHM}{\vartheta} \times 100\% \tag{5.2}$$

where FWHM and ϑ are the full width at half maximum and the centroid, respectively, in the pulse height spectrum for the moderation peak.

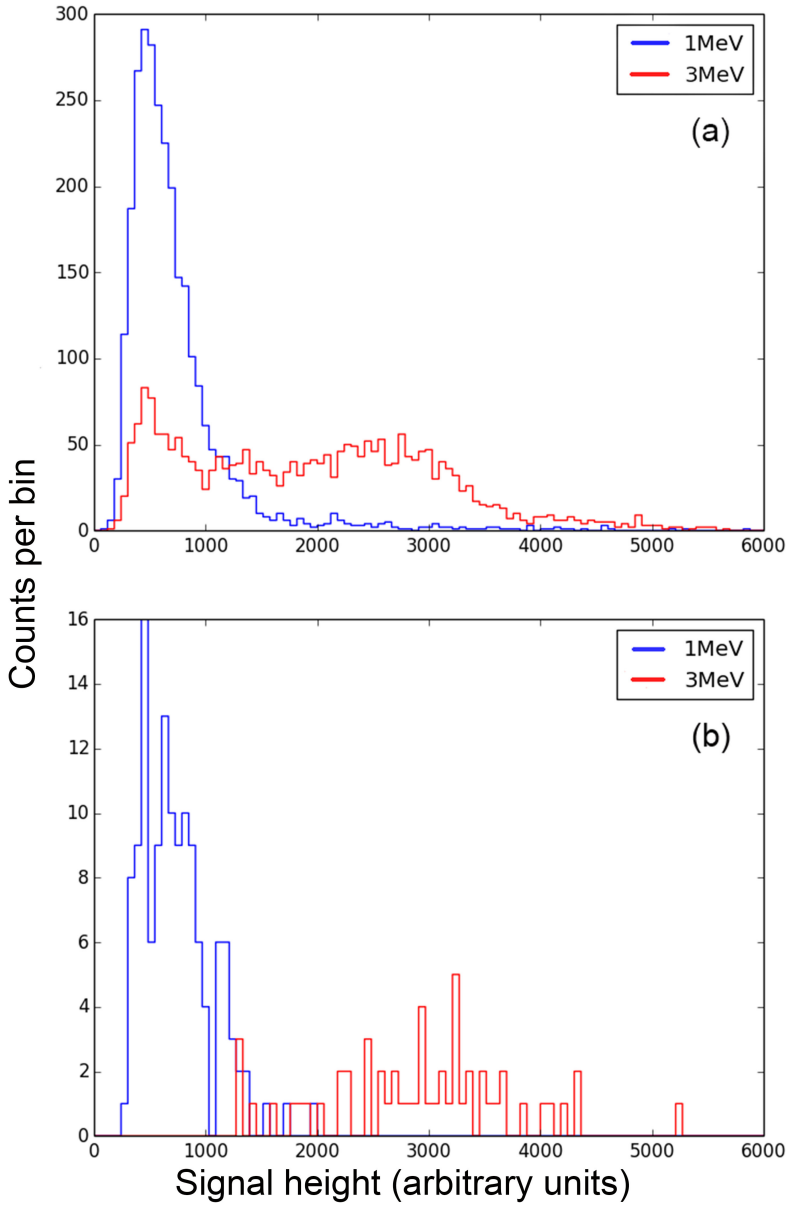

Figure 5.13: Measured pulse height spectra for 1 MeV and 3 MeV incident neutrons, obtained using a ^{252}Cf source inside a scintillator and the time-of-flight method. The low energy cutoff was set to slightly above zero (the use of the time-of-flight method prevents most noise events from being counted). (a) With no capture-gating applied (the triggering pulse for every waveform was recorded). The 1 MeV neutrons fill the histogram in a Gaussian shape, while the 3 MeV neutrons do not. It is not possible to fully discriminate between 1 MeV and 3 MeV incident neutrons. (b) With capture-gating applied (only a triggering pulse followed by a capture pulse was recorded). Only fully moderated neutrons are counted (full energy deposition), resulting in Gaussian distributions at each energy. Capture-gating decreases the number of neutrons detected significantly.

Figure 5.13a shows a pulse height histogram for 1 MeV (shown in blue) and 3 MeV (shown in red) incident mono-energetic neutrons before capture-gating was applied. The combination of capture-gating and the time-of-flight method guarantees that only neutrons were counted, and the energy for these neutrons was measured using the time-of-flight method (see Section 5.4.1). The low energy noise cutoff in pulse height is close to zero, so it does not significantly affect the distributions shown in Figure 5.13. Each chosen energy (1 MeV and 3 MeV) has an energy spread of $\pm 3\%$. The 1 MeV neutrons fill the histogram in a Gaussian shape, while the 3 MeV neutrons are much more spread out, and less Gaussian. This is because 1 MeV neutrons are more likely to deposit most of their energy compared to the 3 MeV neutrons. Prior to applying the capture gate, significant overlap between the 1 MeV and 3MeV pulse height spectra is observed. This is caused by partial energy deposition from the 3 MeV neutrons filling lower pulse height bins. Figure 5.13b displays the same data set after capture-gating is applied (see also Figure 5.10b). After capture-gating, the pulse height spectra for the 1 MeV and 3 MeV incident neutrons both take on Gaussian shapes and can now be separated.

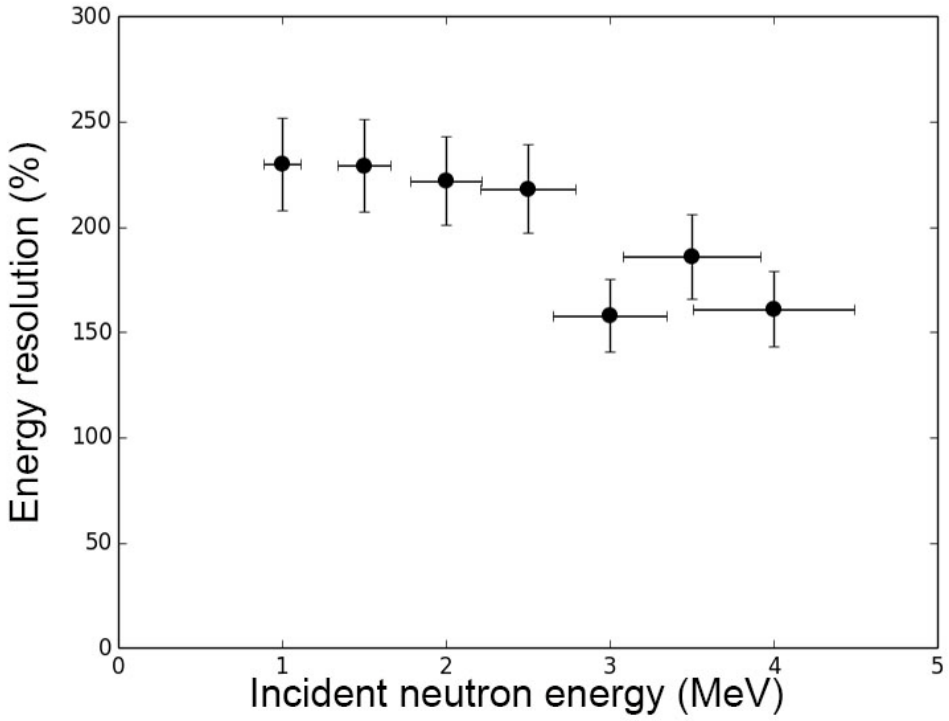

Figure 5.14: Energy resolution of the BC-523A detector as a function of incident neutron energy, measured by the time-of-flight method. Each point represents the energy resolution for all neutrons of a given energy interval (±3% of the total energy). The uncertainty in the x-axis accounts for the ±3% energy spread and systematic errors primarily caused by the low count rate from the source (see Section 5.4.1) and uncertainty in the TAC. The y-axis uncertainty is almost entirely caused by the low count rate of the source. The overall trend indicates a linear improvement in energy resolution as the incident neutron energy increases.

Figure 5.14 shows the detector energy resolution for fast incident monoenergetic neutrons as a function of neutron energy. Capture-gating is applied to these data, and the uncertainties are primarily determined by the low event rate of the neutron source.

5.4.5 Efficiency

Experimentally measured detector efficiency for the BC-523A detector is likewise rarely reported in the literature using capture-gating. The efficiency was measured in this study using a ^{252}Cf source (see Section 5.4.1). Efficiencies were determined at several neutron

energies, both with and without capture-gating. The time-of-flight method discussed in Section 5.4.4 was again utilized to measure the energy of each neutron striking the detector, and the intrinsic efficiency was calculated according to:

$$\epsilon = \frac{N_d}{N_i} \times 100\% \tag{5.3}$$

where N_d is the total number of neutrons detected, and N_i is the number of neutrons incident on the detector; N_i was calculated from the known intensity of the ^{252}Cf source, the known neutron energy distribution of the source [Miller, 2012], and the geometry of the setup.

Figure 5.15a shows the measured intrinsic efficiency, as defined in Equation 5.3, for fast incident neutrons with energies between 1 MeV and 4 MeV before capture-gating is applied (black data points). The intrinsic efficiency is approximately 30% and decreases slightly with increasing neutron energy, which is typical for a liquid scintillator of this size [Banerjee et al., 2009].

Figure 5.15b displays the measured intrinsic efficiency for fast neutrons with energies between 1 MeV and 4 MeV after capture-gating is applied (black data points). The resulting efficiency amounts to around 1%. The efficiency also decreases with increasing neutron energy, because lower energy neutrons have a greater chance to lose all their energy while moderating within the detector, thereby increasing the probability of a capture event.

Monte Carlo simulations were also performed using the `Geant4` toolkit [Agostinelli et al., 2003] to gain a better understanding of the capture-gated fast neutron detection efficiency at energies below the measured data points. The BC-523A detector was simulated by using a standard liquid scintillator that was loaded with 5% of ^{10}B by weight. A monoenergetic neutron beam was simulated incident on the detector, and energy deposition and particles created were recorded for a total of 1×10^6 incident neutrons per energy of interest. The neutron detection efficiency was extracted based on the number of

neutrons, resulting in energy deposition above a threshold level (set to 100 keV). Neutron capture is included in the simulations using the `G4NeutronHP` model, and a simulated capture event is identified by the simultaneous creation of ^{7}Li and an α-particle in the detector. Fast neutron detection efficiencies were then extracted according to Equation 5.3 from the simulations, both with and without capture-gating. All efficiency simulations were adjusted by a common scaling factor to account for the uncertain light collection in the scintillator, so that the simulations are matched closely to the measured values at the higher neutron energies.

Figure 5.15a compares the simulated and measured fast neutron detection efficiencies without capture-gating applied. The black points show the measured data, and the red points are the simulated values from `Geant4`. The measured and simulated efficiencies agree at higher energies. For neutrons with energies less that 1 MeV, the simulations predict intrinsic efficiencies of around 35%. Figure 5.15b shows the neutron detection efficiencies with capture-gating applied. Again, the simulated and measured efficiencies agree at higher neutron energies. For neutrons with energies near 250 keV (the lowest energy simulated), the predicted intrinsic efficiency is $\approx 3\%$.

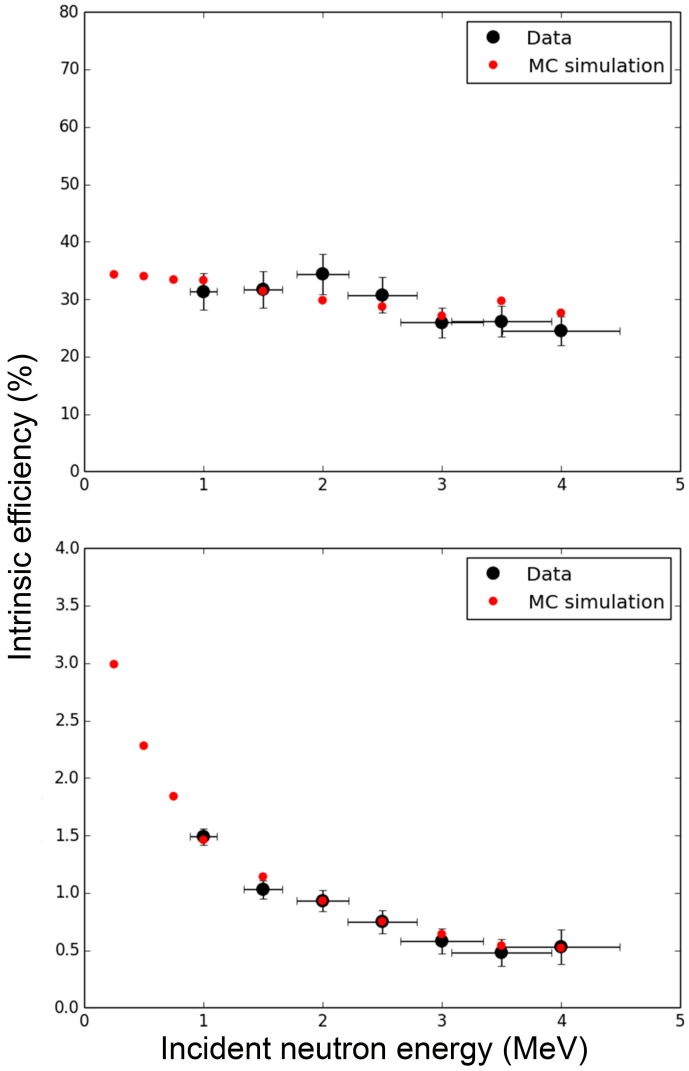

Figure 5.15: Simulated (red; using `Geant4`) and measured (black; using the time-of-flight method) intrinsic neutron detection efficiencies of the BC-523A detector versus incident neutron energy. (top) No capture-gating applied. (bottom) With capture-gating applied.

Though the BC-523A detector was shown to have sufficient energy resolution to eliminate the carbon contaminant background, it was ultimately decided that the efficiency was too low for the ^{22}Ne(α,n)^{25}Mg measurement. Another detector was chosen with a higher efficiency, while still retaining some amount of energy veto to account for fast neutrons produced by the ^{13}C contaminant.

5.5 INVS Detector

The model IV inventory sample counter (INVS) (shown in Figure 5.16) is a detector array developed at Los Alamos National Laboratory, and was designed to allow for quick, non-destructive assay of radioactive material, but was adapted for in-beam measurements at TUNL. The INVS detector, shown in 5.16 and illustrated schematically in 5.17, is a multi-segmented ^{3}He proportional counter. The counters are placed in two concentric rings embedded in a polyethylene neutron moderator. Dimensions for the detector are taken from [Arnold et al., 2011], and are given in Table 5.2.

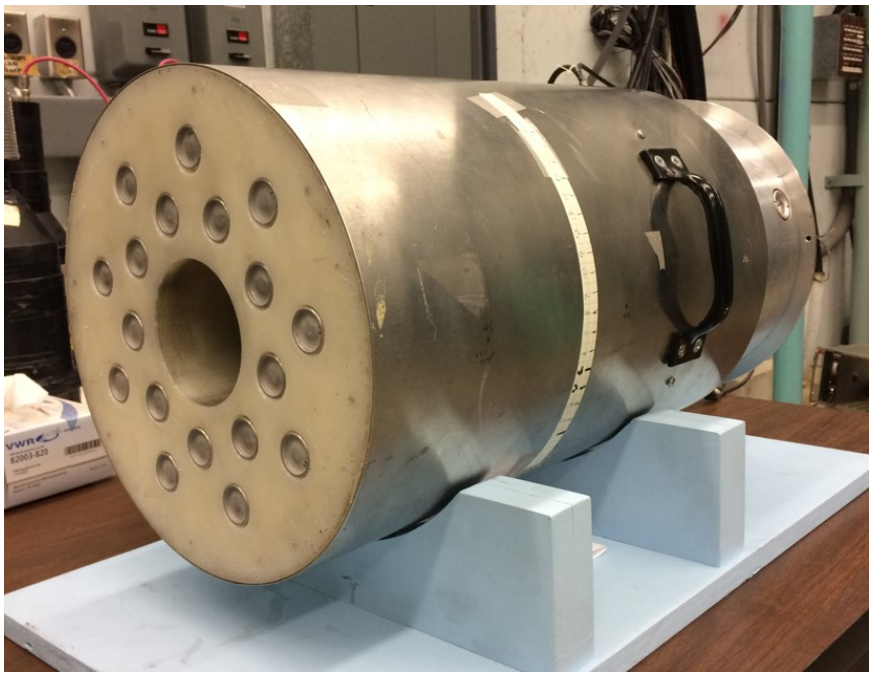

Figure 5.16: Photograph of the INVS detector. The ^{3}He cells and axial beamline cavity are clearly visible.

The detector encompassed the beamline and target chamber where the ^{22}Ne(α,n)^{25}Mg reaction can take place. Neutrons produced from the reaction thermalize in the polyethylene body of the detector, and can capture in the embedded proportional counters via the ^{3}He(n,p)^{3}H reaction. The 763.7 keV of energy released is shared between the outgoing triton and proton from this reaction, and these reaction products ionize the ambient ^{3}He,

resulting in a detectable electrical pulse on the central electrode of the tube, which is biased to +1780 V. Electronic noise and γ-rays are present as low-pulse-height signals, and are eliminated with a fixed threshold discriminator.

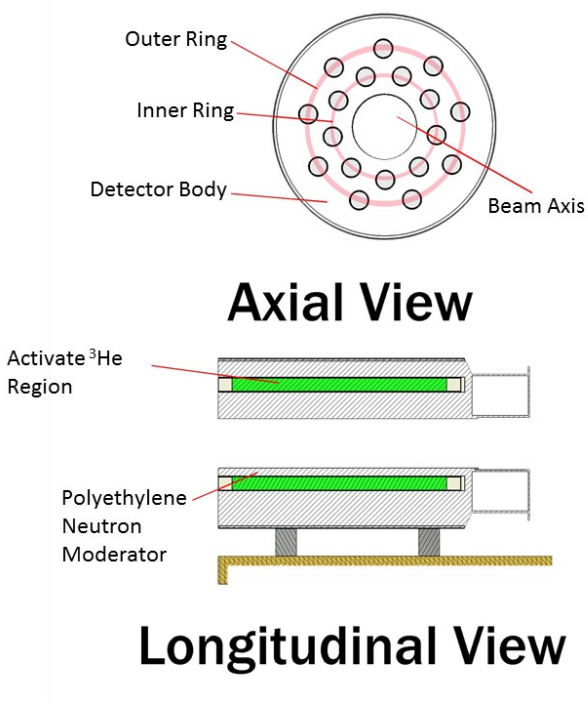

Figure 5.17: Schematic for model IV inventory sample counter (INVS), adapted from [Arnold et al., 2011]. ^{3}He proportional counters are embedded in polyethylene neutron moderator in two concentric rings.

INVS parameters	Dimensions
Inner ring radius	7.24 cm
Outer ring radius	10.60 cm
Polyethylene body length	46.2 cm
Polyethylene body diameter	30.5 cm
^{3}He pressure	6 atm
^{3}He cell active length	39.4 cm
Axial beamline cavity diameter	8.9 cm

Table 5.2: Dimensions of the INVS detector, taken from [Arnold et al., 2011].

5.5.1 INVS Energy Resolution

An important capability of the INVS detector is limited incident neutron energy resolution. On-board signal processing electronics within the detector output TTL logic signals for events occurring in the inner ring (I) or the outer ring (O). [Arnold et al., 2011] has shown that for neutron energies less than about 2 MeV, the mean energy of detected neutrons can be determined by the function:

$$\frac{I}{O} \propto E_n^{-\frac{1}{5}} \tag{5.4}$$

Where I and O represent hits in the inner and outer detector rings respectively, and E_n is the mean energy of the neutrons detected. It should be noted that this is only valid for neutrons originating from the center of the detector. This ratio of inner to outer ring events theoretically allow for limited neutron spectroscopy. A plot of the energy resolution of the INVS detector is shown is Figure 5.18. The measurement of the ^{22}Ne(α,n)^{25}Mg reaction has three potential neutron sources: $\approx$ 300 keV neutrons from the reaction of interest, $\approx$ 3 MeV neutrons from the ^{13}C(α,n)^{16}O reaction, and thermal neutrons from room background. The latter preferentially trigger the outer most ring of the ^{3}He counters, resulting in a value of I/O < 1 [Jack Silano, private communication]. The exact value is dependent on the location of all objects surrounding the detector, and can only be measured with the full experimental setup in place.

Using the known energies of the reaction of interest, contaminant reaction, the data from Figure 5.18, and the I/O value of the room backgrounds, it is theoretically possible to account for contaminant reactions by fitting room background measurements, measured off-resonance measurements, and simulated on-resonance events to the measured total spectrum (following a similar procedure to the fraction fitting described in Chapter 6).

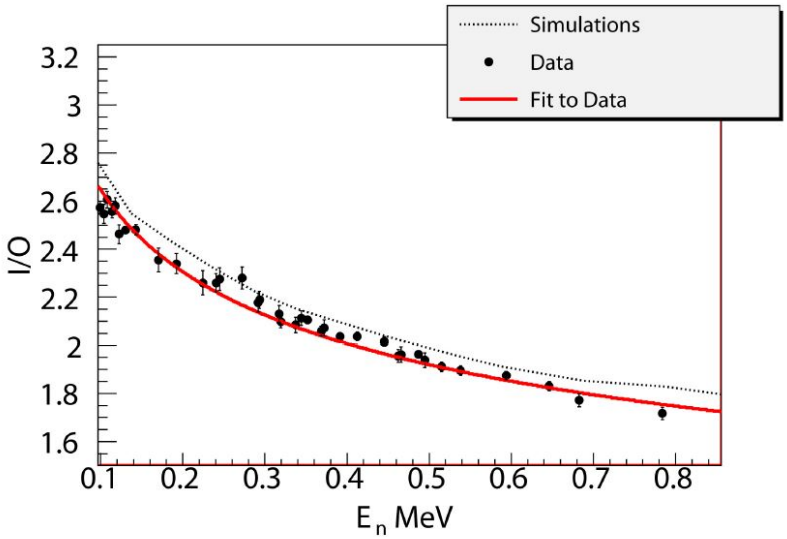

Figure 5.18: Ratio of neutron counts from the inner (I) and outer (O) rings of the INVS detector as a function of mean neutron energy, taken from [Arnold et al., 2011]. The I/O ratio can be used for neutron energies below 2 MeV, with the greatest resolution at the lowest energies.

5.5.2 INVS Simulated and Previously Measured Efficiency

Before the INVS can be used, the efficiency of the detector much be known. The efficiency for the INVS detector is defined as:

$$\epsilon \equiv \frac{N_d}{N_e} \tag{5.5}$$

where N_d is the number of neutrons detected, and N_e is the number of neutrons emitted by a source. The efficiency of the INVS detector was carefully measured [Arnold, 2011], using four distinct neutrons sources (^{252}Cf, ^{2}H(d,n)^{3}He, ^{7}Li(p,n)^{7}Be, and ^{2}H(γ,n)H). It should be noted that [Arnold, 2011] measured efficiency using a carbon plug inserted into the axial cavity to improve efficiency. The carbon plug will not be used in the eventual measurement of the ^{22}Ne(α,n)^{25}Mg reaction, but Jack Silano has shown that this only accounts for a small change in efficiency. Figure 5.19 shows simulated and measured efficiencies from [Arnold, 2011] and [Jack Silano, private communication]. The simulations in

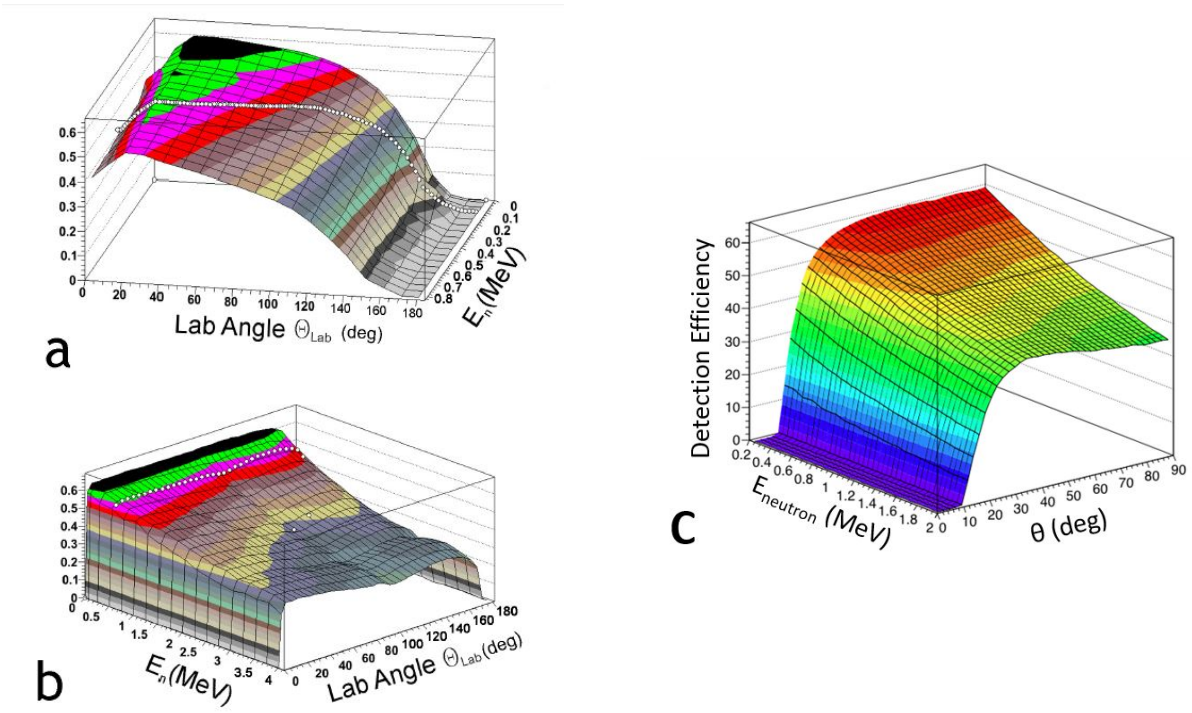

Figure 5.19: Neutron efficiency as a function of angle and energy. (a) and (b) are taken from [Arnold, 2011], and use data from a ^{7}Li(p,n)^{7}Be and ^{2}H(γ,n)H measurements, respectively. For the graphs, θ represents angle of neutron emittance from the source in the lab frame, with 180° being directly through the axial cavity in the center of the detector array. Graphs (a) and (b) were produced using the MCNPX Monte Carlo code [Pellowitz, 2007], using standard neutron libraries [Chadwick et al., 2006]. The white dots correspond to efficiencies sampled by combining kinematics and angular distribution data from the ^{7}Li(p,n)^{7}Be and ^{2}H(γ,n)H measurements (see [Arnold, 2011] for details). (c) was produced by Jack Silano using GEANT4, and does not use the carbon plug or electronic thresholds. These account for a difference in efficiency of around 3% [Jack Silano, private communication].

Figure 5.19a and Figure 5.19b were produced using the Monte Carlo N-Particle eXtended nuclear process toolkit (MCNPX) [Waters et al., 2007]. The white dots represent efficiencies sampled by combining kinematics and angular distribution data from the ^{7}Li(p,n)^{7}Be and ^{2}H(γ,n)H measurements (see [Arnold, 2011] for details). Figure 5.19c shows simulated efficiencies without the carbon plug using GEANT4 [Agostinelli et al., 2003, Allison et al., 2006].

5.5.3 INVS Electronics

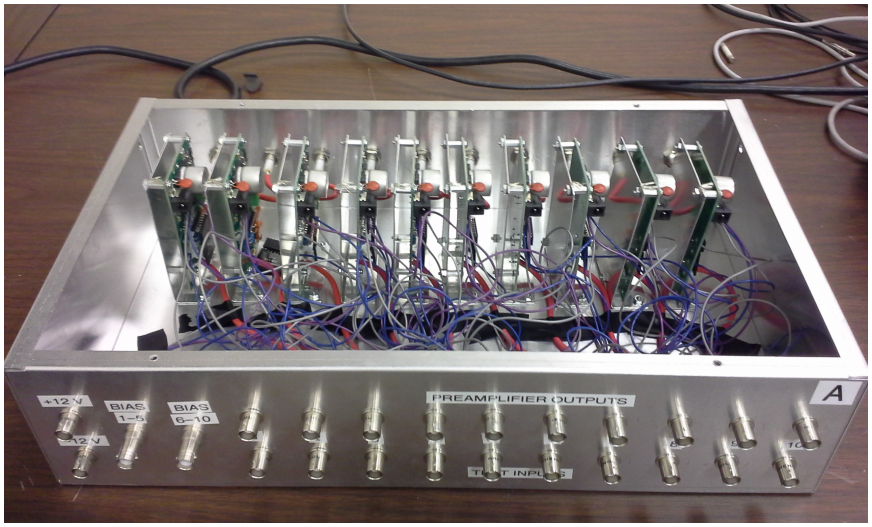

Figure 5.20: Preamplifier array constructed by Jack Silano for the INVS detector. Two boxes with 10 preamplifiers each were used for the 18 channels of the INVS.

The INVS detector has a total of 18 channels producing energy signals that must be processed. The original electronics used for [Arnold et al., 2011] combined the signals from all inner detectors together, and all the signals from the outer detectors together. This complicates the identification of problems with individual detector channels. A new set of electronics was designed for the proposed ^{22}Ne(α,n)^{25}Mg reaction measurement.

A VME-bus modules, NIM modules, and custom electronics were used to process these signals. Each channel was biased to +1780 V, using a multi-channel high voltage power supply. Signals from γ-ray and neutron events were amplified using a custom array of preamplifiers constructed by Jack Silano (see Figure 5.20). A spectroscopic amplifier received the preamplifed signals from the detector and generated an amplified energy signal and a fast output. The amplified signal was sent into an analog-to-digital converter (ADC). The fast output for all 18 channels was combined with linear fan-in modules and discriminated with a constant fraction discriminator (CFD). The discriminated signal was fed into a gate-delay generator, which triggered the ADC with a master gate. See Figure 5.21 for a schematic of this system.

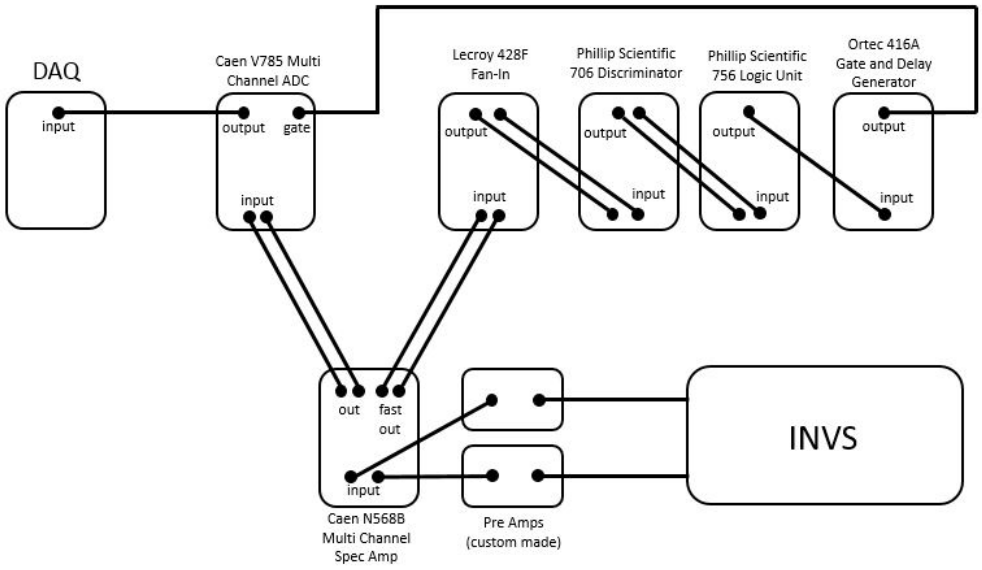

Figure 5.21: Electronics setup for 2 channels of the INVS detector. All 18 channels were configured in this manner, allowing an event in any channel to trigger the ADC and begin data collection. All events were stored, and software gates were used to discriminate between neutron and γ-ray events.

This produces a spectrum (shown in Figure 5.22) with clearly defined γ-ray and neutron peaks, allowing for excellent particle discrimination. The spectra from each individual channel are also summed into inner spectra (a summation of the data from the inner detector ring), outer spectra (a summation of the data from the outer detector ring), and total (a summation of all data from all channels).

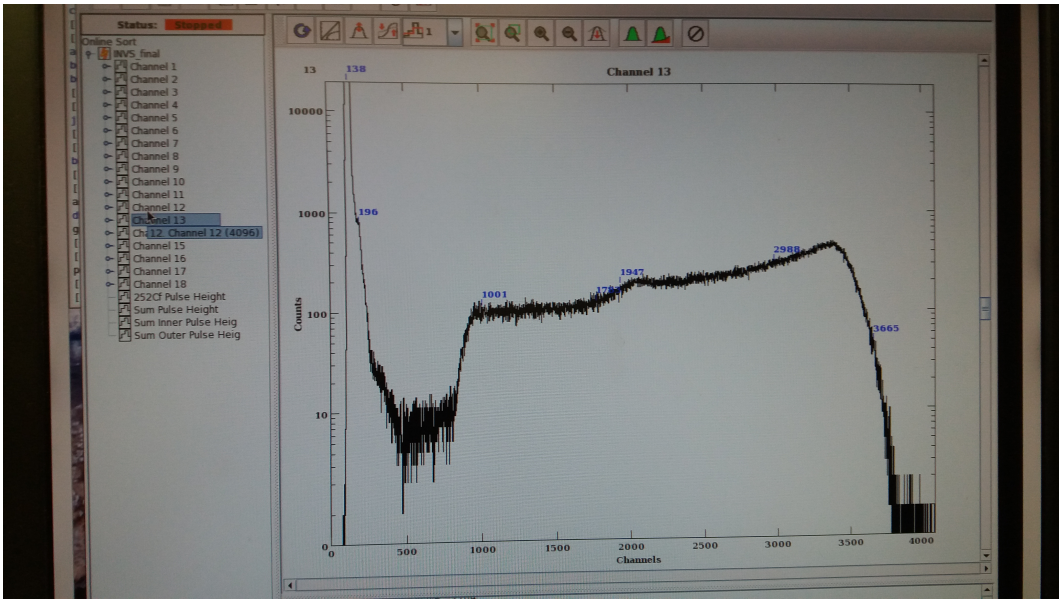

Figure 5.22: Example spectrum from a single channel of the INVS detector, shown in the data acquisition program JAM. The γ-ray peak is clearly identified on the left of the spectrum, and the large broad structure on the right is the signal from neutrons.

While the ^{22}Ne(α,n)^{25}Mg reaction was not measured in this study, the INVS as characterized here represent the best current candidate for the measurement, having high efficiency, some background discriminative abilities, and fully assembled and characterized electronics.

Chapter 6

Measurement of the 828 keV Resonance in the ^{22}Ne(α,γ)^{26}Mg Reaction

6.1 Preface

The astrophysical motivation for remeasuring the ^{22}Ne(α,γ)^{26}Mg and ^{22}Ne(α,n)^{25}Mg reactions is laid out in Chapter 1, but a summary of the experimental motivation for the remeasurement of the ^{22}Ne(α,γ)^{26}Mg reaction will be presented here. All energies are given in laboratory frame unless otherwise stated.

The 828 keV resonance in the ^{22}Ne(α,γ)^{26}Mg reaction has been directly measured only twice, once in [Wolke et al., 1989], and once in a PhD dissertation by M Jaeger (the results from the latter were never published outside the dissertation). Wolke's measurement used a high purity germanium detector, similar to the one described for this study in Chapter 5, and an extended gas cell target. As discussed in Chapter 2, multiple measurements of the ^{22}Ne(α,n)^{25}Mg reaction using the same gas cell target vary widely in the reported resonance strength, despite several having similar detector systems, and some of the measurements using the same accelerator and target. It is hypothesized here that the difficulty of maintaining and fully characterizing the pressures within a windowless gas cell target is one of the leading possible causes of potential systematic errors, and that error is perhaps present in the only direct measurement of the ^{22}Ne(α,γ)^{26}Mg reaction.

Limitations in the number of targets available for the experiment in this dissertation (see Chapter 4) led to the decision to focus on the measurement of the 828 keV resonance in the ^{22}Ne(α,γ)^{26}Mg reaction using the newly developed blister-resistant solid targets developed in Chapter 4. The ^{22}Ne(α,n)^{25}Mg reaction is predicted to require significantly more accumulated beam charge to measure and will be revisited when a new equipment

Energy (keV)	Reference
11301(9)	[Talwar et al., 2016]
11311(5)	[Endt, 1998]
11317(17)	[Talwar et al., 2016]
11319(2)	[Jaeger et al., 2001]
11321(1)	[Adsley et al., 2018]
11328(1)	[Massimi et al., 2017]
11329(1)	[Adsley et al., 2018]

Table 6.1: The density of energy levels near the excitation energy.

for implantation is procured.

It should be noted that there is significant disagreement in the literature about whether the 828(5) keV resonance in the ^{22}Ne(α,γ)^{26}Mg reaction measured by [Wolke et al., 1989] and the 831 keV resonance in the ^{22}Ne(α,n)^{25}Mg reaction are the same resonance (see [Adsley et al., 2018, Longland et al., 2012] for discussions on this). It has been assumed in this dissertation that they are the same resonance for simplicity of discussion, but the high density of energy levels near the excitation energy (see Table 6.1) adds to confusion as to what energy level should be used for simulations. Because [Wolke et al., 1989] is the only direct measurement of the ^{22}Ne(α,γ)^{26}Mg reaction, the value obtained from those data (11313(4) keV) is adopted for simulations in this dissertation.

The measurement of the strength of the 828 keV resonance in the ^{22}Ne(α,γ)^{26}Mg reaction used the 479 keV resonance in the ^{22}Ne(p,γ)^{23}Na reaction as a standard resonance [Kelly, 2016, Longland et al., 2010a]. Decay schemes used for both of the reactions are shown in Figure 6.1 and 6.2, and the branching ratios for the 479 keV resonance are given in Table 7.2 in Appendix C. The energy levels for the 828 keV resonance decay are taken from [Endt, 1998], except for the 11313 keV state in ^{26}Mg, which was obtained from [Wolke et al., 1989]. Branching ratios for the primary transitions are also taken from [Wolke et al., 1989], and secondary branching ratios are adopted from [Endt, 1998]. Energy levels for the 479 keV resonance decay and branching ratios are adopted from [Kelly, 2016].

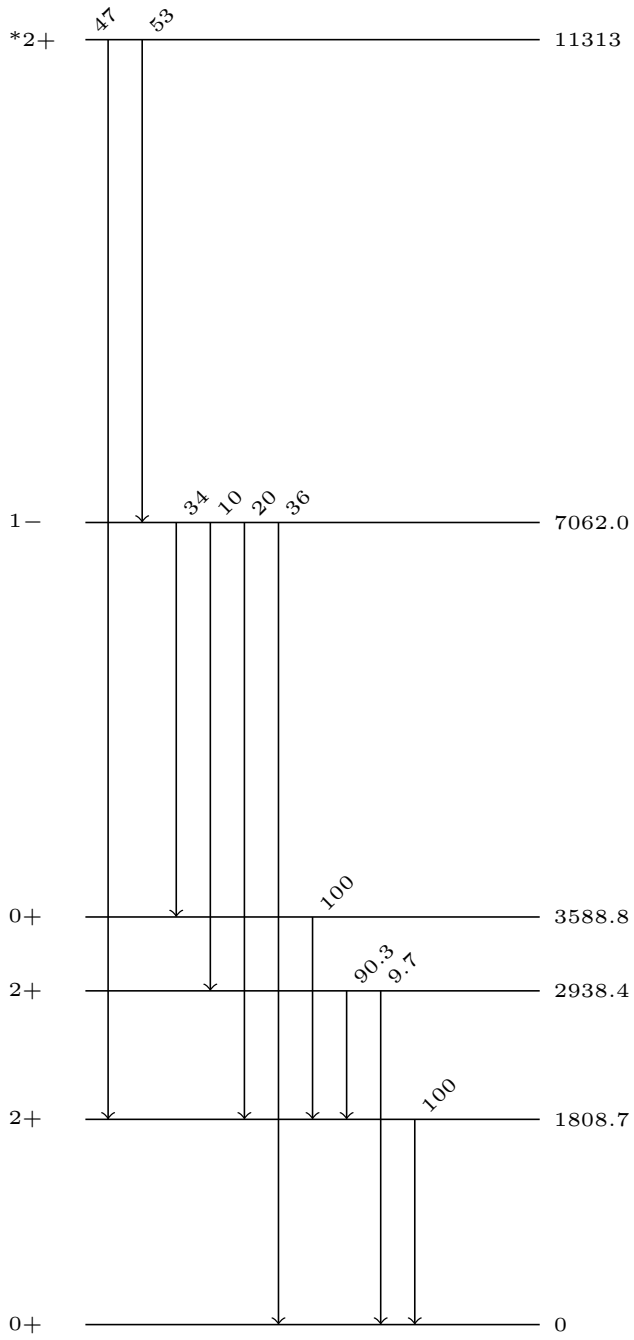

Figure 6.1: Decay scheme for the 828 keV resonance in ^{22}Ne(α,γ)^{26}Mg. The energy of the excitation state is taken [Wolke et al., 1989] (see Appendix B). The spin parity of the excited state (denoted by *) was adapted from [Giesen et al., 1993]. The other energy levels are adopted from [Endt, 1998], the primary branching ratios can be found in [Wolke et al., 1989], and the secondary branching ratios are taken from [Endt, 1998].

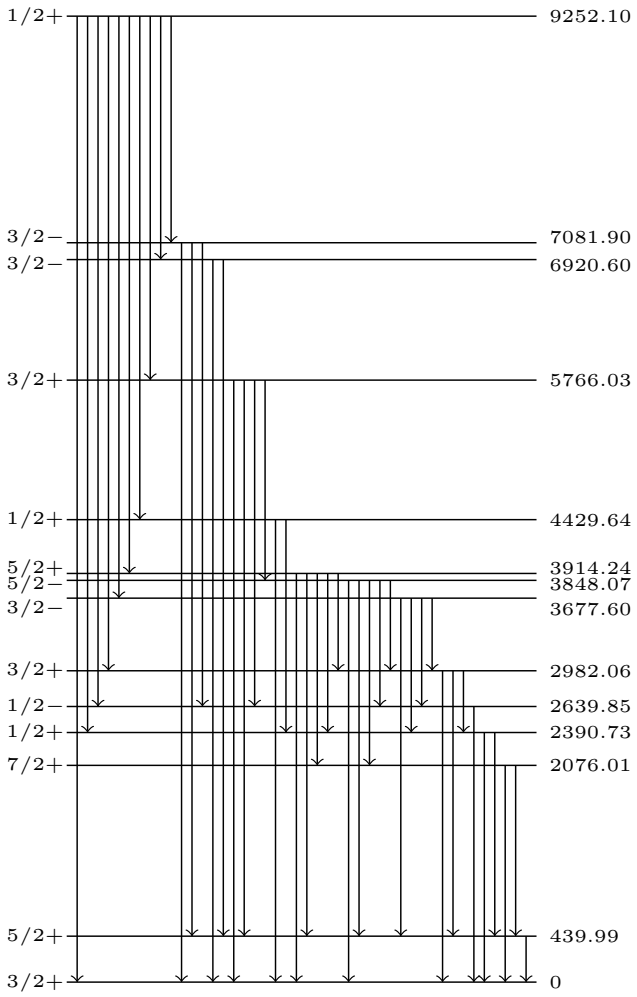

Figure 6.2: Decay scheme for the 479 keV resonance in the ^{22}Ne(p,γ)^{23}Na reaction. The energy levels and branching ratios are adopted from [Kelly, 2016], and can be found in Appendix C

6.2 Experimental Procedure

Data for this measurement were taken with the 1 MV JN Van de Graaff accelerator described in Chapter 3 modified for α-particle production and the $\gamma\gamma$-coincidence HPGe setup detailed in Chapter 5. The detector was placed flush with the target chamber (the

target itself was 1.1 cm from the HPGe detector face). The targets were the evaporated porous titanium targets described in Chapter 4. Two targets were fabricated for this experiment, one of which was used to obtain off-resonance data before being damaged by a faulty rastering system, and one of which was used to collect the on-resonance data. The targets were implanted at a 75 keV implantation energy for the on-resoance target, and 45 keV for the off resonance target, and during implantation accumulated 1 C of charge each to ensure saturation of the implanted material was reached. The beam energy chosen for the 828 keV resonance was 904 keV. This value was chosen by modeling the energy loss of an α particle within a target backing. A 904 keV α particle loses energy within the target backing, and has a kinetic energy of 828 keV at a depth of 0.17 μm. A 493 keV proton traversing the same target has a kinetic energy of 479 keV at 0.17 μm into the target. This shows that the chosen bombarding energy falls in the higher energy quarter of the plateau of the yield curves (Figure 6.5. It should be noted that the first YC shown in the figure has slightly shifted energy values due to accelerator instability during the production of that YC). Off-resonance data were collected at α-particle energies of 815 keV.

The α-particle beam currents on target were maintained at 50 μA throughout data collection and deadtime averaged 1.58% across all collected on-resonance data. The total accumulated charge on target was $\approx$ 4.4 C, though only 3.436480 C of that represented usable data. Approximately 1.4 C of usable off-resonance data were collected before the second target was damaged by the accelerator. The 479 keV resonance in ^{22}Ne(p,γ)^{23}Na was used as a standard resonance in this study, and the ^{22}Ne(α,γ)^{26}Mg measurement is dependent upon the accuracy of that standard resonance, as measured by [Kelly, 2016] and [Longland et al., 2010a].

6.3 Fraction Fitting

Fraction fitting is a method of full spectral decomposition developed by previous graduate students at LENA [Buckner, 2014, Daigle et al., 2016, Dermigny et al., 2016]. This

was used to measure the standard resonance in ^{22}Ne(p,γ)^{23}Na and analyze data from the ^{22}Ne(α,γ)^{26}Mg. This method develops templates for each possible contribution to a total spectra (every primary decay of interest, beam induced background, room background, etc.), which are then varied to reconstruct the measured data (this process is illustrated in Figure 6.3). The templates are fed into an extended binned likelihood function [Barlow, 1990] which represents the probability of obtaining data (**D**) given the m template fractions (**F**), and is given in [Barlow and Beeston, 1993] as:

$$P(\mathbf{D}|\mathbf{F}) = \Big[\sum_{i=1}^{n} D_i \ln f_i - f_i\Big] + \Big[\sum_{i=1}^{n}\sum_{j=1}^{m} a_{ji} \ln A_{ji} - A_{ji}\Big] \tag{6.1}$$

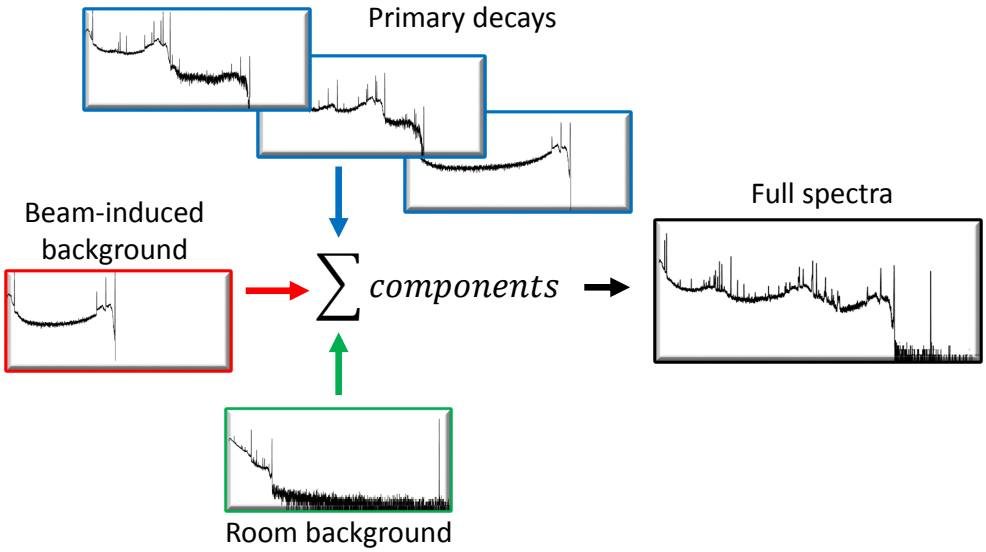

Figure 6.3: Illustration of the process of fraction fitting. Templates representing various components of the measured data are varied to reproduce the actual data.

where n represents the total number of bins, i is a given bin, f_i is the total number of events (contributed by all templates), A_{ji} is the predicted mean in template j, and a_{ji} is the observed number of events in template j. The term A_{ji} accounts for the the statistical fluctuations in a_{ji}, which are sampled from finite Monte Carlo calculations.

The f_{ji} term is possibly the most important component of the likelihood function, and is defined as:

$$f_i = \sum_{j=1}^{m} \frac{A^{data}}{A_j^{sim}} F_j A_{ji} \tag{6.2}$$

where A^{data} is the total area of the data within the measured spectrum, and A_j^{sim} is the total area of a simulated template j within the measured spectrum. The fractions F_j for the majority of this study are found using the `Minuit` library [James, 1975]. Details of this method can be found in [Buckner, 2014]. The low statistic data in Section 6.6 used both the `Minuit` method and a Bayesian method to determine the fractions. The reader is referred to [Dermigny, 2018] for a detailed explanation of the Bayesian method. The fraction fitting work in this dissertation was performed with a python-based GUI developed by Jack Dermigny [Dermigny et al., 2016].

6.4 Targets and Target Degradation

Only two targets were used in this study, so it was critical to characterize the implanted ^{22}Ne content and properly model the target degradation. The first target was used to measure the standard resonance in the ^{22}Ne(p,γ)^{23}Na reaction and to collect off-resonance data and will be referred to in this section as *Target 1*. The second target was used to collect all on-resonance data, and will be referred to as *Target 2*. Both targets had their ^{22}Ne content carefully measured, and Target 2 was carefully monitored throughout data collection.

The yield curve of the 479 keV resonance in the ^{22}Ne(p,γ)^{23}Na reaction with the highest statistics was measured using Target 1. All data points on the plateau of the target were summed to produce a single spectrum, and then the spectrum was trimmed until only a single representative peak from each template used remained in the spectra. The peaks chosen were primaries, escape peaks, or secondaries that were unique to a particular decay branch in the excited state of ^{23}Na and a unique peak for each background template used. Figure 6.4 shows the fraction fit spectra and identifies the reaction peaks

and contaminant peaks. The black line is the measured data, the red line is the sum of all the templates used, and the various other lines are individual templates for the reaction of interest and contaminants. The black arrows originating at the top of the image identify the peaks from the reaction of interest and the brown arrows originating at the bottom of the image identify the contaminant peak. Table 6.2 gives the information on the peaks of interest in Figure 6.4.

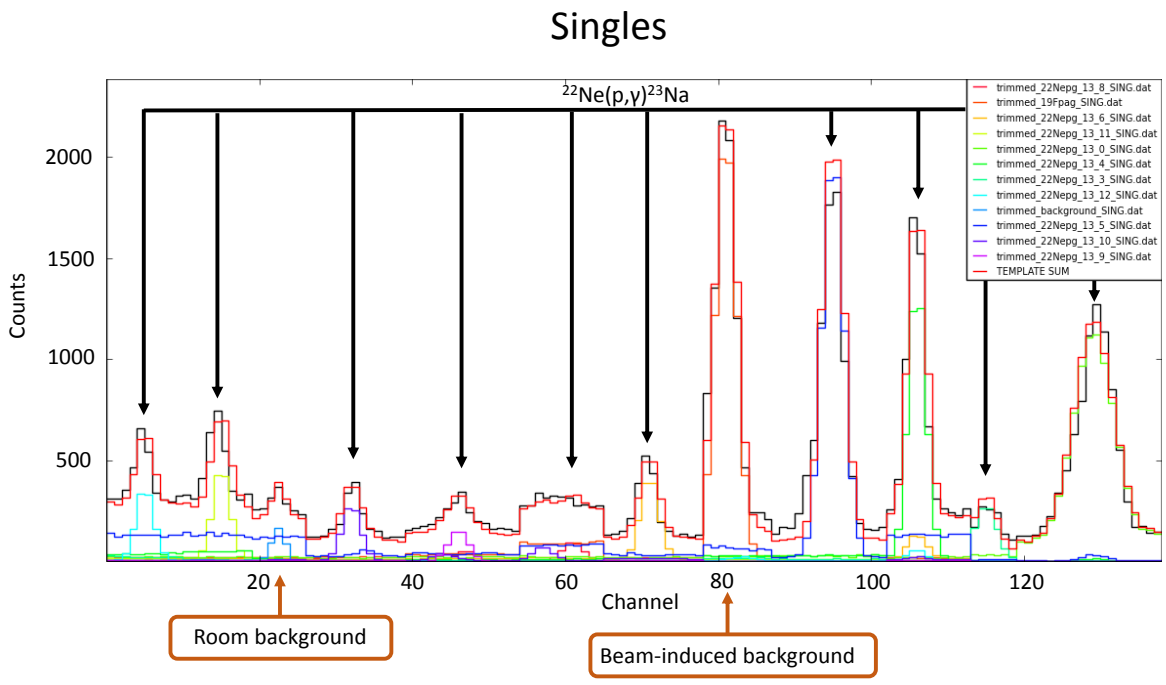

Figure 6.4: Output of the fraction fitting GUI used to analyze the 479 keV resonance in the ^{22}Ne(p,γ)^{23}Na reaction. This spectrum is a patchwork of distinct regions from the entire measured spectrum. Each region contains a peak of interest (usually a primary peak). The black line is the measured data, the red line is the sum of all the templates used, and the various other lines are individual templates for the reaction of interest and contaminants. The black arrows originating at the top of the image identify the peaks from the reaction of interest, and the brown arrows originating at the bottom of the image identify the contaminant peak. Table 6.2 gives the information on the peaks of interest.

Reaction	Transition (keV)	γ-ray measured (keV)
^{22}Ne(p,γ)^{23}Na	$9252.1 \rightarrow 7082.0$	2170.1 (primary)
^{22}Ne(p,γ)^{23}Na	$9252.1 \rightarrow 6920.6$	2331.4 (primary)
Room background	N/A	2614.5 (^{208}Tl)
^{22}Ne(p,γ)^{23}Na	$9252.1 \rightarrow 5766.0$	3486.1 (primary)
^{22}Ne(p,γ)^{23}Na	$9252.1 \rightarrow 4429.6$	4822.5 (primary)
^{22}Ne(p,γ)^{23}Na	$9252.1 \rightarrow 3914.2$	5337.9 (primary)
^{22}Ne(p,γ)^{23}Na	$9252.1 \rightarrow 3677.6$	3246.0 (secondary)
^{19}F(p,$\alpha\gamma$)^{16}O	$6126.9 \rightarrow 0.0$	6126.9 (primary)
^{22}Ne(p,γ)^{23}Na	$9252.1 \rightarrow 2982.1$	6270.0 (primary)
^{22}Ne(p,γ)^{23}Na	$9252.1 \rightarrow 2639.9$	2642.0 (secondary)
^{22}Ne(p,γ)^{23}Na	$9252.1 \rightarrow 2390.7$	6861.4 (primary)
^{22}Ne(p,γ)^{23}Na	$9252.1 \rightarrow 0.0$	8741.1 (escape peak)

Table 6.2: Table of γ-rays representing individual fraction fitting templates displayed in Figure 6.4. In cases when the primary γ-ray had significant contamination in the spectra, a secondary γ-ray was chosen that was unique to that decay branch. The ground state transition was measured using an escape peak so that a simple comparison to the coincidence spectra (which excluded the primary peak) could be made (see Section 6.5)

The fitter outputs the fraction of each template needed to produce the best fit, which can be converted into branching ratios and reaction numbers. The branching ratios reproduced in this dissertation match those found in [Kelly, 2016], as shown in Table 6.6 in Section 6.5, indicating a sufficiently accurate fit to use for target characterization.

Yield curve measurements of this same resonance in Target 2 did not have high enough statistics to fraction fit accurately. The 6270 keV γ-ray from the 9252.1 keV $\rightarrow$ 2982.1 keV transition in ^{22}Ne(p,γ)^{23}Na reaction was measured instead and compared the same measured γ-ray in Target 1. The resonances measured in this section are narrow, allowing the use of the equation

$$Y_{\Delta E \rightarrow \infty} = \frac{\lambda_r^2}{2} \frac{\omega\gamma}{\epsilon_{eff}} \tag{6.3}$$

where $\omega\gamma$ is the resonance strength (for the 479 keV resonance in the ^{22}Ne(p,γ)^{23}Na reaction, this value is 0.583(43) eV, taken from [Kelly, 2016]), ϵ_{eff} is the effective stopping power at the resonance energy, and λ_r is the de Broglie wavelength. The effective

Total Reactions (from Fraction Fitter)	$2376075(19345)$
Accumulated charge	$5059(152)\mu$C
Yield (reactions/particle)	$7.76(0.24) \times 10^{-11}$
ϵ_{eff}	$7.4(0.4) \times 10^{-14}$ (eV/cm^2)
Stoichiometry (Ti:Ne)	$3.8(0.4) : 1$
Counts in 6270 keV peak per μC	$1.46(0.06)$

Table 6.3: Parameters extracted from the $^{22}(p,\gamma)^{23}$Na reference resonance using the fraction fitting and equations described in this Chapter. The counts in the 6270 keV peak were obtained from the yield curve fitting program described in this Chapter.

stopping power is given by

$$\epsilon_{eff} = \epsilon_X + \frac{n_Y}{n_X}\epsilon_Y \tag{6.4}$$

where n_Y is the number of inactive nuclei per square centimeter, n_X is the number of active nuclei per square centimeter, ϵ_Y is the stopping power of the inactive nuclei in the center-of-mass frame, and ϵ_X is the stopping power of the active nuclei in the center-of-mass frame.

The stoichiometry, effective stopping power, and parameters used to calculate those values for the reference resonance are shown are shown in Table 6.4.

The effective stopping power for Target 1 was compared to the observed 6270 keV counts and used to monitor the ^{22}Ne content in Target 2. When comparing two targets using the same resonance, for any individual peak, the following expression can be used

$$Y_1\epsilon_1^{eff} = Y_2\epsilon_2^{eff} \tag{6.5}$$

where Y is the measured yield from a particular peak, and ϵ^{eff} is the effective stopping power. To determine the maximum yield of each target, a yield curve program developed by Jack Dermigny was employed. The program is based on `YCurve.R` which is

described in Chapter 4, but uses Bayesian posterior probability distributions for the maximum yield, the beam-width, the beam straggling, and the thickness of the implanted region. For details regarding the program and parameters, please see Appendix A.1 of [Dermigny, 2018]. Figure 6.5 shows the first 4 yield curve plots obtained by the code. The blue line represents the fit to the data, and the width of the line represents the corresponding uncertainty.

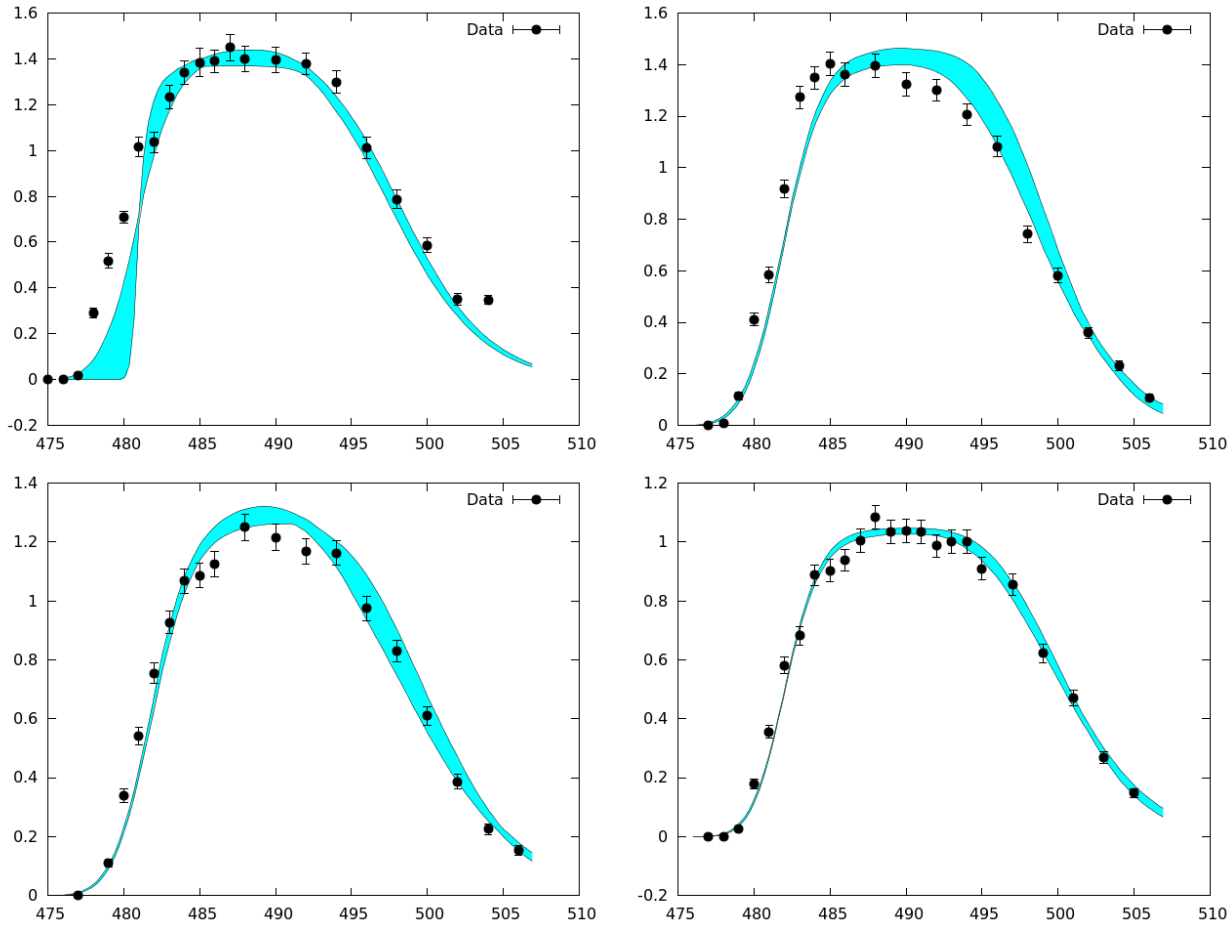

Figure 6.5: ^{22}Ne(p,γ)^{23}Na Yield curves for target 2. (Upper left) 0 C accumulated. (Upper right) 1.5 C accumulated. (Lower left) 2.5 C accumulated. (Lower right) 3.5 C accumulated.

Figure 6.6 shows some of the measured yields from the yield curve program of the 6270 keV γ-ray of Target 2 throughout data collection. Table 6.4 shows the measured 6270 keV γ-rays, the effective stopping power, and the stoichiometries of the target.

Charge	6270 keV Counts	ϵ_{eff} (10^{-14}eV/cm^2) (CoM frame)	Ti:Ne
0.0	1.44 ± 0.09	7.5 ± 0.8	3.9 ± 0.5
1.5	1.43 ± 0.06	7.6 ± 0.7	3.9 ± 0.4
2.5	1.34 ± 0.05	8.1 ± 0.8	4.2 ± 0.5
3.5	1.04 ± 0.04	1.04 ± 1.0	5.6 ± 0.6
4.4	0.91 ± 0.04	1.18 ± 1.2	6.4 ± 0.7

Table 6.4: Parameters from the $^{22}(p,\gamma)^{23}$Na yield curves measured between α-beam data collection periods. Effective stopping power was obtained by comparing the yield of the 6270 keV peak with the yield from the reference resonance, and using the linear relationship between the effective stopping power and measured yield (see Equation 6.5. Stoichiometries are obtained from equation 6.4.

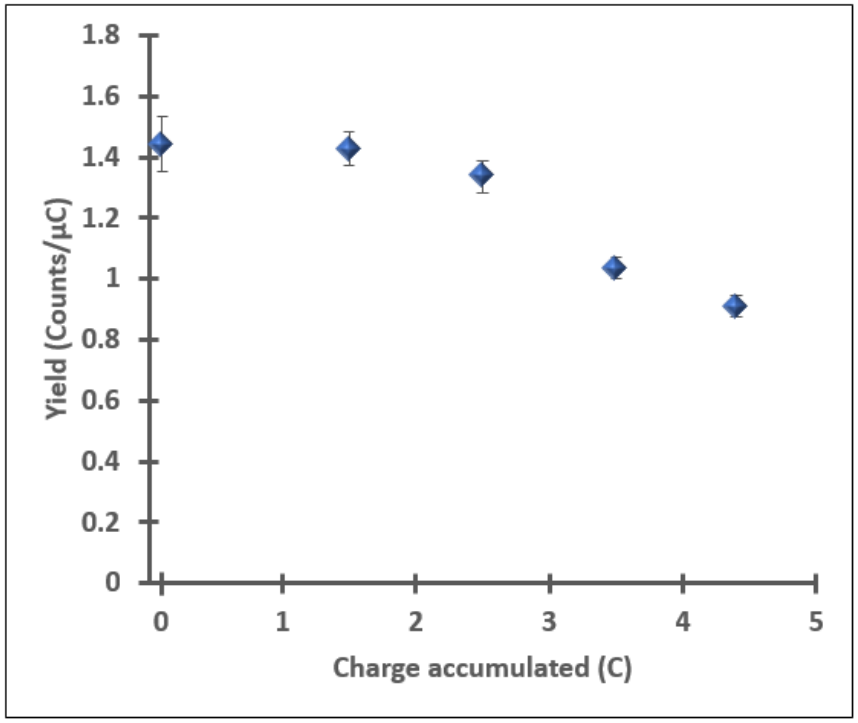

Figure 6.6: Yield of the 6270 keV γ-ray from the ^{22}Ne$(p,\gamma)^{23}$Na reaction in Target 2 as a function of charge accumulated.

The data shown in Table 6.4 were used in Equation 6.3 to calculate the effective stopping power of the target at each yield curve using the effective stopping powers from SRIM for α particles at 830 keV in Ti and Ne. From this, an average stopping power was calculated for each data collection period and is shown in Table 6.5. It should be noted

Charge accumulation period (C)	ϵ_{eff}^{avg} (10^{-13}eV/cm^2)
0.0 - 0.5 C	3.19 ± 0.34
1.5 - 2.5 C	3.32 ± 0.33
2.5 - 3.5 C	3.92 ± 0.37
3.5 - 4.4 C	4.70 ± 0.45

Table 6.5: Average effective stopping power for each data collection period.

that temporary technical issues measuring current of the target collimator (see Chapter 3) because of a disconnected ground wire led to unusually high background events for 1 C of collected data and only the first 0.5 C of the first 1.5 C of collected data could be used.

To account for this increase in effective stopping power (and corresponding decrease in signal of interest), a Beam Current Integrated (BCI) weighted average was used to develop an average effective stopping power for the entire data set via the relation

$$\epsilon_{eff}^{BCI} = \frac{\sum_i \epsilon_{eff,i}^{avg} N_{\alpha,i}}{\sum_j N_{\alpha,j}} \tag{6.6}$$

where indices i and j refer to each data acquisition period and $N_{\alpha,i}$ is the number of α particles accumulated during the data acquisition period i or j. Rather than add uncertainties in quadrature for this average, which would produce artificially low values, a weighted average of the uncertainties listed in Table 6.5 was also taken using the same formalism. The final value of the BCI-weighted average effective stopping power for all data collected on Target 2 was

$$\epsilon_{eff}^{BCI} = (3.84 \pm 0.38) \times 10^{-13}\text{eV/cm}^2 \tag{6.7}$$

6.5 Coincidence Efficiency

The signals from the 828 keV resonance in the ^{22}Ne(α,γ)^{26}Mg reaction are very weak, and cannot be differentiated from room background without use of both the $\gamma\gamma$-coincidence and $\gamma\mu$-anticoincidence systems detailed in Chapter 5. Figure 6.7 illustrates this, with

the top panel representing a portion of the HPGe spectra with no gating, the center panel showing the same spectra with $\gamma\gamma$-coincidence gating, and the bottom panel shows the spectra with $\gamma\mu$-anticoincidence applied. The red area indicates the location of the strongest secondary γ-ray peak in the spectra.

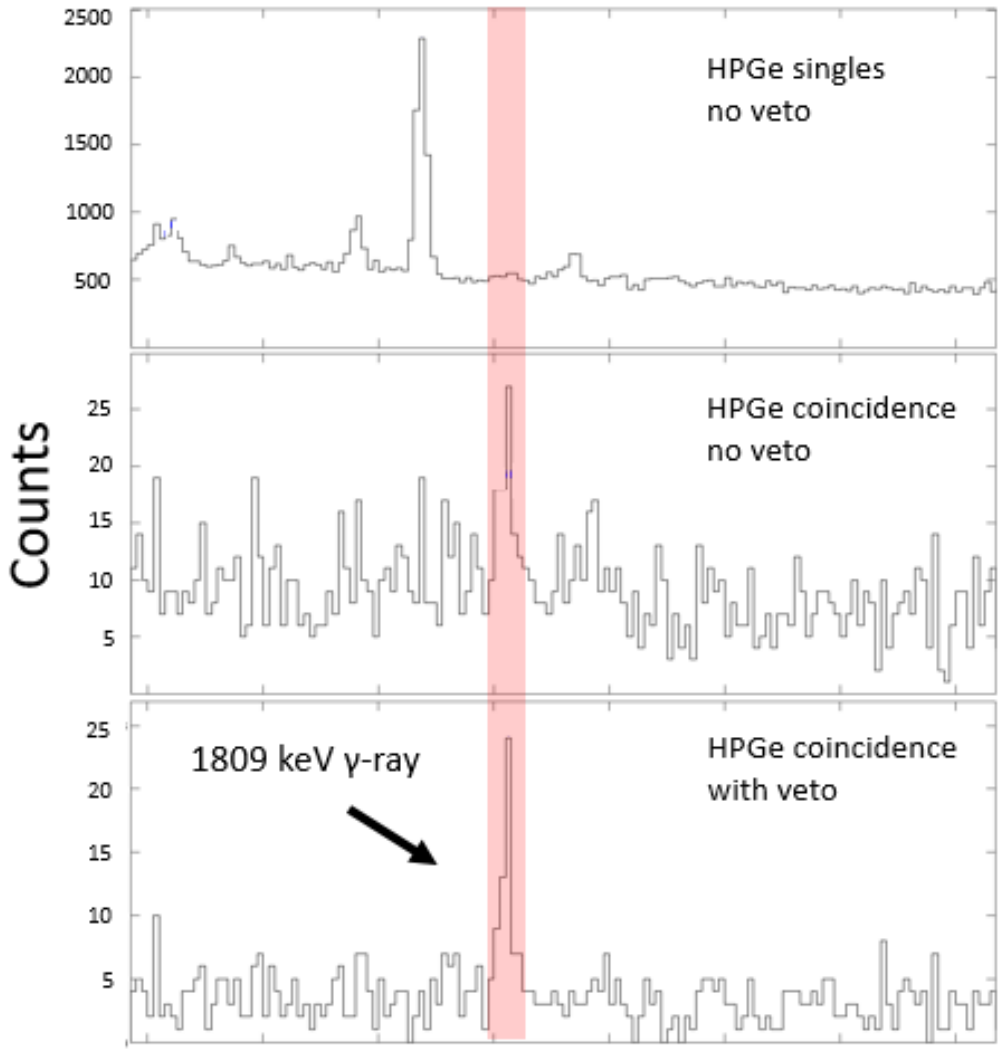

Figure 6.7: Spectra illustrating the $\gamma\gamma$-coincidence and $\gamma\mu$-anticoincidence applied to the 828 keV resonance. (Top) Singles spectra from the HPGe detector zoomed in to a region of interest. (Center) The same spectra with $\gamma\gamma$-coincidence applied. (Bottom) The $\gamma\gamma$-coincidence spectra when $\gamma\mu$-anticoincidence is used. The red area indicates the location of the strongest secondary γ-ray peak in the spectra

To set up the coincidence described in Chapter 5, a two dimensional energy gate must

be set between the HPGe and NaI detectors. This is a software gate generated in JAM (Chapter 5) and is chosen to maximize the signals seen from the decay of interest (see Figure 6.1). The gate chosen for this experiment included events whose total energy deposition in all detectors measured $7000 - 11500$ keV and excluded all other total energy deposition values. This gate was chosen through trial and error to minimize background while maximizing the signal of the 1809 keV secondary γ-ray. Figure 6.8 shows a two-dimensional plot of measured energies in the HPGe (x-axis) and the sum of all the NaI detectors (y-axis). The red trapezoid is the gated region of accepted events.

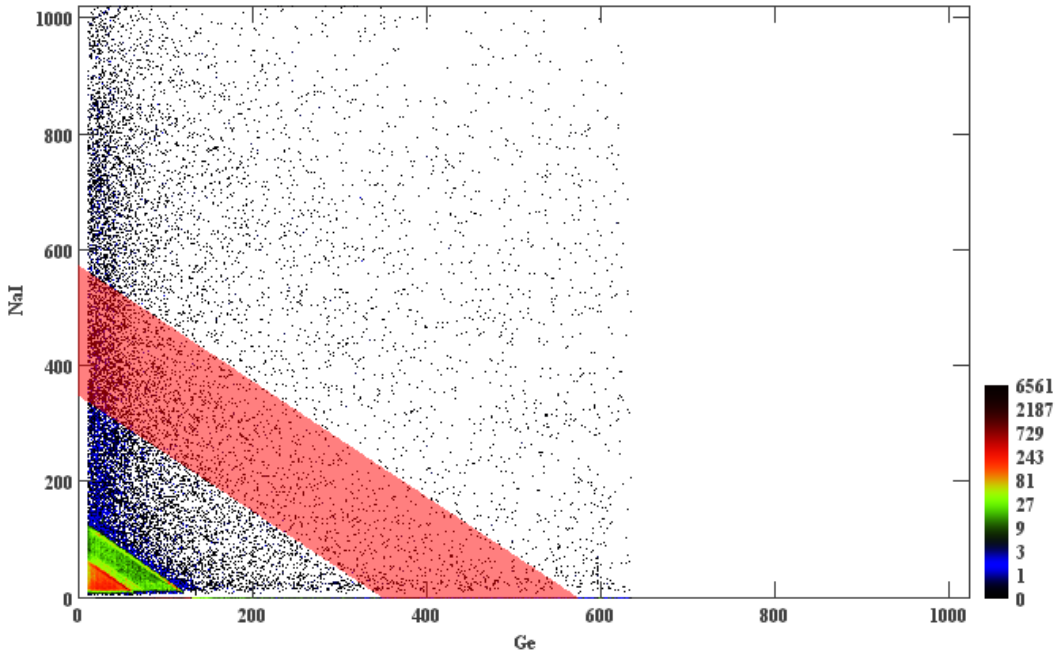

Figure 6.8: Two-dimensional plot of measured energies in the HPGe (x-axis) and the sum of all the NaI detectors (y-axis). The red trapezoid is the gated region of accepted events. The small dense triangular region in the lower left is composed of signals originating almost entirely from room background.

The efficiency measurement of the HPGe detector is detailed in Chapter 5, but coincidence efficiency is handled differently because the efficiency is unique to each coincidence energy gate. Others have shown that our simulations accurately represent the detector [Dermigny et al., 2016, Howard et al., 2013], but an additional check was performed for the specific energy gate chosen for this experiment.

Transition	FF BR (singles)	FF BR (coincidence)	BR (singles) [Kelly, 2016]	BR (coincidence) [Kelly, 2016]
$R \rightarrow 0$	39.97(68)	38.54(108)	41.77(67)	41.23(71)
$R \rightarrow 2391$	4.89(21)	3.65(21)	4.05(12)	4.05(13)
$R \rightarrow 2640$	8.24(19)	9.57(28)	8.27(18)	8.29(20)
$R \rightarrow 2982$	32.19(56)	33.83(71)	31.73(52)	32.79(58)
$R \rightarrow 3678$	4.65(17)	4.65(32)	4.85(16)	4.77(16)
$R \rightarrow 3914$	1.23(16)*	0.37(17)*	0.37(9)	0.05(24)
$R \rightarrow 4430$	1.73(15)	2.13(20)	1.69(9)	1.61(15)
$R \rightarrow 5766$	2.53(11)	2.30(14)	2.78(9)	2.70(13)
$R \rightarrow 6921$	2.71(12)	2.85(17)	2.43(9)	2.49(11)
$R \rightarrow 7082$	2.04(10)	2.10(15)	2.06(9)	2.03(11)

Table 6.6: Comparison of branching ratios of the 479 keV resonance in ^{22}Ne(p,γ)^{23}Na. The values labeled FF BR are the branching ratios determined from the fraction fitting in this study. These are compared to the most recent measured values [Kelly, 2016]. Upper limits are denoted by *.

The coincidence gate used for the ^{22}Ne(α,γ)^{26}Mg measurement was applied to the 479 keV resonance data in ^{22}Ne(p,γ)^{23}Na used to characterize the target in Section 6.4. Branching ratios were compared between the singles spectra, coincidence spectra, and literature values. Table 6.6 shows the results of this comparison. Although less charge was accumulated in the present work compared to [Kelly, 2016], values for branching ratios match each other in singles and coincidence for the data from the 479 keV ^{22}Ne(p,γ)^{23}Na measurement. Additionally, the values for the branching ratios in singles and coincidence are reasonably close to the values obtained by [Kelly, 2016], which was a higher-statistics study of this resonance. This confirms the accuracy of the simulations with the particular coincidence gate chosen for this study.

The coincidence gate was applied to the 828 keV resonance whose decay scheme is shown in Figure 6.1. The branching ratios for the primary transition are taken from [Wolke et al., 1989], and secondary branching ratios are taken from [Endt, 1998]. These values were used to run a full coincidence simulation of the 828 keV resonance in ^{22}Ne(α,γ)^{26}Mg in `Geant4`, and the number of background-reduced events in the 1809 keV secondary γ-ray was measured and compared to the number of simulated events. It was determined that the coincidence efficiency at 1809 keV with the $7000 - 11500$ keV 2D energy gate was 0.0095 for this particular γ-ray.

6.6 Analysis

Because of the low statistics of the signals from the 828 keV resonance, multiple methods of analysis were performed to corroborate the results. While primary γ-rays from the 828 keV resonance were detected, the number of counts for each primary were very low. The 1809 keV secondary γ-ray is the strongest signal from the resonance detected and the first method of analysis used only this secondary to obtain a resonance strength.

Initial data analysis utilized the data acquisition system JAM (Chapter 5) for peak analysis. The secondary peak of interest was identified, and the net area was measured using JAM Net Area tool, which uses background markers to identify regions-of-interest for background reduction and measures the background-reduced net area of a peak.

The full simulated decay of the 828 keV resonance in ^{22}Ne(α,γ)^{26}Mg described in Section 6.5 shows that with the current detector setup the coincidence efficiency for the $1809 \rightarrow 0$ keV decay (assuming literature branching ratios) is 0.0095. The total counts and coincidence efficiency were used to obtain the total number of reactions, shown in Section 6.7. That number was used to calculate the resonance strength with Equation 6.3.

The second method of analysis used the Fraction Fitting described in Section 6.3. Templates for the 11313 $\rightarrow$ 7062 and 11313 $\rightarrow$ 1809 primary transitions were generated, as these were the only primary transitions identified by [Wolke et al., 1989], and no additional primary peaks could be identified in the data taken for this dissertation. Efforts were made to properly account for Doppler shifting and Doppler broadening, which are detailed in Appendix A, and were applied to the primary templates.

After applying the $\gamma\gamma$-coincidence and $\gamma\mu$-anticoincidence gates, both beam-induced and room background data were too noisy to obtain a proper fit. It was estimated that approximately 2 full weeks of 24 hour runtime would be needed to obtain the statistics needed to produce reasonable background templates. The beam-induced and room background templates did reveal that the background local to the peaks of interest was relatively flat, leading to the use of manually generated flat background templates for all

regions.

Fraction fitting was performed with both the binned likelihood method [Dermigny et al., 2016] and Bayesian method [Dermigny, 2018]. An example fit (in this case, the likelihood fit) is shown in Figure 6.9. The top panel shows the various fit regions, with the left most region being the 1809 keV secondary, while the center and right regions are the primaries detected. Black arrows indicate the primary peaks. The bottom panel shows the fit from the binned likelihood method. Black denotes the measured data, red is the sum of the templates, and the various other colored lines are the primary and background templates.

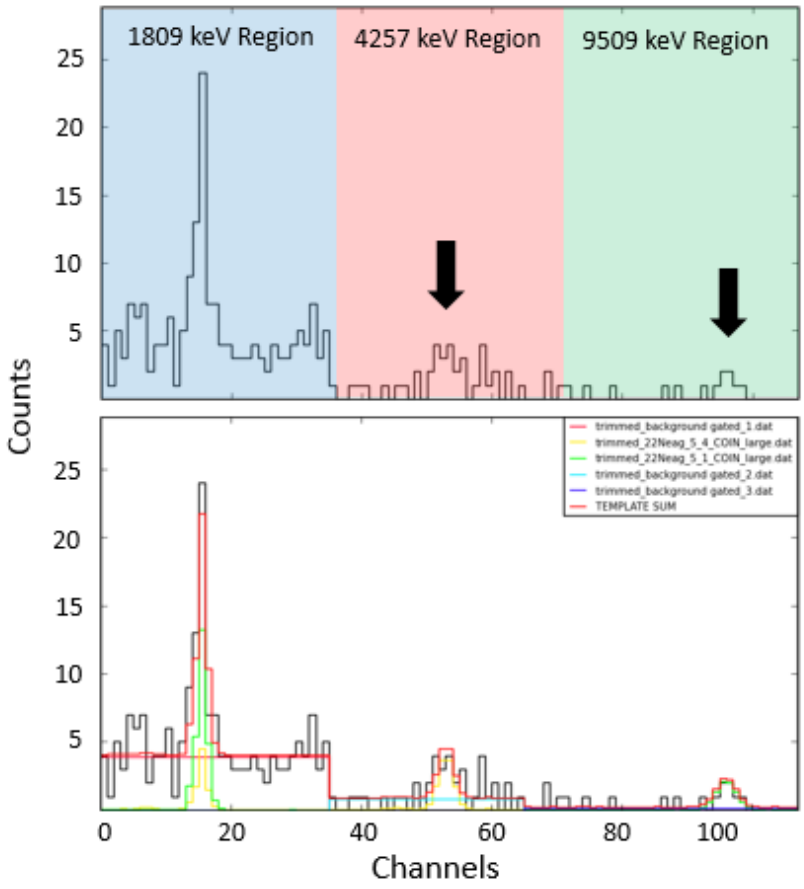

Figure 6.9: (Top) The various fit regions, each labeled with the γ-ray being fit within the panel. Black arrows indicate the primary peaks. (Bottom) The fit from the binned likelihood method. Black is the measured data, red is the sum of the templates, and the various other colored lines are the primary and background templates.

Parameter	Value
Total accumulated charge	3.436480 C
ϵ_{eff}^{ave}	$(3.84 \pm 0.38) \times 10^{-13}$eV/cm^2
Counts (1809 keV γ-ray)	43.18 ± 10.43
Average detector dead time	1.58%
Coincidence efficiency (1809 keV γ-ray)	0.0095

Table 6.7: Parameters used to calculate the resonance strength in ^{22}Ne(α,γ)^{26}Mg. Counts is the background subtract net area of the peak, ϵ_{eff}^{ave} is the BCI-weighted average effective stopping power in the CoM frame, and coincidence efficiency is the number of events detected per decay using the coincidence gate given in Section 6.5.

The resulting total number of reactions measured, branching ratios derived, and resulting measured resonance strength are given in Section 6.7. Values for excitation energy are given in Section 6.8.

6.7 Resonance Strength Results

The results from the analysis of the strongest secondary γ-ray, assuming branching ratios from [Wolke et al., 1989], and the binned likelihood and Bayesian analysis methods are shown in Table 6.8. Because the 828 keV resonance in ^{22}Ne(α,γ)^{26}Mg reaction is narrow, Equation 6.3 can be used to determine the resonance strength. The total reaction numbers found in Section 6.6 and the effective average stopping power found in Section 6.4 were used. For convience, all parameters needed to calculate the resonance strength for the tranditional analysis method are given in Table 6.7.

Table 6.8 shows the resulting total reaction number, assumed or derived branching ratios, and calculated resonance strength.

It should be noted that the fraction fitting methods produce a significantly lower value for the resonance strength, as compared to a traditional analysis of the 1809 keV secondary γ-ray. The fraction fitter seems to underestimate the strength of the 1809 keV γ-ray (see Figure 6.9), indicating the presence of one or more additional unidentified primary branches. The presence of undetected additional primary branches will also have

Method	Reaction number	Primary BR$_{(R\rightarrow 7062)}$	Primary BR$_{R\rightarrow 1809)}$	$\omega\gamma$ (meV)
Secondary peak analysis	4476(1081)	53(4)*	47(4)*	0.047(12)
Binned likelihood fraction fitting	3588(775)	50(19)	50(23)	0.038(9)
Bayesian fraction fitting	3523(845)	49(12)	51(12)	0.037(10)

Table 6.8: Total reaction numbers, branching ratios, and resonance strength derived from the three methods of analysis. Branching ratios denoted by * are taken from [Wolke et al., 1989].

an effect on the traditional analysis, because the coincidence efficiency is constructed using the known primary branching ratios. However, [Wolke et al., 1989] showed that the 1809 keV secondary γ-ray is produced for 84 to 98% of decays in higher energy resonances in ^{22}Ne(α,γ)^{26}Mg. It is therefore reasonable to assume that the additions of unknown primary branches will not alter the traditional analysis significantly, but does appear to have a significant effect on the fraction fitting. The value officially reported in this dissertation is therefore

$$\omega\gamma = 0.047 \pm 0.012 \text{ meV} \tag{6.8}$$

The uncertainty of this measurement is a direct consequence of the low statistics of the data set. An extensive study of effects of these results on the cross section of the ^{22}Ne(α,γ)^{26}Mg, the subsequent effect on the ^{22}Ne(α,n)^{25}Mg reaction in stellar environments, and the effect on the weak and strong s-process are not explored in this dissertation.

6.8 Excitation Energy

An effort was also made to extract the excitation energy of the 828 keV resonance from the identified primary γ-rays. To do this with the data presented in Chapter 6, Equation C.11 from [Iliadis, 2015] was modified and used. The modified equation is:

$$E_\gamma = E_{x\ initial} - E_{x\ final} + \Delta E_{Dopp} - \Delta E_{rec} \tag{6.9}$$

Parameter	Value$_{9532(2)}$ (keV)	Value$_{4269(2)}$ (keV)
E_γ	9532(2)	4269(2)
$E_{x\ final}$	1809	7062
ΔE_{Dopp}	24	11
ΔE_{Rec}	2	0

Table 6.9: Parameters for calculating excitation energy using equation 6.9. The parameter E_γ was measured from the data spectrum, $E_{x\ final}$ was taken from [Endt, 1998], ΔE_{Dopp} is calculated in appendix A, and ΔE_{Rec} is calculated from equation 6.10.

where E_γ is the observed γ-ray energy, $E_{x\ initial}$ and $E_{x\ final}$ are the initial and final energy states respectively, and ΔE_{Dopp} and ΔE_{rec} are the Doppler shift and recoil energies respectively. The Doppler shift is calculated in Appendix A and shown in Table 6.9. The recoil energy (from Equation C.13 in [Iliadis, 2015] is given by

$$\Delta E_{rec} = 5.36772 \times \frac{E_\gamma^2}{M} \tag{6.10}$$

where E_γ is the energy of a primary in MeV, and M is the mass of the recoiling nucleus. Table 6.9 contains the parameters used in Equation 6.9 to calculate the excitation energy.

Using these values, and equation 6.9, the excitation energy value predicted for each of the primary γ-rays measured is:

$$E_{x,9532} = 11319(2)\text{keV} \tag{6.11}$$

$$E_{x,4269} = 11320(2)\text{keV} \tag{6.12}$$

These values are consistent with states identified in Table 6.1

Chapter 7

Conclusions

The goal of this dissertation has been to improve the technologies needed to remeasure the low energy resonances in the ^{22}Ne(α,γ)^{26}Mg and ^{22}Ne(α,n)^{25}Mg reactions and to attempt to remeasure the resonance strength of the 831 keV resonance in the ^{22}Ne(α,n)^{25}Mg reaction.

Efforts to characterize a new fast neutron spectrometer capable of differentiating between the low energy ($\approx$ 300 keV) neutrons from the ^{22}Ne(α,n)^{25}Mg reaction and the higher energy ($\approx$ 3 MeV) neutrons from the contaminant ^{13}C(α,n)^{16}O reaction were mostly successful. Analysis of the signals from the BC523A detector using pulse shape discrimination showed that the literature understanding of the detector was incorrect, the capture event signal was properly identified, and confirmed using gating and timing tests. The energy resolution of the detector was measured for the first time, using the neutron time-of-flight method, and showed that the detector would have good discrimination between signal and contaminant neutrons from the ^{22}Ne(α,n)^{25}Mg and ^{13}C(α,n)^{16}O reactions. Intrinsic efficiency as a function of energy was also measured for the first time, though the results of that measurement showed that the detector most likely had insufficient efficiency for use in this dissertation.

Targets were also designed that are capable of withstanding the intense damage of an α-particle beam. Three targets were explored, the first of which was made of a highly pure glass called fused silica. This target was blister-resistant, but did not have the mechanical strength desired for most nuclear targets, and had insufficient thermal conduction for proper cooling. The second target designed used sintered metal for the backing. This target was also blister resistant, but proved very difficult to water cool due to its porous

nature. The final target used evaporated titanium to develop a porous Stranski-Krastanov structure which proved blister resistant (possibly blister-proof) while still retaining the cooling properties associated with standard implanted solid targets. This dissertation represents the first ever measurement with such a target.

The loss of the implantation system needed to make additional targets (see Chapter 3) prevented all the data collection planned for this experiment, which resulted in poor statistics for the measurement of the resonance strength in ^{22}Ne(α,γ)^{26}Mg. Despite the poor statistics, a resonance strength measurement was still made, and the strength found disagrees with the only directly measured literature value.

Despite these low statistics, the preliminary results shown here may indicate that the strength of the 828 keV resonance in ^{22}Ne(α,γ)^{26}Mg is higher than the only other previous measurement of 0.036(4) meV by Wolke et al. [1989]. It is hypothesized here that the wide range of values for the resonance strength measured for the various resonances in ^{22}Ne(α,n)^{25}Mg (including the 831 keV resonance) by various groups (see Chapter 1) using the same extended gas cell target lend credibility to the target being one of the primary causes of potential systematic errors. The only direct measurement of the ^{22}Ne(α,γ)^{26}Mg reaction used the same gas cell target, leading to the hypothesis that the resonance strength measured by [Wolke et al., 1989] contains additional unaccounted for uncertainty. This work in this dissertation leads us to recommend additional data be collected for the 831 keV resonance using the evaporated porous targets detailed in Chapter 4 once a new implantation system for LENA is secured.

It should also be noted that LENA has procured funding for a new accelerator to replace the JN, which will be capable of providing a pulsed-mode α-particle beam to target with an effective current of 20 mA ($\approx$ 400 times greater than what was used for this study). The pulse capabilities of the new accelerator would prevent heat damage to the targets and only collecting data when the beam is on target will reduce background by a factor of $\approx$ 400. This would all but entirely eliminate background near the primary peaks of

interest and would vastly improve the uncertainty on the secondary peak.

Once an updated measurement of the resonance strength of the 828 keV resonance in the ^{22}Ne(α,γ)^{26}Mg reaction is performed, a thorough investigation of the effect of the new resonance strength on the s-process in the stellar environments of AGB and massive stars can be performed.

APPENDIX A: DOPPLER EFFECTS

The purpose of this appendix is to outline the efforts made to properly account for the Doppler shift and Doppler broadening of the primary peaks in the measurement made is Chapter 6. Much of the work shown here uses equations and formalisms from [Iliadis, 2015] and references within.

Doppler shift is a fairly straightforward calculation. From [Daigle et al., 2016], the Doppler shift can be represented by the equation:

$$E_{\gamma}^{obs} = E_{\gamma}^{0} \frac{\sqrt{1-\beta(t)^2}}{1-\beta(t)Q_1 \cos(\theta} \tag{7.1}$$

where E_{γ}^{obs} is the observed γ-ray energy, E_{γ}^{0} is the unshifted energy, $\beta(t)$ is the recoil velocity (in units of c), and Q_1 is an angular attenuation coefficient, which corrects for the angular acceptance of the detector.

The value used for Q_1 is 0.85 for the lower energy primary, and 0.86 for the higher energy primary (taken from [Dermigny, 2018]). The recoil velocity is found via the equation

$$v_B = v_a \frac{m_a}{m_B} \tag{7.2}$$

where v and m are velocity and mass respectively, and the subscripts refer to nuclei, best illustrated with Figure 7.1. For the 828 keV resonance, this becomes $v_B \approx 9 \times 10^5 m/s$. This gives a value of $\beta(t) \approx 0.003$. Using this, Equation 7.1 becomes:

$$E_{\gamma}^{obs} = E_{\gamma}^{0} \times 1.00255 \tag{7.3}$$

The values observed for the two primary γ-rays from the 828 keV resonance are 4269(2) keV and 9532(2) keV. This gives actual emitted γ-ray values of 4258(2) keV and 9508(2) keV. These Doppler shifts were applied to the templates used in the fraction fitting analysis method.

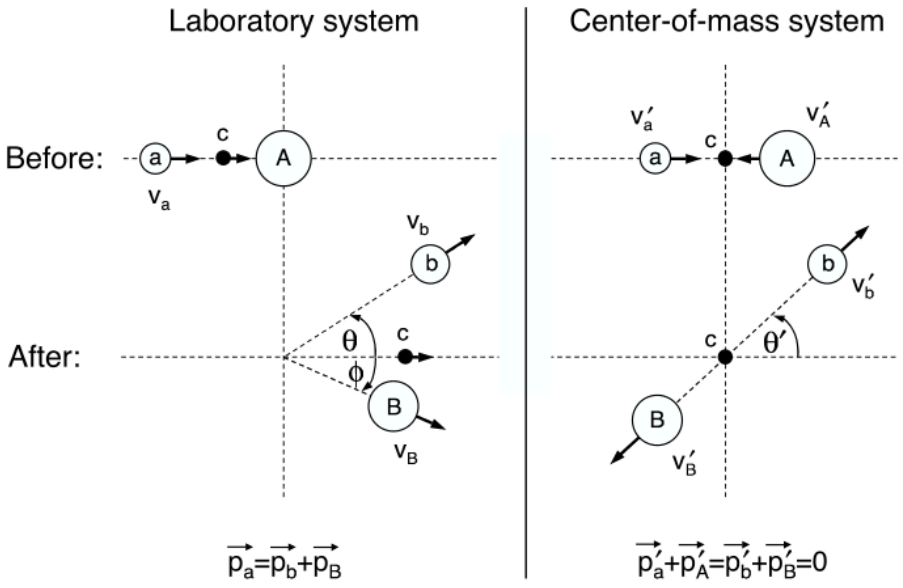

Figure 7.1: kinematic properties of a reaction $A(a,b)B$ in the laboratory frame (a), and the center-of-mass frame (b). Figure taken from [Iliadis, 2015].

Doppler broadening of the peaks is caused by the fact that γ-rays with different values of θ have a different energies, which will increase the FHWM of peaks within a measured spectra. To determine the Doppler broadening of the peaks in the ^{22}Ne(α,γ)^{26}Mg, we will compare to the broadening in the ^{22}Ne(p,γ)^{23}Na reaction.

First, it is necessary to attempt to approximate the Doppler broadening of peak within the ^{22}Ne(p,γ)^{23}Na spectra. The 9252 keV γ-ray was chosen for this, FWHM of the γ-ray was measured using `JAM` to be 14.49 keV. The energy resolution of the HPGe detector at these energies is $\approx$ 13 keV. The Doppler shift and energy resolution of the detector are added in quadrature to obtain the observed FWHM

$$FWHM_{total} = \sqrt{(FWHM_{Reso})^2 + (FWHM_{Dopp})^2} \tag{7.4}$$

Using the measured values, a Doppler broadening of $\approx$ 6 keV is obtained.

The maximum angle of acceptance into the detector of 1.22 radians (taken from `Geant4` simulations). An estimate of the maximum possible Doppler broadening is made by comparing the difference between the Doppler shifts at 1.22 and 0 radians. Using Equation

7.1, the values for maximum broadening value for the 9252 keV γ-ray from ^{22}Ne(p,γ)^{23}Na reaction of $\approx$ 8 keV. Repeating for the ^{22}Ne(α,γ)^{26}Mg reaction yields a maximum broadening value of $\approx$ 19 keV.

The approximation for Doppler broadening requires a link between the measured broadening for the ^{22}Ne(p,γ)^{23}Na reaction, and the expected Doppler broadening for the ^{22}Ne(α,γ)^{26}Mg reaction. The link chosen for this approximation is the ratio of observed broadening to the maximum possible broadening. For the 9252 keV γ-ray from ^{22}Ne(p,γ)^{23}N reaction, this ratio is $\approx 3/4$. Applying this to the 19 keV maximum possible broadening for the 9504 keV γ-ray from ^{22}Ne(α,γ) reaction results in a Doppler broadening value of $\approx$ 14 keV.

Multiplying this ratio to the 8 keV maximum possible broadening for the 4252 keV γ-ray from ^{22}Ne(α,γ) reaction results in a Doppler broadening value:

$$\Delta_{broadening,4252} \approx 6 \text{ keV} \tag{7.5}$$

The energy resolution for the HPGe detector at this energy is $\approx$ 8 keV (see Figure 5.4). To include Doppler broadening in the Geant4 simulations used in fraction fitting, the Doppler broadening and energy resolution were added in quadrature, and normalized to the existing energy resolution in Geant, yielding a correction of

$$\sigma_{new,4252} = 1.25\sigma_{old} \tag{7.6}$$

Applying this to the 19 keV maximum possible broadening for the 9504 keV γ-ray from the ^{22}Ne(α,γ)^{26}Mg reaction results in a Doppler broadening value:

$$\Delta_{broadening,9504} \approx 14 \text{ keV} \tag{7.7}$$

The energy resolution for the HPGe detector at this energy is $\approx$ 13 keV (see Chapter 5). To include Doppler broadening in the Geant4 simulations used in fraction fitting, the

Doppler and energy resolution were added in quadrature, and normalized to the existing energy resolution in Geant, yielding a correction of

$$\sigma_{new,9504} = 1.37\sigma_{old} \tag{7.8}$$

APPENDIX B: EXCITATION ENERGIES

The excitation energy quoted in this dissertation comes from the only direct measurement of the ^{22}Ne(α,γ)^{26}Mg reaction [Wolke et al., 1989]. The excitation energy is not explicitly stated in Wolke's work, so it was extracted from his measured resonance energy via the equation given in [Kikstra et al., 1990]

$$E_x = Q + \frac{m_T}{m_T + m_\alpha} E_\alpha \frac{2}{1 + \sqrt{1 + 2E_\alpha m_T/(m_T + m_\alpha)^2 c^2}} \tag{7.9}$$

where E_x is the excitation energy, E_α is the bombarding particle energy, Q is the Q value for the reaction, and m_T and m_α are the masses of the target and bombarding particle respectively. These values are given in Table 7.1

These values result in an excitation energy of: 11313(4) keV

Parameter	Value
E_α	828(5) keV
Q	10612.88(3) keV
m_t	21.9914
m_α	4.0026

Table 7.1: Parameters for calculating excitation energy from [Wolke et al., 1989]. The Q is calculated from atomic mass differences, accounting for the difference in electron binding energy. All masses are taken from [Wang et al., 2017].

APPENDIX C: BRANCHING RATIOS

Table of branching ratios adopted from [Kelly, 2016].

Initial state (MeV)	Final state (MeV)	Branching ratio	Branch uncertainty
0.44	0.00	1.000	0.000
2.08	0.44	0.918	0.046
2.08	0.00	0.082	0.004
2.39	0.44	0.343	0.017
2.39	0.00	0.657	0.033
2.64	0.00	1.000	0.000
2.98	2.39	0.003	0.0001
2.98	0.44	0.411	0.021
2.98	0.00	0.586	0.029
3.68	2.89	0.005	0.001
3.68	2.64	0.195	0.010
3.68	2.39	0.013	0.0001
3.68	0.44	0.787	0.039
3.85	2.98	0.020	0.001
3.85	2.64	0.045	0.002
3.85	2.08	0.611	0.031
3.85	0.44	0.095	0.005
3.85	0.00	0.229	0.011
3.91	2.98	0.023	0.001
3.91	2.39	0.011	0.001
3.91	2.08	0.090	0.004
3.91	0.44	0.081	0.004
3.91	0.00	0.795	0.040
4.43	2.39	0.083	0.004
4.43	0.00	0.917	0.046
5.77	3.85	0.015	0.001
5.77	2.64	0.045	0.002
5.77	0.44	0.421	0.021
5.77	0.00	0.520	0.026
6.92	0.44	0.301	0.015
6.92	0.00	0.699	0.035
7.08	0.00	0.550	0.020
7.08	0.44	0.250	0.030
7.08	2.64	0.200	0.020
9.25	7.08	0.021	0.001
9.25	6.92	0.024	0.001
9.25	5.77	0.028	0.001
9.25	4.43	0.017	0.001
9.25	3.91	0.004	0.001
9.25	3.68	0.049	0.002
9.25	2.98	0.317	0.005
9.25	2.64	0.083	0.002
9.25	2.39	0.041	0.001
9.25	0.00	0.418	0.007

Table 7.2: Branching ratios of the 479 keV resonance in ^{22}Ne(p,γ)^{23}Na. Values are taken from [Kelly, 2016] and references within.

BIBLIOGRAPHY

P Adsley, JW Brümmer, T Faestermann, SP Fox, F Hammache, R Hertenberger, A Meyer, R Neveling, D Seiler, N de Séréville, et al. High-resolution study of levels in the astrophysically important nucleus mg 26 and resulting updated level assignments. *Physical Review C*, 97(4):045807, 2018.

Sea Agostinelli, John Allison, K al Amako, J Apostolakis, H Araujo, P Arce, M Asai, D Axen, S Banerjee, G Barrand, et al. Geant4, a simulation toolkit. *Nuclear Instruments and Methods in Physics research section A: Accelerators, Spectrometers, Detectors and Associated Equipment*, 506(3):250–303, 2003.

John Allison, K Amako, J Apostolakis, HAAH Araujo, P Arce Dubois, MAAM Asai, GABG Barrand, RACR Capra, SACS Chauvie, RACR Chytracek, et al. Geant4 developments and applications. *Nuclear Science, IEEE Transactions on*, 53(1):270–278, 2006.

WD Arnett and F-K Thielemann. Hydrostatic nucleosynthesis. i-core helium and carbon burning. *The Astrophysical Journal*, 295:589–619, 1985.

WD Arnett and JW Truran. Carbon-burning nucleosynthesis at constant temperature. *The Astrophysical Journal*, 157:339, 1969.

Charles William Arnold. *A New Absolute Total Cross-Section for Photodisintegration of Beryllium-9*. PhD thesis, The University of North Carolina at Chapel Hill, 2011.

CW Arnold, TB Clegg, HJ Karwowski, GC Rich, JR Tompkins, and CR Howell. Characterization of an invs model iv neutron counter for high precision (γ, n) cross-section measurements. *Nuclear Instruments and Methods in Physics Research Section A: Accelerators, Spectrometers, Detectors and Associated Equipment*, 647(1):55–62, 2011.

Marcel Arnould and Stéphane Goriely. The p-process of stellar nucleosynthesis: astrophysics and nuclear physics status. *Physics Reports*, 384(1):1–84, 2003.

G Audi, AH Wapstra, and C Thibault. The ame2003 atomic mass evaluation:(ii). tables, graphs and references. *Nuclear Physics A*, 729(1):337–676, 2003.

K Banerjee, TK Ghosh, S Kundu, TK Rana, C Bhattacharya, JK Meena, G Mukherjee, P Mali, Dhruba Gupta, S Mukhopadhyay, et al. Variation of neutron detection characteristics with dimension of bc501a neutron detector. *Nuclear Instruments and Methods in Physics Research Section A: Accelerators, Spectrometers, Detectors and Associated Equipment*, 608(3):440–446, 2009.

Roger Barlow. Extended maximum likelihood. *Nuclear Instruments and Methods in Physics Research Section A: Accelerators, Spectrometers, Detectors and Associated Equipment*, 297(3): 496–506, 1990.

Roger Barlow and Christine Beeston. Fitting using finite monte carlo samples. *Computer Physics Communications*, 77(2):219–228, 1993.

Allan FM Barton. *CRC handbook of solubility parameters and other cohesion parameters*. CRC press, 1991.

Ernst Bauer. Phänomenologische theorie der kristallabscheidung an oberflächen. ii. *Zeitschrift für Kristallographie-Crystalline Materials*, 110(1-6):395–431, 1958.

PM Bird and PRJ Burch. The relative performances of large volume plastic and liquid scintillators. *Physics in Medicine and Biology*, 2(3):217, 1958.

JC Browne and BL Berman. Neutron-capture cross sections for osmium isotopes and the age of the universe. *Physical Review C*, 23(4):1434, 1981.

Matthew Quinn Buckner. *Hydrogen burning of the rare oxygen isotopes*. PhD thesis, The University of North Carolina at Chapel Hill, 2014.

E Margaret Burbidge, Geoffrey Ronald Burbidge, William A Fowler, and Fred Hoyle. Synthesis of the elements in stars. *Reviews of Modern Physics*, 29(4):547, 1957.

DF Buscher, JE Baldwin, PJ Warner, and CA Haniff. Detection of a bright feature on the surface of betelgeuse. *Monthly Notices of the Royal Astronomical Society*, 245:7P–11P, 1990.

M Busso, R Gallino, and GJ Wasserburg. Nucleosynthesis in asymptotic giant branch stars: Relevance for galactic enrichment and solar system formation. *Annual Review of Astronomy and Astrophysics*, 37(1):239–309, 1999.

Kaiyong Cai, Michael Müller, Jörg Bossert, Annett Rechtenbach, and Klaus D Jandt. Surface structure and composition of flat titanium thin films as a function of film thickness and evaporation rate. *Applied Surface Science*, 250(1-4):252–267, 2005.

AGW Cameron. Essays in nuclear astrophysics, ed. *C. Barnes, D. Clayton, and D*, 1982.

Alastair Graham Walter Cameron. Stellar evolution, nuclear astrophysics, and nucleogenesis. Technical report, Atomic Energy of Canada Ltd. Chalk River Project, Chalk River, Ontario (Canada), 1957.

Spencer Carson, Christian Iliadis, John Cesaratto, Art Champagne, Lori Downen, Marija Ivanovic, John Kelley, Richard Longland, Joseph R Newton, Gencho Rusev, et al. Ratio of germanium detector peak efficiencies at photon energies of 4.4 and 11.7 mev: Experiment versus simulation. *Nuclear Instruments and Methods in Physics Research Section A: Accelerators, Spectrometers, Detectors and Associated Equipment*, 618(1):190–198, 2010.

MB Chadwick, P Obložinskỳ, M Herman, NM Greene, RD McKnight, DL Smith, PG Young, RE MacFarlane, GM Hale, SC Frankle, et al. Endf/b-vii. 0: Next generation evaluated nuclear data library for nuclear science and technology. *Nuclear Data Sheets*, 107(12):2931–3060, 2006.

A Chieffi and M Limongi. The production of 26 al, 60 fe and 44 ti in massive stars of solar metallicity. *New Astronomy Reviews*, 46(8):459–462, 2002.

Donald D Clayton and ME Rassbach. Termination of the s-process. *The Astrophysical Journal*, 148:69, 1967.

Donald D Clayton and Richard A Ward. S-process studies: Exact evaluation of an exponential distribution of exposures. *The Astrophysical Journal*, 193:397–400, 1974.

Donald D Clayton, William A Fowler, TE Hull, and BA Zimmerman. Neutron capture chains in heavy element synthesis. *Annals of Physics*, 12(3):331–408, 1961.

AC Comrie, A Buffler, FD Smit, and HJ Wörtche. Digital neutron/gamma discrimination with an organic scintillator at energies between 1mev and 100mev. *Nuclear Instruments and Methods in Physics Research Section A: Accelerators, Spectrometers, Detectors and Associated Equipment*, 772:43–49, 2015.

Andrew L Cooper, KJ Kelly, E Machado, I Pogrebnyak, J Surbrook, C Tysor, P Thompson, M Emamian, B Walsh, B Carlin, et al. Development of a variable-energy, high-intensity, pulsed-mode ion source for low-energy nuclear astrophysics studies. *Review of Scientific Instruments*, 89(8):083301, 2018.

Richard G Couch, Ann B Schmiedekamp, and W David Arnett. s-process nucleosynthesis in massive stars: core helium burning. *The Astrophysical Journal*, 190:95–100, 1974.

John J Cowan, Friedrich-Karl Thielemann, and James W Truran. Radioactive dating of the elements. *Annual Review of Astronomy and Astrophysics*, 29:447–497, 1991.

S Daigle, KJ Kelly, AE Champagne, MQ Buckner, C Iliadis, and C Howard. Measurement of the e r c. m.= 259 kev resonance in the n 14 (p, γ) o 15 reaction. *Physical Review C*, 94 (2):025803, 2016.

John Robert Dermigny. *Investigation of the 30Si(p,y)31P reaction*. PhD thesis, The University of North Carolina at Chapel Hill, 2018.

JR Dermigny, C Iliadis, MQ Buckner, and KJ Kelly. γ-ray spectroscopy using a binned likelihood approach. *Nuclear Instruments and Methods in Physics Research Section A: Accelerators, Spectrometers, Detectors and Associated Equipment*, 830:427–437, 2016.

HW Drotleff, A Denker, H Knee, M Soine, G Wolf, JW Hammer, U Greife, C Rolfs, and HP Trautvetter. Reaction rates of the s-process neutron sources 22ne (α, n) 25mg and 13c (α, n) 16o. *The Astrophysical Journal*, 414(2):735–739, 1993.

PM Endt. Supplement to energy levels of a= 21–44 nuclei (vii). *Nuclear Physics A*, 633(1): 1–220, 1998.

SK Erents and GM McCracken. Blistering of molybdenum under helium ion bombardment. *Radiation Effects*, 18(3-4):191–198, 1973.

JH Evans. An interbubble fracture mechanism of blister formation on helium-irradiated metals. *Journal of Nuclear Materials*, 68(2):129–140, 1977.

JH Evans. The role of implanted gas and lateral stress in blister formation mechanisms. *Journal of Nuclear Materials*, 76:228–234, 1978.

Marcio Luis Ferreira Nascimento and Edgar Dutra Zanotto. Diffusion processes in vitreous silica revisited. *Physics and Chemistry of Glasses-European Journal of Glass Science and Technology Part B*, 48(4):201–217, 2007.

M Flaska and SA Pozzi. Identification of shielded neutron sources with the liquid scintillator bc-501a using a digital pulse shape discrimination method. *Nuclear Instruments and Methods in Physics Research Section A: Accelerators, Spectrometers, Detectors and Associated Equipment*, 577(3):654–663, 2007.

Marek Flaska and Sara A Pozzi. Digital pulse shape analysis for the capture-gated liquid scintillator bc-523a. *Nuclear Instruments and Methods in Physics Research Section A: Accelerators, Spectrometers, Detectors and Associated Equipment*, 599(2):221–225, 2009.

J Frehaut. Use of the large gadolinium-loaded liquid scintillator technique for (n, 2n) and (n, 3n) cross section measurements. *Nuclear Instruments and Methods*, 135(3):511–518, 1976.

DA García-Hernández, Plez García-Lario, Bertrand Plez, F D'antona, A Manchado, and JM Trigo-Rodríguez. Rubidium-rich asymptotic giant branch stars. *Science*, 314(5806): 1751–1754, 2006.

DA García-Hernández, Arturo Manchado, David L Lambert, Bertrand Plez, Pedro Garcia-Lario, Francesca D'Antona, Maria Lugaro, AI Karakas, and MA Van Raai. Rb-rich asymptotic giant branch stars in the magellanic clouds. *The Astrophysical Journal Letters*, 705(1):L31, 2009.

U Giesen, CP Browne, J Görres, S Graff, C Iliadis, H-P Trautvetter, M Wiescher, W Harms, KL Kratz, B Pfeiffer, et al. The astrophysical implications of low-energy resonances in 22 ne+ α. *Nuclear Physics A*, 561(1):95–111, 1993.

LL Green, GA Stephens, and JC Willmott. The 7li (α, γ) 11b reaction. *Proceedings of the Physical Society*, 79(5):1017, 1962.

LR Greenwood and NR Chellew. Improved 10b-loaded liquid scintillator with pulse-shape discrimination. *Review of Scientific Instruments*, 50(4):466–471, 1979.

LR Greenwood, NR Chellew, and GA Zarwell. 6li-loaded liquid scintillators with pulse shape discrimination. *Review of Scientific Instruments*, 50(4):472–477, 1979.

KL Hainebach and DN Schramm. Galactic evolution models and the rhenium-187/osmium-187 chronometer-a greater age for the galaxy. *The Astrophysical Journal*, 207:L79–L82, 1976.

G Hardie, BW Filippone, AJ Elwyn, M Wiescher, and RE Segel. Resonant alpha capture by be 7 and li 7. *Physical Review C*, 29(4):1199, 1984.

V Harms, K-L Kratz, and M Wiescher. Properties of ne 22 (α, n) 25 mg resonances. *Physical Review C*, 43(6):2849, 1991.

Graham M Harper, Alexander Brown, and Edward F Guinan. A new vla-hipparcos distance to betelgeuse and its implications. *The Astronomical Journal*, 135(4):1430, 2008.

X Haubois, G Perrin, S Lacour, Tijl Verhoelst, S Meimon, L Mugnier, E Thiébaut, JP Berger, ST Ridgway, JD Monnier, et al. Imaging the spotty surface of betelgeuse in the h band. *Astronomy & Astrophysics*, 508(2):923–932, 2009.

Falk Herwig. Evolution and yields of extremely metal-poor intermediate-mass stars. *The Astrophysical Journal Supplement Series*, 155(2):651, 2004.

Dorrit Hoffleit. History of the discovery of mira stars. *Journal of the American Association of Variable Star Observers (JAAVSO)*, 25:115–136, 1997.

K Hofmann, B Spangenberg, M Luysberg, and H Kurz. Properties of evaporated titanium thin films and their possible application in single electron devices. *Thin Solid Films*, 436 (2):168–174, 2003.

C Howard, C Iliadis, and AE Champagne. Monte carlo simulation of the lena detector system. *Nuclear Instruments and Methods in Physics Research Section A: Accelerators, Spectrometers, Detectors and Associated Equipment*, 729:254–259, 2013.

S Hunt, C Iliadis, and R Longland. Characterization of a 10 b-doped liquid scintillator as a capture-gated neutron spectrometer. *Nuclear Instruments and Methods in Physics Research Section A: Accelerators, Spectrometers, Detectors and Associated Equipment*, 811: 108–114, 2016.

Sean Hunt, Camden Hunt, Christian Iliadis, and Michael Falvo. Blister resistant targets for nuclear reaction experiments with α-particle beams. *Nuclear Instruments and Methods in Physics Research Section A: Accelerators, Spectrometers, Detectors and Associated Equipment*, 2018.

Icko Iben Jr and Alvio Renzini. Asymptotic giant branch evolution and beyond. *Annual Review of Astronomy and Astrophysics*, 21:271–342, 1983.

C Iliadis. Nuclear physics of stars, by christian iliadis. Technical report, ISBN 978-3-527-40602-9. Published by Wiley-VCH Verlag, Wenheim, Germany, 2007.

Christian Iliadis. *Nuclear Physics of Stars 2nd Edition*. John Wiley & Sons, 2015.

Christian Iliadis, Richard Longland, AE Champagne, Alain Coc, and Ryan Fitzgerald. Charged-particle thermonuclear reaction rates: Ii. tables and graphs of reaction rates and probability density functions. *Nuclear Physics A*, 841(1-4):31–250, 2010.

M Jaeger, R Kunz, A Mayer, JW Hammer, G Staudt, KL Kratz, and B Pfeiffer. N 22 e (α, n) m 25 g: The key neutron source in massive stars. *Physical Review Letters*, 87(20):202501, 2001.

F James. F. james and m. roos, comput. phys. commun. 10, 343 (1975). *Comput. Phys. Commun.*, 10:343, 1975.

J Januszewski, MI Khokhar, and AS Mujumdar. Thermal conductivity of some porous metals. *Letters in Heat and Mass Transfer*, 4(6):417–423, 1977.

SD Jastaniah and PJ Sellin. Digital techniques for n/γ pulse shape discrimination and capture-gated neutron spectroscopy using liquid scintillators. *Nuclear Instruments and Methods in Physics Research Section A: Accelerators, Spectrometers, Detectors and Associated Equipment*, 517(1):202–210, 2004.

PB Johnson, RW Thomson, and Karen Reader. Tem and sem studies of radiation blistering in helium-implanted copper. *Journal of Nuclear Materials*, 273(2):117–129, 1999.

M Kaminsky and SK Das. Effect of temperature on first-wall erosion by radiation blistering. *Nuclear Technology*, 22(3):373–378, 1974.

F Kappeler, H Beer, and K Wisshak. S-process nucleosynthesis-nuclear physics and the classical model. *Reports on Progress in Physics*, 52(8):945, 1989.

Franz Käppeler, Roberto Gallino, Sara Bisterzo, and Wako Aoki. The s process: Nuclear physics, stellar models, and observations. *Reviews of Modern Physics*, 83(1):157, 2011.

AI Karakas, Maria A Lugaro, Michael Wiescher, J Görres, and Claudio Ugalde. The uncertainties in the 22ne+ α-capture reaction rates and the production of the heavy magnesium isotopes in asymptotic giant branch stars of intermediate mass. *The Astrophysical Journal*, 643(1):471, 2006.

Amanda I Karakas, DA García-Hernández, and Maria Lugaro. Heavy element nucleosynthesis in the brightest galactic asymptotic giant branch stars. *The Astrophysical Journal*, 751(1):8, 2012.

Margarita Karovska, Warren Hack, John Raymond, and Edward Guinan. First hubble space telescope observations of mira ab wind-accreting binary system. *The Astrophysical Journal Letters*, 482(2):L175, 1997.

Keegan John Kelly. *Nuclear reaction rate uncertainties and the 22 Ne (p, γ) 23 Na reaction: Classical novae and globular clusters*. PhD thesis, The University of North Carolina at Chapel Hill, 2016.

SW Kikstra, C Van Der Leun, PM Endt, JGL Booten, AGM Van Hees, and AA Wolters. The 40ca level scheme investigated with the 39k (p, γ) 40ca reaction. *Nuclear Physics A*, 512(3):425–465, 1990.

PE Koehler. Constraints on the 22 ne (α, n) 25 mg s-process neutron source from analysis of nat mg+ n total and 25 mg (n, γ) cross sections. *Physical Review C*, 66(5):055805, 2002.

VI Kononenko, VM Baranovskii, and VP Dushchenko. Thermal conductivity of porous sintered iron. *Powder Metallurgy and Metal Ceramics*, 7(3):175–177, 1968.

SA Lamb, WM Howard, JW Truran, and I Iben Jr. Neutron-capture nucleosynthesis in the helium-burning cores of massive stars. *The Astrophysical Journal*, 217:213–221, 1977.

L Lebreton, A Zimbal, and D Thomas. Experimental comparison of 241am–be neutron fluence energy distributions. *Radiation Protection Dosimetry*, 2007.

RW Lee, RC Frank, and DE Swets. Diffusion of hydrogen and deuterium in fused quartz. *The Journal of Chemical Physics*, 36(4):1062–1071, 1962.

Lu Lin, RM Dreizler, and H Galbraith. Spontaneous-fission half-life of 8 be. *Lettere Al Nuovo Cimento (1971–1985)*, 11(14):627–630, 1974.

R Longland, C Iliadis, AE Champagne, C Fox, and JR Newton. Nuclear astrophysics studies at the lena facility: The γ-ray detection system. *Nuclear Instruments and Methods in Physics Research Section A: Accelerators, Spectrometers, Detectors and Associated Equipment*, 566(2):452–464, 2006.

R Longland, C Iliadis, JM Cesaratto, AE Champagne, S Daigle, Joseph R Newton, and R Fitzgerald. Resonance strength in ne 22 (p, γ) na 23 from depth profiling in aluminum. *Physical Review C*, 81(5):055804, 2010a.

Richard Longland, Christian Iliadis, AE Champagne, JR Newton, Claudio Ugalde, Alain Coc, and Ryan Fitzgerald. Charged-particle thermonuclear reaction rates: I. monte carlo method and statistical distributions. *Nuclear Physics A*, 841(1):1–30, 2010b.

Richard Longland, Christian Iliadis, and Amanda I Karakas. Reaction rates for the s-process neutron source 22 ne+ α. *Physical Review C*, 85(6):065809, 2012.

M Lugaro and M van Raai. New discoveries and challenges for the s process in agb stars. *Journal of Physics G: Nuclear and Particle Physics*, 35(1):014007, 2007.

LK Mansur and WA Coghlan. Mechanisms of helium interactions with radiation effects in metals and alloys: A review. *Journal of Nuclear Materials*, 119(1):1–25, 1983.

N Marochov and PJ Goodhew. A comparison of the growth of helium and neon bubbles in nickel. *Journal of Nuclear Materials*, 158:81–86, 1988.

Joseph S Masaryk and Richard M Fulrath. Diffusivity of helium in fused silica. *The Journal of Chemical Physics*, 59(3):1198–1202, 1973.

Cristian Massimi, Sebastian Altstadt, Józef Andrzejewski, L Audouin, M Barbagallo, Vicente Bécares, F Bečvář, F Belloni, E Berthoumieux, J Billowes, et al. Neutron spectroscopy of 26mg states: Constraining the stellar neutron source 22ne (α, n) 25mg. *Physics Letters B*, 768:1–6, 2017.

Hj Matzke and E Vernaz. Thermal and physicochemical properties important for the long term behavior of nuclear waste glasses. *Journal of Nuclear Materials*, 201:295–309, 1993.

Albert Miller. Californium-252 as a neutron source for bnct. In *Neutron Capture Therapy*, pages 69–74. Springer, 2012.

IA Pawełczak, J Tõke, E Henry, M Quinlan, H Singh, and WU Schröder. Nstara capture gated plastic neutron detector. *Nuclear Instruments and Methods in Physics Research Section A: Accelerators, Spectrometers, Detectors and Associated Equipment*, 629(1):230–238, 2011.

Paolo Peerani, Alice Tomanin, Sara Pozzi, Jennifer Dolan, Eric Miller, Marek Flaska, Marco Battaglieri, Raffaella De Vita, Luisa Ficini, Giacomo Ottonello, et al. Testing on novel neutron detectors as alternative to 3 he for security applications. *Nuclear Instruments and Methods in Physics Research Section A: Accelerators, Spectrometers, Detectors and Associated Equipment*, 696:110–120, 2012.

DB Pellowitz. Mcnpx users manual, version 2.6. 0. *Los Alamos Report No. LA CP*, 2:408, 2007.

James G Peters. Nucleosynthesis by the s-process in stars of 9 and 15 solar masses. *The Astrophysical Journal*, 154:225, 1968.

M Pignatari, R Gallino, F Käppeler, and M Wiescher. Effects of uncertainties of the 22 ne (α, n) 25 mg and 13 c (α, n) 16 o reaction rates in the s-process yields. *Nuclear Physics A*, 758:541–544, 2005.

M Pignatari, R Gallino, M Heil, M Wiescher, F Käppeler, F Herwig, and S Bisterzo. The weak s-process in massive stars and its dependence on the neutron capture cross sections. *The Astrophysical Journal*, 710(2):1557, 2010.

F Pino, L Stevanato, D Cester, G Nebbia, L Sajo-Bohus, and G Viesti. Detecting fast and thermal neutrons with a boron loaded liquid scintillator, ej-339a. *Applied Radiation and Isotopes*, 92:6–11, 2014.

Anthony L Piro and Lars Bildsten. Neutronization during type ia supernova simmering. *The Astrophysical Journal*, 673(2):1009, 2008.

Antonio Pizzi and Kashmiri L Mittal. *Handbook of adhesive technology, revised and expanded*. CRC Press, 2003.

Richard F Post. Decay time and efficiency of a liquid scintillator. *Physical Review*, 79(4): 735, 1950.

N Prantzos, M Hashimoto, and K Nomoto. The s-process in massive stars-yields as a function of stellar mass and metallicity. *Astronomy and Astrophysics*, 234:211–229, 1990.

CM Raiteri, M Busso, G Picchio, and R Gallino. S-process nucleosynthesis in massive stars and the weak component. ii-carbon burning and galactic enrichment. *The Astrophysical Journal*, 371:665–672, 1991.

M Rayet, M Arnould, M Hashimoto, N Prantzos, and K Nomoto. The p-process in type ii supernovae. *Astronomy and Astrophysics*, 298:517, 1995.

R Reifarth, C Lederer, and F Käppeler. Neutron reactions in astrophysics. *Journal of Physics G: Nuclear and Particle Physics*, 41(5):053101, 2014.

Claus E Rolfs and William S Rodney. *Cauldrons in the cosmos: nuclear astrophysics*. University of Chicago press, 1988.

C Rowland, C Iliadis, AE Champagne, AK Dummer, R Fitzgerald, ECT Harley, J Mosher, and R Runkle. Studies of weak capture-γ-ray resonances via coincidence techniques. *Nuclear Instruments and Methods in Physics Research Section A: Accelerators, Spectrometers, Detectors and Associated Equipment*, 480(2):610–625, 2002.

Anne L Sallaska, Christian Iliadis, AE Champange, Stéphane Goriely, S Starrfield, and FX Timmes. Starlib: a next-generation reaction-rate library for nuclear astrophysics. *The Astrophysical Journal Supplement Series*, 207(1):18, 2013.

Philip A Seeger, William A Fowler, and Donald D Clayton. Nucleosynthesis of heavy elements by neutron capture. *The Astrophysical Journal Supplement Series*, 11:121, 1965.

Christopher Sneden and John J Cowan. Genesis of the heaviest elements in the milky way galaxy. *Science*, 299(5603):70–75, 2003.

Christopher Sneden, John J Cowan, and Roberto Gallino. Neutron-capture elements in the early galaxy. *Annu. Rev. Astron. Astrophys.*, 46:241–288, 2008.

JL Sokoloski and Lars Bildsten. Evidence for the white dwarf nature of mira b. *The Astrophysical Journal*, 723(2):1188, 2010.

Oscar Straniero, Roberto Gallino, and Sergio Cristallo. s process in low-mass asymptotic giant branch stars. *Nuclear Physics A*, 777:311–339, 2006.

Ivan N Stranski and Lubomir Krastanow. Zur theorie der orientierten ausscheidung von ionenkristallen aufeinander. *Monatshefte für Chemie und verwandte Teile anderer Wissenschaften*, 71(1):351–364, 1937.

Li Sun, Chia-Ling Chien, and Peter C Searson. Fabrication of nanoporous nickel by electrochemical dealloying. *Chemistry of Materials*, 16(16):3125–3129, 2004.

Kenneth B Swartz, Dale W Visser, and John M Baris. A java-based data acquisition system for nuclear physics. *Nuclear Instruments and Methods in Physics Research Section A: Accelerators, Spectrometers, Detectors and Associated Equipment*, 463(1):354–360, 2001.

DE Swets, RW Lee, and RC Frank. Diffusion coefficients of helium in fused quartz. *The Journal of Chemical Physics*, 34(1):17–22, 1961.

L Swiderski, M Moszynski, D Wolski, T Batsch, A Nassalski, A Syntfeld-Kazuch, T Szczesniak, F Kniest, MR Kusner, G Pausch, et al. Boron-10 loaded bc523a liquid scintillator for neutron detection in the border monitoring. *Nuclear Science, IEEE Transactions on*, 55 (6):3710–3716, 2008.

Tomasz Szczesniak, Marek Moszynski, Agnieszka Syntfeld-Kazuch, Lukasz Swiderski, Dariusz Wolski, Martyna Grodzicka, Guntram Pausch, Juergen Robert Stein, Frans Kniest, MR Kusner, et al. Light pulse shapes in liquid scintillators originating from gamma-rays and neutrons. *Nuclear Science, IEEE Transactions on*, 57(6):3846–3852, 2010.

R Talwar, T Adachi, GPA Berg, L Bin, S Bisterzo, M Couder, X Fang, H Fujita, Y Fujita, J Görres, et al. Probing astrophysically important states in the mg 26 nucleus to study neutron sources for the s process. *Physical Review C*, 93(5):055803, 2016.

F-K Thielemann, A Arcones, R Käppeli, M Liebendörfer, T Rauscher, C Winteler, C Fröhlich, I Dillmann, T Fischer, G Martinez-Pinedo, et al. What are the astrophysical sites for the r-process and the production of heavy elements? *Progress in Particle and Nuclear Physics*, 66(2):346–353, 2011.

Frank X Timmes, Edward F Brown, and JW Truran. On variations in the peak luminosity of type ia supernovae. *The Astrophysical Journal Letters*, 590(2):L83, 2003.

Claudia Travaglio, Roberto Gallino, Enrico Arnone, John Cowan, Faith Jordan, and Christopher Sneden. Galactic evolution of sr, y, and zr: a multiplicity of nucleosynthetic processes. *The Astrophysical Journal*, 601(2):864, 2004.

H Trinkaus. Energetics and formation kinetics of helium bubbles in metals. *Radiation Effects*, 78(1-4):189–211, 1983.

MY Tsai, BG Streetman, RJ Blattner, and CA Evans. Study of surface contamination produced during high dose ion implantation. *Journal of The Electrochemical Society*, 126(1): 98–102, 1979.

Roeland P van der Marel, Joris Gerssen, Puragra Guhathakurta, Ruth C Peterson, and Karl Gebhardt. Hubble space telescope evidence for an intermediate-mass black hole in the globular cluster m15. i. stis spectroscopy and wfpc2 photometrybased on observations with the nasa/esa hubble space telescope. *The Astronomical Journal*, 124(6):3255, 2002.

A Van Veen, W Th M Buters, TR Armstrong, B Nielsen, KT Westerduin, LM Caspers, and J Th M De Hosson. Redistribution of implanted noble gas atoms by self-interstitials in molybdenum and nickel. *Nuclear Instruments and Methods in Physics Research*, 209: 1055–1061, 1983.

DA Vermilyea. The kinetics of formation and structure of anodic oxide films on tantalum. *Acta Metallurgica*, 1(3):282–294, 1953.

F Voorhees, J Flamenbaum, and P Schultz. Method for producing high quality fused silica, April 23 1974. US Patent 3,806,570.

Lei Wang and T John Balk. Synthesis of nanoporous nickel thin films from various precursors. *Philosophical Magazine Letters*, 94(9):573–581, 2014.

Meng Wang, G Audi, FG Kondev, WJ Huang, S Naimi, and Xing Xu. The ame2016 atomic mass evaluation (ii). tables, graphs and references. *Chinese Physics C*, 41(3):030003, 2017.

Laurie S Waters, Gregg W McKinney, Joe W Durkee, Michael L Fensin, John S Hendricks, Michael R James, Russell C Johns, and Denise B Pelowitz. The mcnpx monte carlo radiation transport code. In *Hadronic Shower Simulation Workshop(AIP Conference Proceedings Volume 896)*, volume 896, pages 81–90, 2007.

AM Williams, PA Beeley, and NM Spyrou. Response of a lithium gadolinium borate scintillator in monoenergetic neutron fields. *Radiation Protection Dosimetry*, 110(1-4): 497–502, 2004.

Richard A Wolf. Rates of nuclear reactions in solid-like stars. *Physical Review*, 137(6B): B1634, 1965.

K Wolke, V Harms, HW Becker, JW Hammer, KL Kratz, C Rolfs, U Schröder, HP Trautvetter, M Wiescher, and A Wöhr. Helium burning of22ne. *Zeitschrift für Physik A Atomic Nuclei*, 334(4):491–510, 1989.

SE Woosley and William A Fowler. A nuclear correction factor for re/os cosmochronology. *The Astrophysical Journal*, 233:411–417, 1979.

SE Woosley and A Heger. Nucleosynthesis and remnants in massive stars of solar metallicity. *Physics Reports*, 442(1):269–283, 2007.

Kurt L Wray and Thomas J Connolly. Thermal conductivity of clear fused silica at high temperatures. *Journal of Applied Physics*, 30(11):1702–1705, 1959.

Stanley P Wyatt and Julius H Cahn. Kinematics and ages of mira variables in the greater solar neighborhood. *The Astrophysical Journal*, 275:225–239, 1983.

David Yong, Frank Grundahl, David L Lambert, Poul Erik Nissen, and MD Shetrone. Mg isotopic ratios in giant stars of the globular cluster ngc 6752. *Astronomy & Astrophysics*, 402(3):985–1001, 2003a.

David Yong, David L Lambert, and Inese I Ivans. Magnesium isotopic abundance ratios in cool stars. *The Astrophysical Journal*, 599(2):1357, 2003b.

James F Ziegler and Jochen P Biersack. Srim-2008. *Stopping Power and Range of Ions in Matter*, 2008.

JF Ziegler, JP Biersack, and MD Ziegler. The stopping and range of ions in matter, srim, 2013. *Website: http://www. srim. org*, 2013.